Università degli Studi di Pavia

Dipartimento di Scienze della Terra e dell'Ambiente

SCUOLA DI ALTA FORMAZIONE DOTTORALE

MACRO-AREA SCIENZE E TECNOLOGIE

DOTTORATO DI RICERCA IN SCIENZE DELLA TERRA E DELL'AMBIENTE

Emanuele Bonanno

Fault-propagation fold kinematics in mechanically anisotropic rocks: controlling factors.

Anno Accademico 2016-2017
Ciclo XXX

Coordinatore
Prof. Roberto Sacchi

Tutor
Prof. Silvio Seno

Co-tutor
Dott. Lorenzo Bonini

INDEX

Abstract

This study aims to define the impact of the mechanical stratigraphy, such us thin, mechanical discontinuities, on the evolution of reverse faults and their related folds. Among different mechanical discontinuities that exist in nature, my goal is to analyze the role of thin, frictional discontinuities, by means of two methodologies, i.e. analogue and numerical modeling.

Analogue models use wet clay as analogue material, and they have been designed to simulate the growth of two master faults dipping at 30° in one case and 45° in another, that are the two most common dips for reverse fault in nature. For each fault dip, one or two thin discontinuities have been inserted in the clay pack. Their results are then compared with the results obtained from fully isotropic models. The results of this first study show that reactivated discontinuities affect both the development and the propagation of new faults and the shape of the associated folds.

Experimental constrains of analogue models inhibit testing different frictional properties of the discontinuities, thus inhibit simulating the variety of mechanical discontinuities that exist in nature. To overcome this limitation, in a second study, I employ boundary element method (BEM) numerical models to investigate the effect of different frictional properties of the discontinuities on the reverse faults evolution.

BEM models numerically reproduce the fault configurations and sequence of faulting revealed by clay analogue models, and test different coefficient of friction along a layer-parallel interface in sequential stages of deformation. The results of this second study show that different frictional properties of the discontinuities induce variation in the distribution of the slip budget along the faults and discontinuities, affecting the time span of their interaction and modifying the propagation rate of the master fault.

This study thus provides new insights for an improved understanding of fault-propagation folds mechanics in regions affected by thin discontinuities. The new findings can be used to improve the existing kinematic models of fault-related folding.

Chapter 1. Introduction

The association of faulting and folding is a common feature occurring in many geological scenarios, such as mountain chains, fold-and-thrust belts, and accretionary wedges. This association named fault-related folding includes different geometric and kinematic styles depending on the geometrical and temporal relationship of the two structural elements (i.e. fault and fold), and are: *detachment folds*, *fault-bend folds*, and *fault-propagation folds* (e.g. Jamison, 1987). Fault–propagation folds forms as a fault propagates upward through the brittle crust. The displacement along the fault surface decrease to zero at its tip causing the folding of rocks above the fault. The associated fold appears generally asymmetric, with a narrow forelimb and a wide backlimb. This structural configuration is widely described in numerous outcrops and seismic reflection profiles and it is a popular subject of interest, for instance in oil and gas industry because it represents a potential hydrocarbon trap (e.g., Mitra, 1990; Lingrey, 2000; Mitra and Mount, 1998; Yan and Liu, 2004; Hesse et al., 2010;), and/or in active tectonic studies to extract data about the geometry and the activity of potentially seismogenic faults (e.g., Shaw and Shearer,1999; Allmendinger and Shaw, 2000; Benesh et al., 2007; Maesano et al., 2015).

Different methods can be applied to study the relationship between faults and the associated folds. Such methods can be grouped in kinematic (e.g., Suppe, 1983; Epard and Groshong, 1995; Mitra, 1990; Suppe and Medwedeff, 1990; Erslev, 1991; Mitra and Mount, 1998) and mechanical models (e.g., Erickson and Jamison, 1995; Roering et al., 1997; Finch et al., 2003; Finch et al., 2004; Hardy and Finch, 2007; Albertz and Lingrey, 2012; Hughes and Shaw, 2015). Kinematic models are purely based on geometrical rules that allow to retrace the paths of the material involved in deformation, thus they allow to examine the evolution of faults and folds (e.g. Suppe, 1983; Suppe and Medwedeff, 1990, Erslev, 1991). Specifically, they aim to relate the observable deformation (i.e., folds or uplifted features) to fault geometry and slip at depth. Mechanical models integrate the geometrical and kinematic models considering the forces and stresses required to produce the structures. They require rheological information as input, such as density, Young's modulus and Poisson's ratio of the rocks involved, as well as the boundary conditions to determine the distribution of the stress and strain within the deforming area.

Kinematic models has been developed and widely used to explain the evolution of the fault-propagation folds from a geometrical point of view; such as the kink-fold model developed by Suppe and Medewedeff (1990), and the trishear model developed by Erslev (1991), both successively implemented by many other studies. These kinematic models use

the geometry of the folds to determine the dip of and the displacement along the fault. The kinematic approach, however, include simplifications, for instance, it does not account mechanical stratigraphy, and it assume a constant growth rate of faults. The growth rate sometimes is not constant in isotropic materials, and even more variable if one considers naturally anisotropic geological systems. Mechanical heterogeneities such us interlayer surfaces, weak layers, or pre-existing faults placed ahead of a propagating fault tip may influence the fault propagation rate itself and the associated fold shape. This means that the assumptions of kinematic models may result, in some cases, too simplifying and could lead to incorrect interpretations of the kinematic evolution of the system.

The aim of the thesis is to analyze the effect of thin, mechanical discontinuities on the propagation of reverse faults and related folds. To this end, the research investigate this aspect employing two methodologies, i.e. analogue and numerical modeling.

Scaled analogue/physical models have been used for over a century to understand the dynamics and kinematics of rock deformation at different scales (Corti et al., 2003; Graveleau et al., 2012). This technique is based on the principle of scalability, in which geometric, kinematic and dynamic similarity between the natural prototype and the model are achieved by using different analogue materials or techniques (Hubbert, 1937).

Chapter 2 deals with the clay analogue models performed to study the effect of thin, mechanical discontinuities on the development of reverse faults and of the associated folds. One or two initially horizontal, thin discontinuities are implemented in a clay pack above an initially blind fault dipping at 30° in one case, and 45° in another. Their results are then compared with the results obtained from fully isotropic models (i.e. without thin discontinuities). The experimental results show that the occurrence of thin discontinuities affects both the development and the propagation of new faults and the shape of the associated folds, and that this is due to the localized shear strain (slip) accommodated along the discontinuities.

Although these findings improve the understanding of the evolution of faults and fault-related folds in anisotropic cases, intrinsic limitations of analogue models pave the way for further insights. For example, experimental constrains inhibit testing different frictional properties of the discontinuities, thus, inhibit simulating the variety of mechanical discontinuities encountered in nature, which differ in their ability to accommodate localized deformation. To investigate this aspect, this study used numerical modeling based on the Boundary Element Method (BEM). BEM is particularly suitable for modeling multiple faults

because it requires less effort for discretization and errors due to discretization result only along fault surface (Crouch and Starfield, 1990).

Chapter 3 deals with the BEM numerical models performed to analyze the effect of different frictional properties of the discontinuities on the propagation and evolution of thrust faults. BEM models numerically reproduce the fault configurations and sequence of faulting revealed by clay analogue models, and test different coefficient of friction along a layer-parallel interface in three successive stages of deformation. The distribution of the slip budget and the analysis of the external work reveals the stages in which the fault interacts with the discontinuity, and the stages in which the fault is expected to crosses the discontinuity. In terms of kinematic evolution, BEM models suggest that the propagation rate of a reverse fault will be affected by an overlying discontinuity as long as the discontinuity is able to accommodate localized deformation (slip).

The second and third Chapter represent the main body of the thesis and are structured in the form of articles. The second Chapter is a published work (Bonanno et al., 2017), the third Chapter is a paper in preparation.

The results coming from the two correlated studies provide new clues and new constraints for an improved understanding of the evolution of faults and fault-related folds in regions affected by different types of thin, mechanical discontinuities.

Chapter 2. The effect of thin, mechanical discontinuities on fault-propagation fold kinematics: an analogue modeling perspective

This chapter wholly reports the paper *"How do horizontal, frictional discontinuities affect reverse fault-propagation folding?"* published by Bonanno E., Bonini L., Basili R., Toscani G., and Seno S., (2017) on the *Journal of Structural Geology*, vol. 102, pp.147-167.

ABSTRACT

The development of new reverse faults and related folds is strongly controlled by the mechanical characteristics of the host rocks. In this study we analyze the impact of a specific kind of anisotropy, i.e. thin mechanical and frictional discontinuities, in affecting the development of reverse faults and of the associated folds using physical scaled models. We perform analogue modeling introducing one or two initially horizontal, thin discontinuities above an initially blind fault dipping at 30° in one case, and 45° in another, and then compare the results with those obtained from a fully isotropic model. The experimental results show that the occurrence of thin discontinuities affects both the development and the propagation of new faults and the shape of the associated folds. New faults 1) accelerate or decelerate their propagation depending on the location of the tips with respect to the discontinuities, 2) cross the discontinuities at a characteristic angle (~90°), and 3) produce folds with different shapes, resulting not only from the dip of the new faults but also from their non-linear propagation history. Our results may have direct impact on future kinematic models, especially those aimed to reconstruct the tectonic history of faults that developed in layered rocks or in regions affected by pre-existing faults.

2.1. Introduction

Shortening in the brittle crust is mostly accommodated by folding, fracturing, and faulting. These processes are intimately associated with one another and understanding their evolution through time is of paramount importance. Several kinematic models have been proposed to explain the relationships between faulting and folding (for a recent summary see McClay, 2011; and Brandes and Tanner, 2014). It is generally accepted that fault-related folding can be described by three end-member geometries: detachment folds, fault-bend folds, and fault-propagation folds (e.g. De Sitter, 1956; Dahlstrom, 1969; Suppe, 1983; Suppe and Medwedeff, 1984, 1990; Jamison, 1987; Chester and Chester, 1990; Mitra, 1990, 1992, 2003; Erslev, 1991; Fisher et al., 1992, Epard and Groshong, 1995; Poblet and McClay, 1996; Storti and Salvini, 1996; Hardy and Ford, 1997; Allmendinger, 1998; Suppe et al., 2004; Tavani et al., 2006; Hardy and Finch, 2007; Albertz and Lingrey, 2012;). Such three end-members, however, often represent different stages in the evolution of the same structure (e.g., Tavani and Storti, 2006; Storti et al., 1997). For instance, a contractional structure may form as a detachment fold, then propagate upward forming a ramp as a fault-propagation fold, and finally be deflected along a weak layer to operate as a fault-bend fold.

Although the evolution of detachment folds and fault-bend folds is mainly related to the friction of the surface where they propagate and to the intrinsic mechanical properties of the rocks involved, the propagation of a ramping fault is a more complex mechanism, mainly because a new slipping surface must be created. The development of new faults in an isotropic medium occurs through three successive phases (e.g., Anderson, 1942; Brace et al., 1966; Segall and Pollard, 1983; Cartwright et al., 1995; Mansfield and Cartwright, 2001; Scholz, 2002; Faulkner et al., 2006; Bonini et al., 2015): 1) a “nucleation” phase, during which small cracks form as a consequence of the applied stress, usually with an en echelon arrangement; 2) a “creation” phase, when new fault planes form through the coalescence of previously formed cracks; and 3) a “propagation” phase, when a single fault grows through the connection of small cracks located at its outer tips. Note that during the propagation phase, both nucleation and creation phases continue to occur at fault tips, and that the general evolution of a fault is seldom a linear process. In an ideal isotropic case, however, the linear propagation of a new fault is often an accepted assumption. Different factors may affect this linearity in nature, including the different strength of the rocks involved in the faulting process, the non-uniformity of the stress field, the presence of fluids, the occurrence of background inherited fractures - which may not be homogeneously distributed in the faulted

sequence - and pressure and/or heat flow variations. As a result, any deviation from the linearity of fault propagation impacts also on the associated folding.

Understanding the deviations from linearity in the propagation of a ramping fault is fundamental in many applications which use the activity (slip) of the fault as a basic parameter. In regions of active tectonics or in the external portion of orogenic belts, reverse faults or thrust-fault ramps are often blind or buried below piles of sediments, thus preventing any direct observation of the faults. Several kinematic models have been developed to relate the observations of deformation features (e.g. folded horizons, secondary brittle structures, uplifted and warped terraces, growth strata) to their causative fault and to investigate the evolution of the whole system through time (e.g., Suppe, 1983, Suppe and Medwedeff, 1990; Erslev, 1991; Epard and Groshong, 1995; Homza and Wallace, 1995; Hardy and Ford, 1997; Allmendinger, 1998; Mitra, 2002b, 2003; Allmendinger et al., 2004; Suppe et al., 2004; Vannoli et al., 2004; Jin and Groshong, 2006; Tavani et al., 2006; Storti and Salvini, 1996; Cardozo and Aanonsen, 2009; Cardozo et al., 2011; Maesano et al., 2013; Grothe et al., 2014; Maesano et al., 2015; Bergen et al., 2017). Other studies used different approaches based on mechanical modeling, such as boundary element methods (BEM; e.g. Roering et al., 1997), finite element methods (FEM; e.g. Albertz and Lingrey, 2012), and discrete element methods (DEM; Hughes and Shaw, 2015).

Most studies agree that one of the main elements controlling the evolution of a ramping fault is the mechanical stratigraphy. Deviations from a linear evolution are commonly observed in layered rocks that are often characterized by alternating weak and strong layers. However, such behavior can be also associated with other mechanical heterogeneities. For example, interlayer surfaces or pre-existing fault planes located along the propagating fault trajectories represent mechanical discontinuities within the hosting rocks. How do these thin, frictional, mechanical discontinuities impact on the propagation of a ramping fault? To answer this question we analyze a set of analog models. Our goal is to highlight how initially horizontal thin, mechanical discontinuities deviate a propagating fault from its linear development. We study how such discontinuities affect the evolution of fault-propagation folds, first by reproducing the development of initially blind, reverse faults dipping at different angles. We then introduce one or two horizontal discontinuities above the fault initial tip to quantitatively analyze their role in affecting the development of the whole structure. Finally, we use our results to discuss the potential impact of our findings in the investigation of natural cases.

2.2. Method

Among the various fault dips that can be adopted for a preliminary experimental analysis we chose to reproduce the dips that are most commonly observed in areas of active reverse faulting. A global compilation of active reverse faults (Sibson and Xie, 1998) indicates two prominent peaks in the 25°-35° and 45°-55° intervals. Accordingly, we designed two experimental boxes with the master fault, i.e. the inclined surface along which the two rigid blocks slip with reverse kinematics, dipping at 30° and 45° (Fig. 2.1): the corresponding sets of experiments are named DIP30 and DIP45, respectively (Table 2.1). The two boxes are composed by two rigid blocks: one is fixed and represents the footwall, the other is mobile and represents the hanging wall (Fig. 2.1). The analog material overlies these blocks and simulates the rock volume where the reverse fault is expected to propagate. In this setup the master fault is initially planar and blind.

As analogue material we used wet kaolin (#CC31 China Clay), which is widely used to analyze faulting and folding processes in scaled experiments (e.g. Withjack et al., 1990; Miller and Mitra, 2011; Mitra and Miller, 2013; Cooke et al., 2013; Bonini et al., 2014a; Bonini et al., 2016a). Several peculiarities make the kaolin especially suitable for our purpose: 1) its mechanical properties can be easily assessed by measuring the water content of the mixture and by imposing a specific strain rate; 2) thin mechanical discontinuities can be easily introduced by cutting the clay pack; 3) the small size of clay particles allows for a very high resolution of strain observations, especially those related with faulting and fracturing. The analogue material is not laterally confined along the side in which we performed observations and analysis.

Table 2.1. Summary of the analog experiments presented in this study.

Mater fault dip	Number of precuts	Number of models	Initials	Clay thickness (mm)	Precut position (distance from the base of the model; mm)
30°	0	3	DIP30_ISO	50	-
	1	3	DIP30_1PC	50	25
	2	3	DIP30_2PC	50	17 (lower) - 34 (upper)
45°	0	3	DIP45_ISO	50	-
	1	3	DIP45_1PC	50	25
	2	3	DIP45_2PC	50	17 (lower) - 34 (upper)

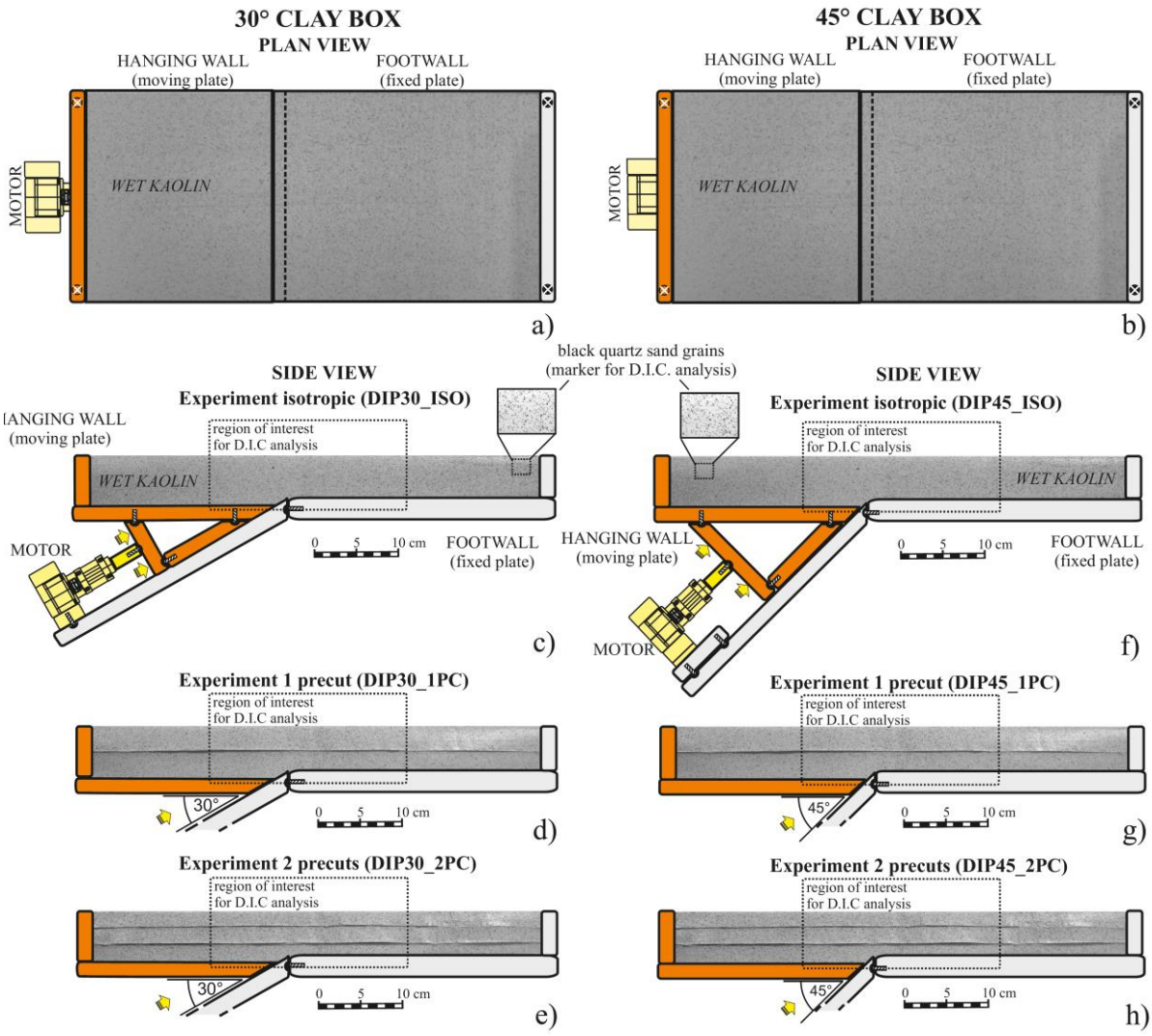

Figure 2.1. Schematic representation of the experimental apparatus with two different setups: 30° clay box (left column), and 45°clay box (right column). a) and b) are the plan view of both boxes. c), d), e) f), g), h) show the side view for all the configurations, both isotropic and with precuts. Orange colour marks the mobile parts.

2.2.1. Scaling

A proper analog experiment is subject to specific scaling rules that must be representative of a natural setting (Hubbert, 1937; Hubbert, 1951; Ramberg, 1981). As recalled earlier, the mechanical behavior of wet kaolin depends mainly on its water content and strain rate (e.g., Eisenstadt and Sims, 2005; Cooke and van der Elst, 2012). In this study we used a mixture of clay with a 60% water content by mass, resulting in a density of 1.65 g/cm^3. It follows that we may assume a cohesion in the range 50 to 120 Pa (Eisenstadt and Sims, 2005) and a friction coefficient of 0.6 (Henza et al., 2010). To ensure a proper rheological behavior during the experiments we adopted a 0.02 mm/s hanging wall speed

(Cooke and van der Elst, 2012). As a natural target we assumed a rock with a density of 2.5 g/cm^3 and a cohesion in the range 10-20 MPa. Hence, the scaling relationship can be calculated as:

$$\frac{c_m}{c_n} = \frac{\rho_m}{\rho_n}\frac{l_m}{l_n} \quad (1)$$

where c is the cohesion, ρ is the density and l is the length. The subscripts m and n denote the analogue model and the natural target, respectively. Solving Eq. 1 for the length of the models gives

$$l_m = l_n \frac{\rho_n}{\rho_m}\frac{c_m}{c_n} \quad (2)$$

and using the maximum and minimum values of the kaolin cohesion we obtain that 10 mm in our model correspond to about 0.1-1.0 km in nature. Hence, the clay cake placed above the two rigid blocks was made 50 mm-thick, representing 0.5-5.0 km in nature.

2.2.2. Modeling strategy

To analyze the impact of the presence of thin, horizontal, mechanical discontinuities onto the development of reverse faults and related folds we introduced such discontinuities in our models by cutting the clay cake with an electrified probe before moving the hanging wall block. This technique allows us to precut the wet clay pack without modifying its mechanical properties (Cooke et al., 2013; Bonini et al., 2014a; Bonini et al., 2015; Bonini et al., 2016a). We thus assume that friction along the precut is the same as that of natural faults forming in the wet kaolin.

For both experimental setups (DIP30 and DIP45) we tested three different configurations (Fig. 2.1; Table 2.1): 1) an isotropic case (_ISO), i.e. a single clay layer without any precut; 2) a case where there is only one precut in the middle of the clay pack (_1PC), thereby forming two clay layers; 3) a case where two evenly spaced precuts have been introduced (_2PC), thereby forming a three-layer clay pack. To test the repeatability of the processes and to handle the data statistically we replicated each configuration three times. The isotropic experiments serve as reference for all the others. Models with one precut provide information on how new faults interact with a horizontal discontinuity and how this interaction impacts on the folding process. Models with two precuts allow us to observe what happens when the discontinuity is closer to the initial tip of the master fault (the lower

precut), and how the increased number of discontinuities compares with the outcomes from the isotropic and single-precut models.

2.2.3. Data analysis

We collect data from our models by taking high-resolution photographs (at 18 megapixel resolution) of the lateral side of the experimental box at every 1 mm of displacement along the master fault plane. These images are analyzed every 5 mm in two main ways: 1) using the Move software (Midland Valley Exploration Ltd) to digitize faults, fractures, and folds; and 2) using the PIVlab software (Thielicke, 2014; Thielicke and Stamhuis, 2014), which adopts an optical technique in visible light (Digital Image Correlation method, D.I.C.) to aid the detection of particles movements and thus quantify the amount of deformation. All images are referenced to a fixed coordinate system so that structures from different models and at different shortening be compared objectively. Black quartz sand grains are placed on the side of the clay cake before starting the experiments to act as markers for the identification of displacement without modifying the mechanical properties of the clay mixture. The D.I.C in particular allows us to calculate the displacement field and the shear strain rate distribution.

One of the key elements to understand fault kinematics is the analysis of fault displacement, allowing a detailed reconstruction of fault evolution and the discrimination of the fault-related folding style (e.g., Williams and Chapman, 1983; Hedlund, 1997; Tavani et al., 2006; Hughes and Shaw, 2014). The ratio between propagation and slip (P/S) of a fault is another widely used parameter that allows the fault-related folding evolution to be analyzed in detail, in particular using methods based on the trishear theory (e.g., Erslev, 1991; Hardy and Ford, 1997; Allmendinger, 1998). By varying the P/S ratio we can restore different fold shapes associated with propagating faults, leaving all other parameters such as the fault dip or the fault tip position unchanged, (e.g., Allmendinger and Shaw, 2000). Our experimental approach provides data about the displacement distribution along the fault and about the propagation of the fault through time. The latter is particularly important because the propagation rate of a fault can hardly be observed in nature, and also because fault propagation models are mainly based on the analysis of the displacement distribution along the fault from markers in the hanging wall and footwall. To extract data such as fault length and P/S ratio while the fault grows during the experiments we measure the coordinates of the upper tip point of the main new faults every 5 mm of total displacement imposed on the master fault. The retained fault upper tip position is the average of the three realizations of

each experimental configuration. Many new faults form during the experiments, but we collect these data only about the main faults, i.e. those showing a significant change of the velocity field and along which the shear strain rate is larger (Fig. 2.2a), excluding secondary faults and fractures. When multiple faults show significant activity we assume the most developed one, i.e. the longest one, as the main fault.

Another interesting piece of information is the angle formed between the direction of the propagating faults and the slope of the discontinuity at its inflection point (Fig. 2.2b), which we refer to as Angle Of Incidence (AOI). The direction of new faults is measured as the up-dip projection of the line connecting the tip of the master fault and the tip of the main new propagating faults. The slope of the inflection point is obtained first by fitting the line drawing of precuts (sampled at regular intervals of 10 mm) with a spline function, then by calculating the first derivative of these curves. The average of the angle of incidence measured from the three experiments for each configuration is retained for further analyses.

Finally, to investigate the evolution of folds associated with fault propagation we inspect the topographic surface of the experiments during deformation every 5 mm of displacement on the master fault. Similarly to the other observations described above, we use data from three experiments for each configuration and retain the average. To this end we sample the height of each model surface at a regular spacing of 10 mm, then fit these data with a spline function to obtain a synthetic curve representing the fold shape at each deformation step (Fig. 2.2c).

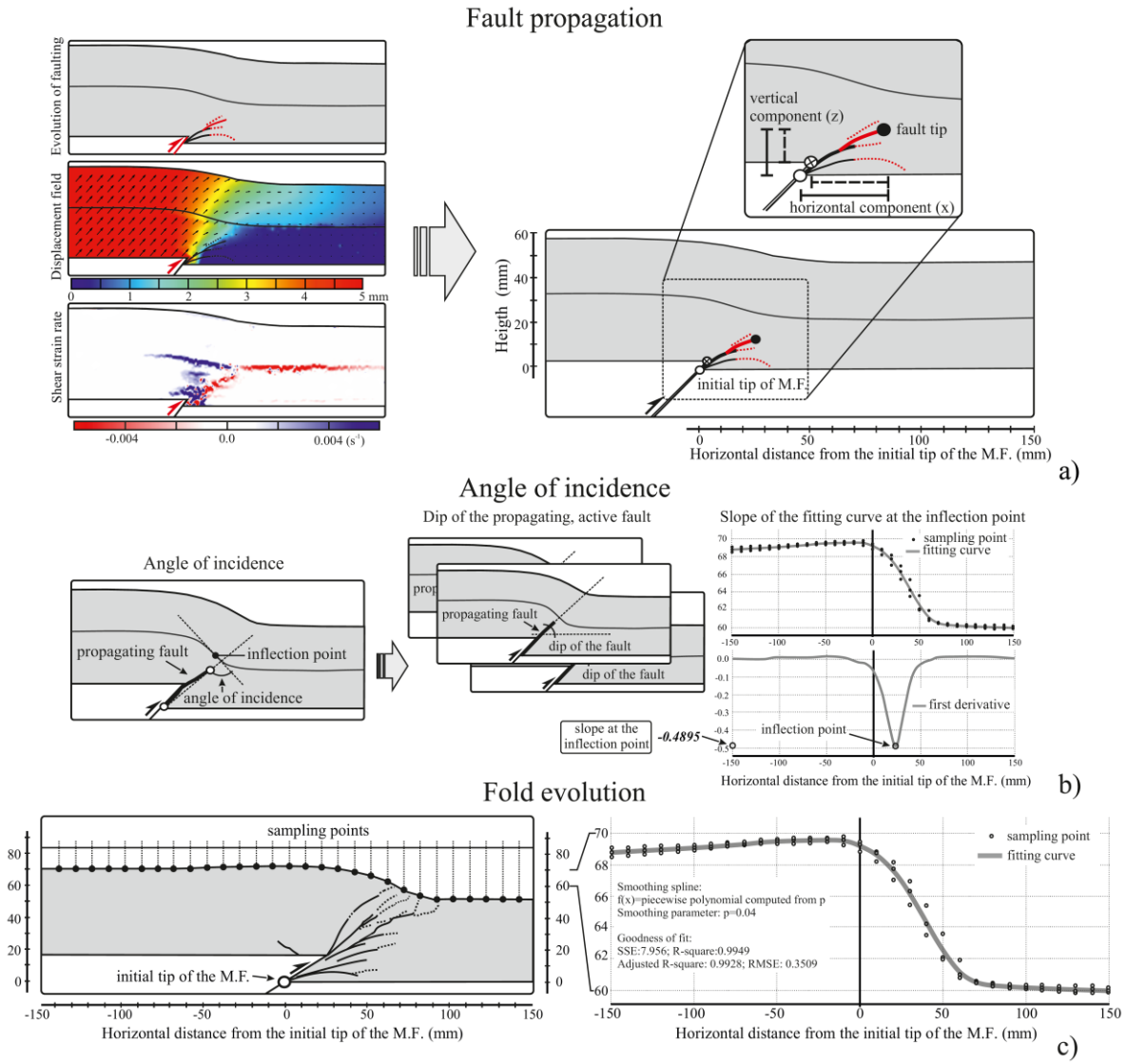

Figure 2.2. Data acquisition procedure: a) Fault propagation: combining velocity field, shear strain rate and faults and fractures analyses to obtain the tip coordinates of the most active main fault. We consider the total length of the new faults (denoted by solid lines) as the distance between the initial tip point of the master fault and the upper tip of the new faults. The net length of the new faults (denoted by dashed lines) is the distance between the hanging wall cut-off of the rigid block and the upper tip of the new faults. b) Procedure to establish the angle of incidence (see section 2.2.3 for explanation). c) Fold evolution: sampling of the free upper surface of the model at regular intervals (every 1 cm) for three experiments with the same configuration, and application of the smoothing spline function to the three curves to get the best fit (see section 2.2.3 for explanation).

2.3. Experimental results

We present here the main features observed in all the experiments. Specifically, we describe the geometry and development of faults and tensile fractures, the displacement field, and the shear strain rate distribution for all model configurations. For the sake of simplicity, in sections 2.3.1 and 2.3.2 we limit the description to one of the three series of experiments. The new faults formed in the isotropic experiments, in both the DIP30 and DIP45 configurations, reach the surface after about 40 mm of total displacement on the master fault. Considering that the specific goal here is to compare experiments with and without precuts, we describe the experiments with precuts only until we accumulate 40 mm of total slip even if no new faults have reached the surface at this displacement level. We subdivide the model evolution into two stages based on the amount of displacement imposed on the master fault: an Early Stage from 0 to 20 mm, and a Late Stage from 20 to 40 mm. The results in terms of fault propagation, angle of incidence (AOI) and fold evolution are obtained considering the three series of experiments for each configuration (see section 2.2.3 for explanations).

2.3.1. DIP30 Experiments (ISO, 1PC, 2PC)

This section describes the results of experiments performed with a 30°-dipping master fault (DIP30_ISO, DIP30_1PC, and DIP30_2PC; Table 2.1), illustrating faults and fractures that are visually detected on the long side of the models (Fig. 2.3), the displacement field (Fig. 2.4), and the shear strain rate (Fig. 2.5) derived from D.I.C. analysis.

During the Early Stage, in DIP30_ISO the new faults nucleate at the tip of the master faults and develop with a shallow dip as they propagate forward until they become horizontal or even curve downward into the footwall (Fig. 2.3). At the end of the Early Stage, more new faults are formed in the hanging wall of the previous ones with progressively steeper dip (Fig. 2.3). In DIP30_1PC, during the Early Stage the new faults exhibit the same pattern as those seen in the isotropic case. In DIP30_2PC, the new faults are fewer and reach the lower precut at the end of the Early Stage (Fig. 2.3). In DIP30_ISO the displacement field highlights a trishear zone, with the apex located at the upper tip of the steeper fault (Fig. 2.4). The low-angle faults and fractures located in the footwall border the lower edge of the trishear zone. This zone is preserved during the entire DIP30_ISO, whereas in DIP30_1PC and DIP30_2PC it appears segmented since the beginning of the Early Stage due to partial reactivation of the precuts, as pointed out by shear strain rate analysis (Fig. 2.5). In DIP30_2PC the new faults

are deflected, and when they link with the lower precut the extent of slip along them increases (Fig. 2.4 and 2.5). Conversely, during the Early Stage of experiment DIP30_1PC the faults remain below the precut, so that the precut is not fully activated.

During the Late Stage, in DIP30_ISO the new faults continue to grow (Fig. 2.3). The activity of the faults having a dip similar to that of the master fault is prominent with respect to other faults, as testified by both the velocity field (Fig. 2.4) and the shear strain rate (Fig. 2.5) analyses. In DIP30_1PC and DIP30_2PC the upward propagation of faults and fractures stops against precuts, though in DIP30_2PC some fractures cross the lower precut at the end of the stage. Also in DIP30_1PC and DIP30_2PC the activity of faults showing the same dip as that of the master fault is predominant, while the activity on the low-angle faults gradually decreases (Fig. 2.5). In DIP30_1PC and DIP30_2PC layer-parallel faults nucleate in front of the upward-propagating faults and within the layers, along the neutral surface of the blocks bordered by precuts and the free surface. In DIP30_1PC the layer-parallel faults form close to the neutral surface of the upper layer, i.e. the layer between the free surface and the precut. In DIP30_2PC, several layer-parallel faults form; first in the middle layer, i.e. the layer located between the two precuts, and then in the uppermost layer. Conversely, layer-parallel faults never appear in the isotropic experiment. The displacement field (Fig. 2.4) shows that the trishear zone progressively narrows as deformation increases in all three cases. Finally, the activity of precuts and layer-parallel faults produces a decoupling between the different layers. Notice that in DIP30_2PC an upward-propagating fault overtakes the lower precut and promotes the transition of slip from the lower to the higher precut at the end of the Late Stage (Figs. 2.4 and 2.5). In DIP30_1PC, small, reverse faults propagate downward from the free surface just along the hinge of the footwall syncline (Fig. 2.3).

2.3.2. DIP45 Experiments (ISO, 1PC, 2PC)

This section present the results of experiments performed with a 45°-dipping master fault (DIP45_ISO, DIP45_1PC, and DIP45_2PC; Table 2.1; Figs. 2.6, 2.7 and 2.8).

During the Early Stage of all DIP45 experiments new faults form at the tip of the master faults (Fig. 2.6) with shallower dip as they grow in a way similar to that observed in DIP30 experiments. In DIP45_ISO, a series of convex-up splays form with progressively steeper angle up to the dip of the master fault. Toward the end of the Early Stage a new fault having the same dip as that of the master fault nucleates at the neutral surface of the associated fold and propagates both downward and upward; small antithetic shear faults also form in its

hanging wall. In DIP45_1PC and DIP45_2PC new faults reach roughly the same height within the clay body, though in DIP45_2PC when these new faults reach the lower precut some layer-parallel faults form in the middle layer (Fig. 2.6). The displacement field of all DIP45 experiments (Fig. 2.7) shows a trishear zone that is narrower than that seen in the corresponding DIP30 experiments. In DIP45_1PC and DIP45_2PC the trishear zone also appears to be segmented as a consequence of the partial reactivation of precuts (Fig. 2.8). Similarly to DIP30, the early low-angle faults border the lower edge of the trishear zone in all DIP45 experiments. In DIP45_2PC, layer-parallel faults nucleate in the hinge zone of the middle layer.

During the Late Stage, in DIP45_ISO the fault that formed in the middle of the clay cake connects with an upward-growing fault stemming from the tip of the master fault. Several new layer-parallel faults form in the hanging wall of the newly-formed main fault (Fig. 2.6). In DIP45_1PC and DIP45_2PC the new faults are deflected as they approach the precut (the lower precut in DIP45_2PC). Layer-parallel faults form in the fold hinge zone within the middle/upper layer as they did in the DIP30 experiments, but they are more numerous. As suggested by the shear strain rate analyses, layer-parallel faults show the same shear strain rates as those of the segments reactivated along precuts (Fig. 2.8). Similarly to the DIP30 configurations, faults with the same dip as that of the master fault are prominent during this stage, while the activity of low-angle faults gradually decreases in all models (Fig. 2.8). In DIP45_1PC small fractures propagate downward from the free surface along the hinge of the footwall syncline. At the end of the Late Stage, in DIP45_1PC the new faults cross the precut, whereas in DIP45_2PC the new faults cross both precuts (Fig. 2.6).

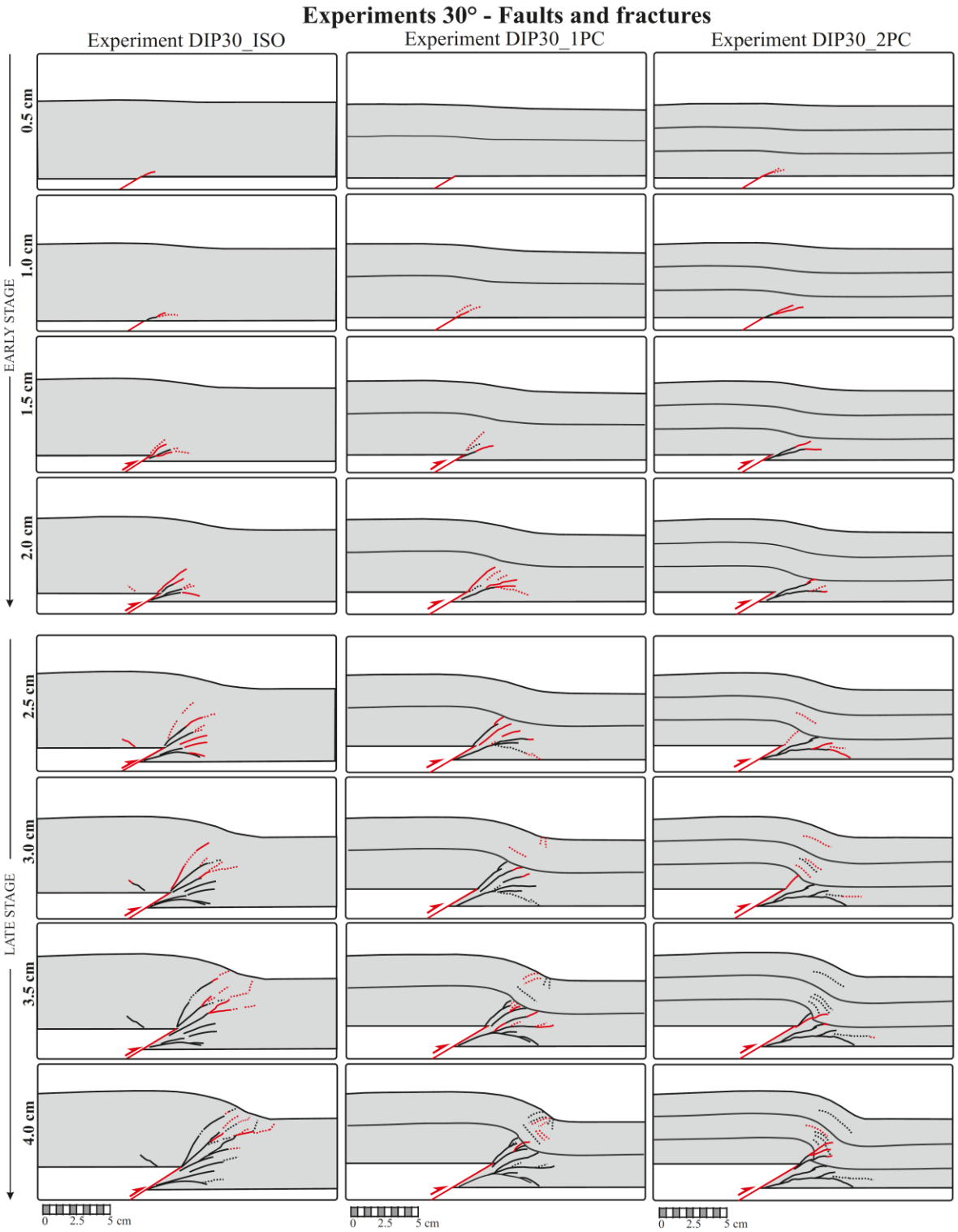

Figure 2.3. Analysis of faults and fractures in experiments with master fault dipping 30° for three different configurations: isotropic (_ISO), one precut (_1PC), and two precuts (_2PC). Each row represents the development of faults and fractures at every increment of 5 mm displacement on the master fault. Red and black lines represent the newly- and previously-formed faults, respectively, at each successive increment of displacement (5 mm). Dotted lines indicate faults or fractures where the offset determination is uncertain. Black thin lines indicates the position of precuts.

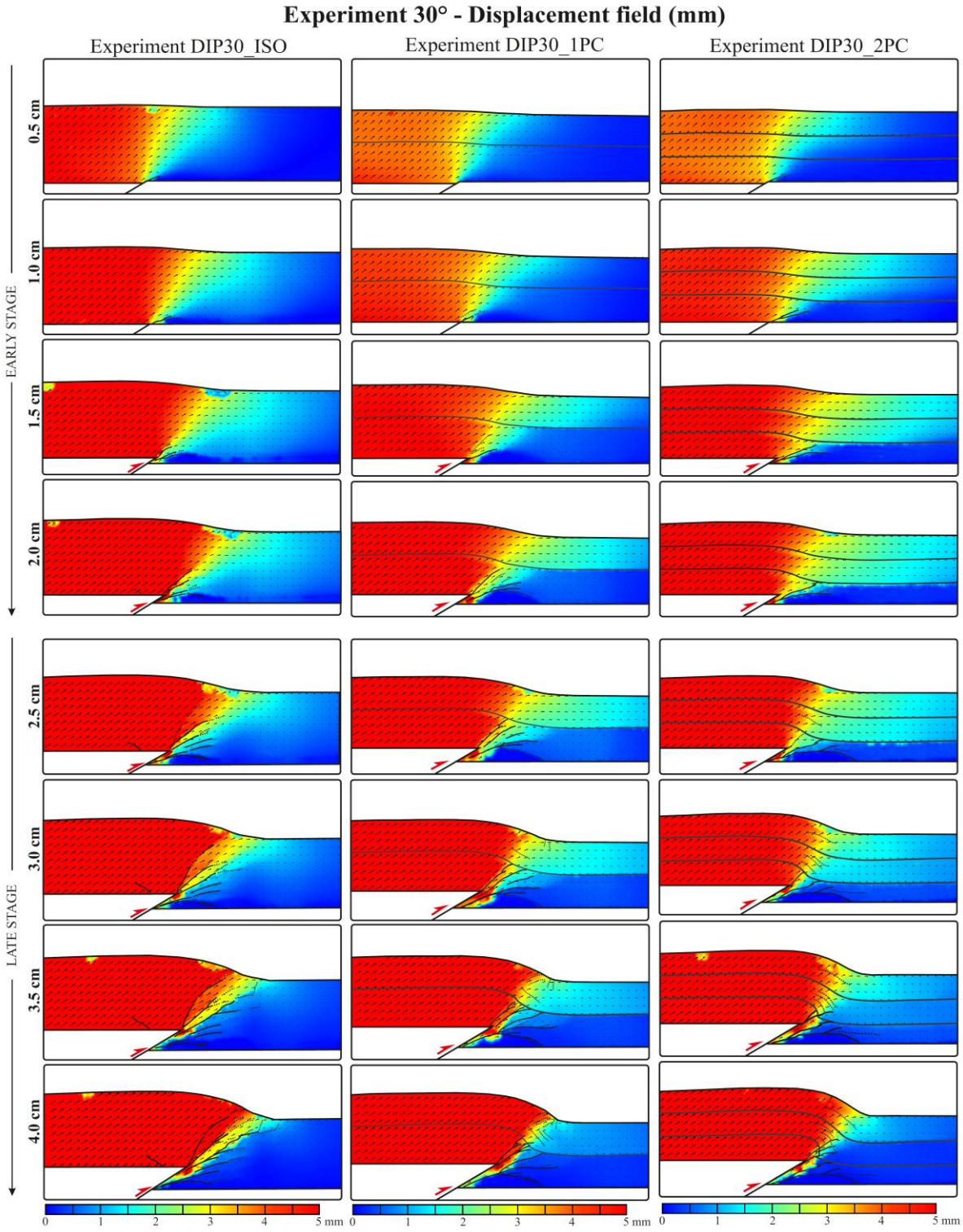

Figure 2.4. Displacement field analysis in experiments with master fault dipping 30° for three different configurations: isotropic (_ISO), one precut (_1PC), and two precuts (_2PC). Each row shows the displacement field after every 5 mm of displacement on the master fault. Black arrows represent the displacement vectors. The traces of faults, fractures, and precuts are also shown.

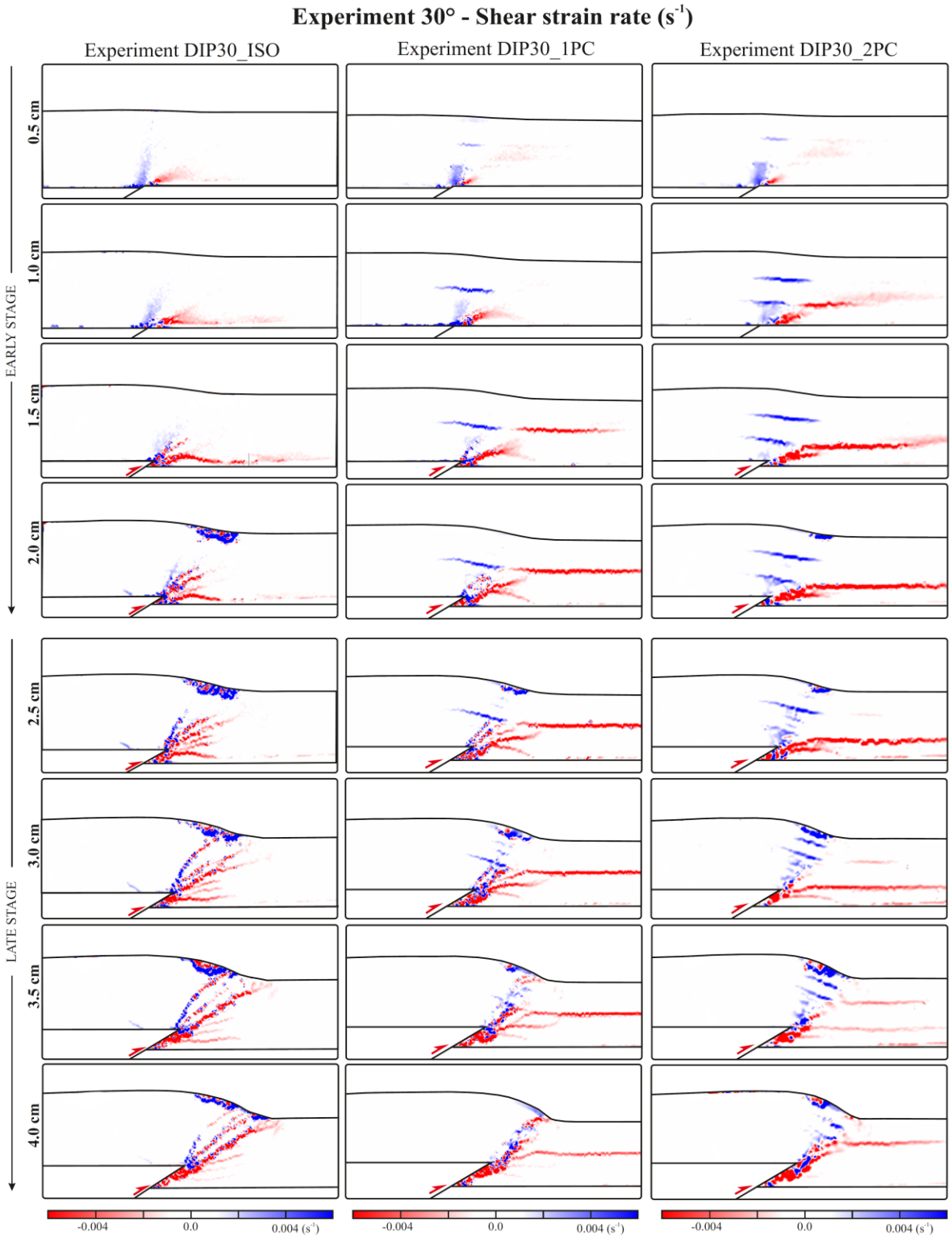

Figure 2.5. Shear strain rate analysis in experiments with master fault dipping 30° for three different configurations: isotropic (_ISO), one precut (_1PC), and two precuts (_2PC). Each row represents the shear strain rate calculated at each 5 mm of displacement on the master fault. Red and blue zones highlight dextral and sinistral sense of shear in the side view, respectively.

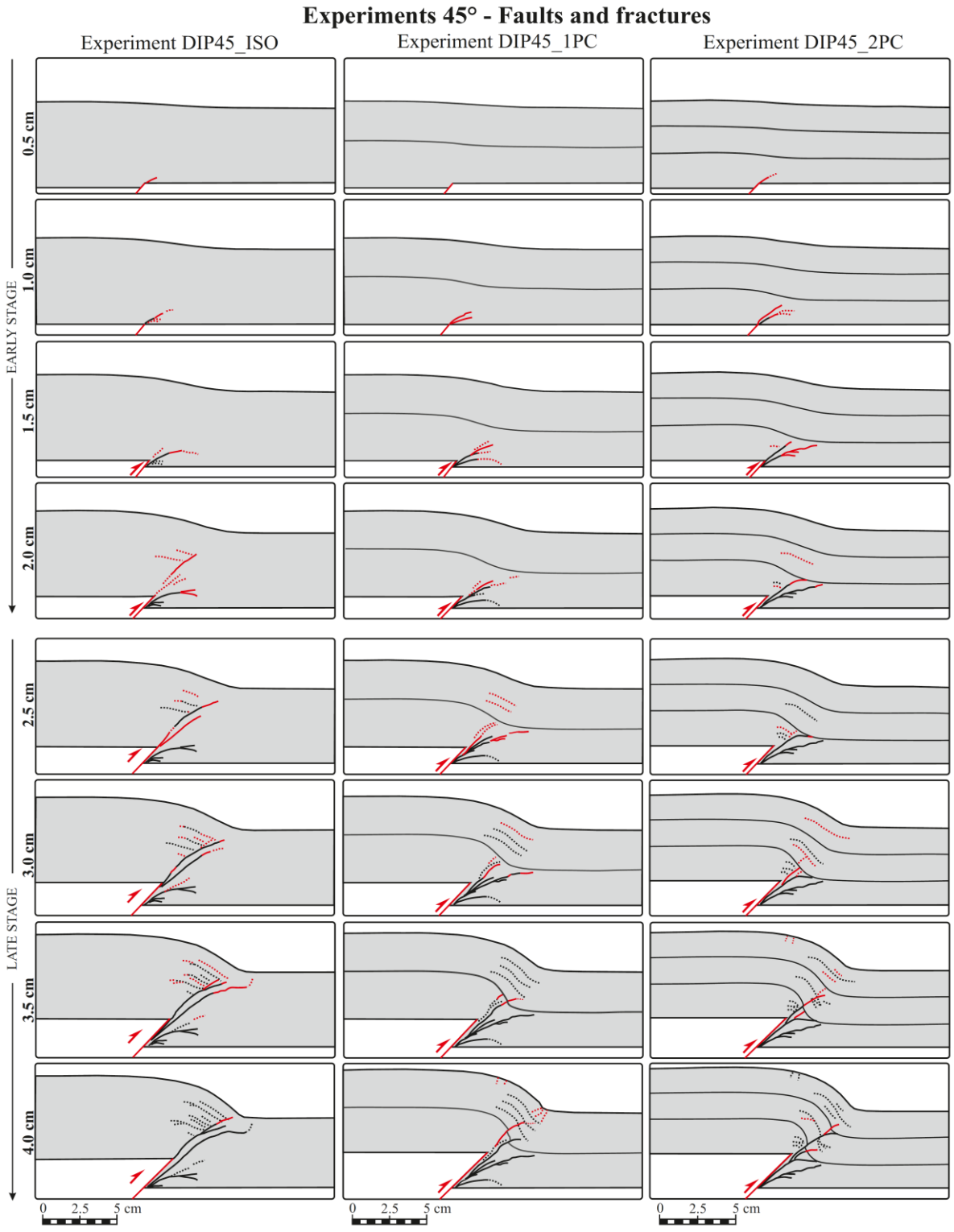

Figure 2.6. Analysis of faults and fractures in experiments with master fault dipping 45° for three different configurations: isotropic (_ISO), one precut (_1PC), and two precuts (_2PC). Each row represents an increment of 5 mm of displacement on the master fault. Red and black lines represent the newly- and previously-formed faults, respectively, at each successive increment of displacement (5 mm). Dotted lines indicate faults or fractures where the offset determination is uncertain. Black thin lines indicates the position of precuts.

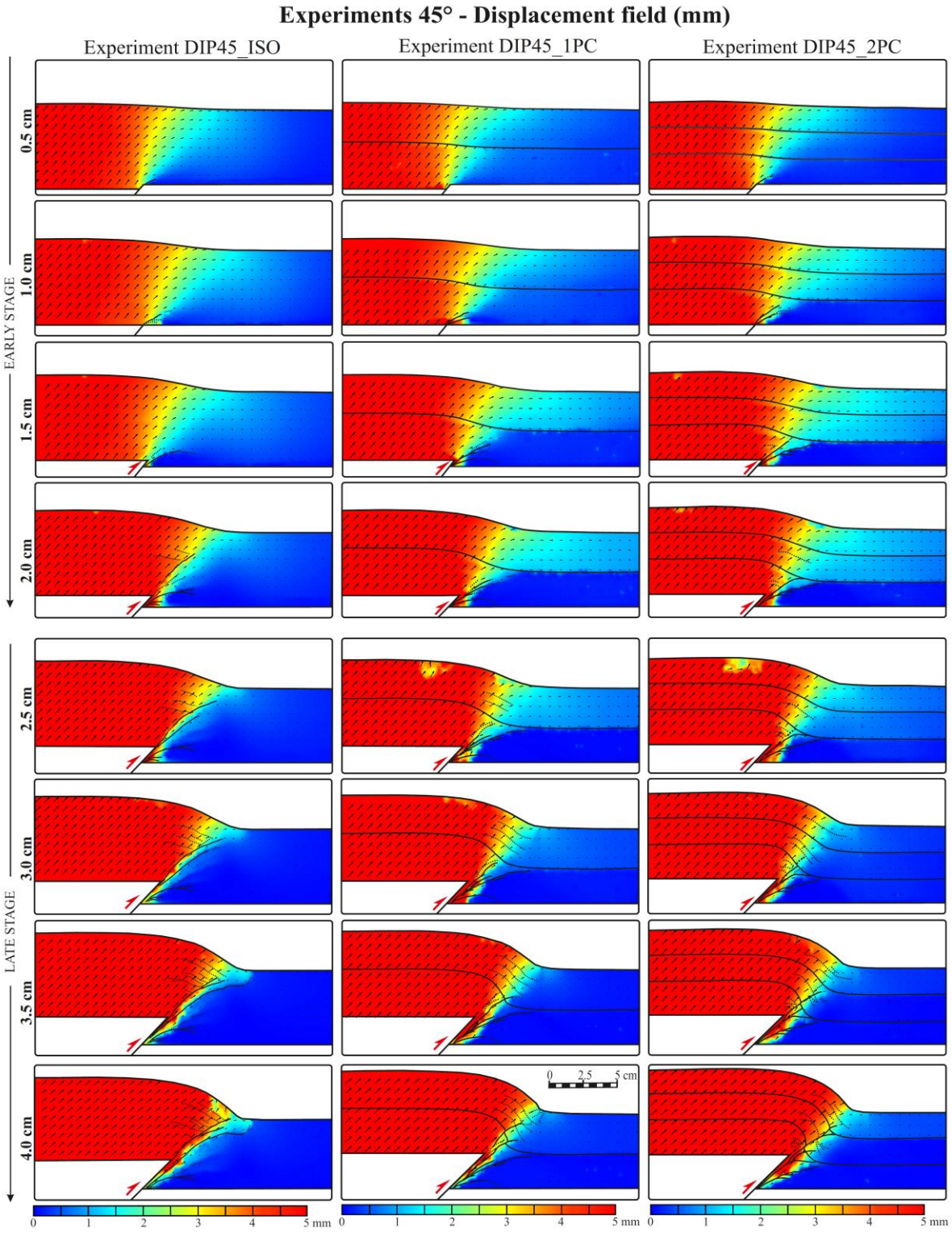

Figure 2.7. Displacement field analysis in experiments with master fault dipping 45° for three different configurations: isotropic (_ISO), one precut (_1PC), and two precuts (_2PC). Each row shows the displacement field after every 5 mm of displacement on the master fault. Black arrows represent the displacement vectors. The traces of faults, fractures, and precuts are also shown.

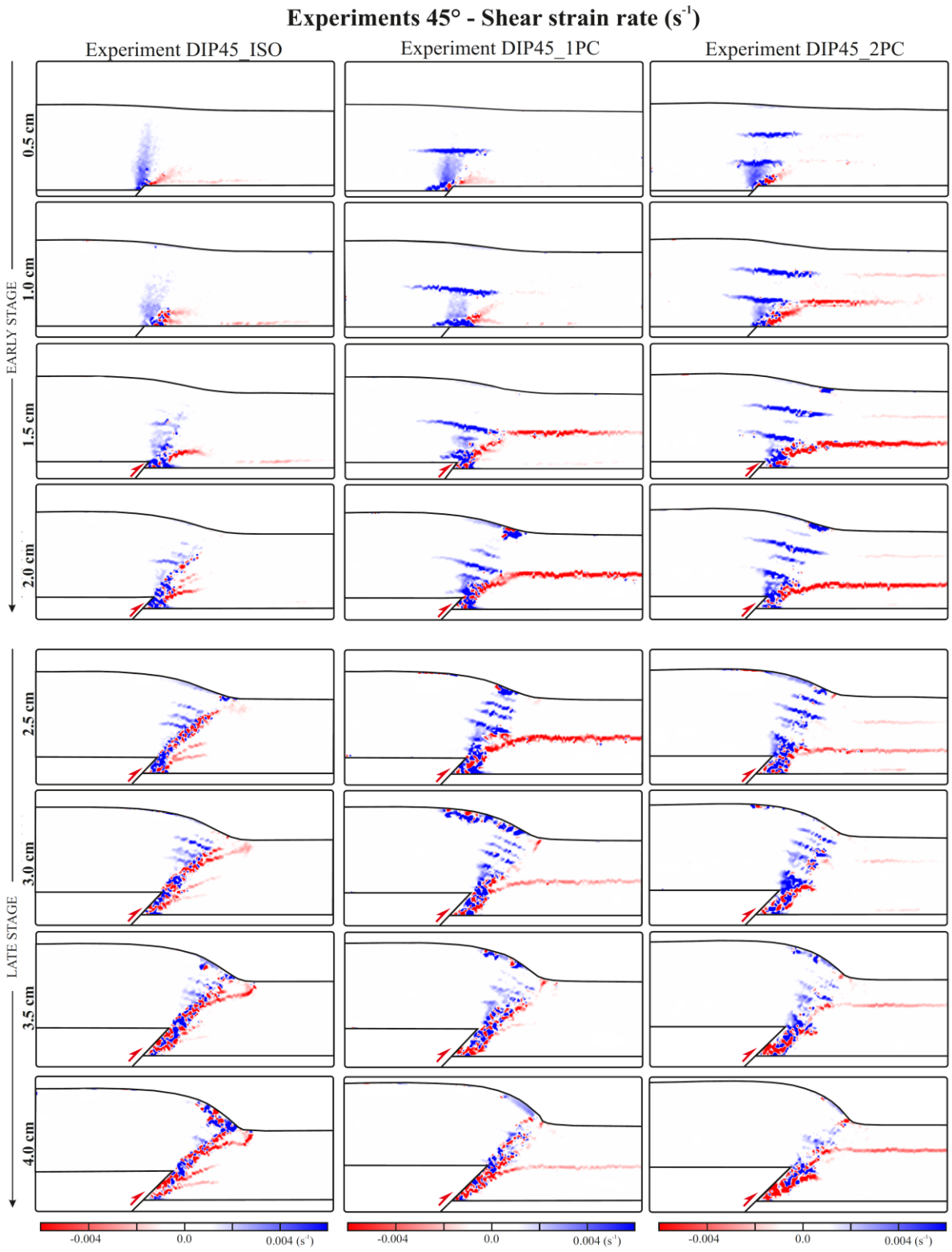

Figure 2.8. Shear strain rate analysis in experiments with master fault dipping 45° for three different configurations: isotropic (_ISO), one precut (_1PC), and two precuts (_2PC). Each row reports the shear strain rate calculated each 5 mm of displacement on the master fault. Red and blue zones highlight dextral and sinistral sense of shear in the side view, respectively.

2.3.3. Fault propagation

This section presents data of the evolution of new faults described using their length and P/S from all the experiments (see Fig. 2.9). In DIP30_ISO, the propagation of the main new faults is rather linear with a total average P/S ratio equal to 2.3. The quite regular increase and decrease of the P/S ratio is indicative of the propagation and nucleation phase of the new faults (Figs. 2.9a, and 2.9c). In DIP30_1PC, the evolution of the length of the new faults is rather regular only up to 25 mm of total displacement (Fig. 2.9c), i.e. until the new faults reach the precut: hence, the propagation of new faults rapidly decreases because the new faults are deflected along the precut (Fig. 2.9c). The total average P/S ratio (1.6) is lower than that observed in the isotropic experiment. In DIP30_2PC, the P/S ratio increases rapidly to 4.7 up to 10 mm of total displacement, then decreases to 0.8 when reaching 15 mm of total displacement, then increases again up to 1.4 at the end of the experiments (Fig. 2.9a). In summary, when the new fault is below the precut, the propagation rate is faster than that observed in the isotropic case. When the new fault reaches the precut it is deflected along it and almost stops its propagation. Once the fault crosses the precut, it tends to the same P/S ratio of the isotropic case. Notice that the non-zero P/S ratio in the experiments with one or two precuts when the new fault reaches them does not mean that the propagation of the fault has slowed down; rather it implies that the fault propagation has stopped against the precut while the system is still accumulating deformation due to increasing displacement on the master fault. In this case the change in P/S ratio means that the upper tip point of the new fault changes its position without increasing the length of the fault, and this point migration being located within the trishear zone.

The DIP45_ISO experiment shows a quite linear trend of the P/S ratio, its average being similar to that of DIP30_ISO (2.1 vs 2.3: Fig. 2.9e). Also in this case the increase and decrease of P/S ratio indicate the nucleation and propagation phases of new faults. In DIP45_1PC, the fault length is similar to that observed in the isotropic case (Figs. 2.9b and 2.9d). The _ISO and _1PC configurations evolve differently at 20 mm of displacement, when the new faults in DIP45_1PC approach the precut. At the end of DIP45_1PC, both the length of new faults and P/S ratio increase, approaching the values observed in DIP45_ISO. The difference in the average of P/S ratio in DIP45_ISO and DIP45_1PC is negligible (DIP45_ISO, P/S = 2.1; DIP45_1PC, P/S = 2.2; Fig. 2.9b). The general trend of the fault propagation is quite different if compared to the DIP30_1PC experiment (Fig. 2.9f), where the new faults remain below the precut until the end of the experiments with an almost regular trend. In the DIP45_2PC experiment, the extent of development of the new faults is smaller

than that of the isotropic case except for their late activity (i.e. after 30 mm of total displacement). The length of new faults shows a trend similar to that of the experiments with one precut, i.e. they show a P/S ratio increase after they cross the precuts (Fig. 2.9b). This increase of the P/S ratio, however, occurs at different displacement values corresponding to the different times when the new faults cross the precuts. The DIP45_2PC are different from the DIP30_2PC at the final stage (Fig. 2.9g) because in the former new faults cross both precuts whereas in the latter they cross just the lower precut (Figs. 2.9g and 2.9j).

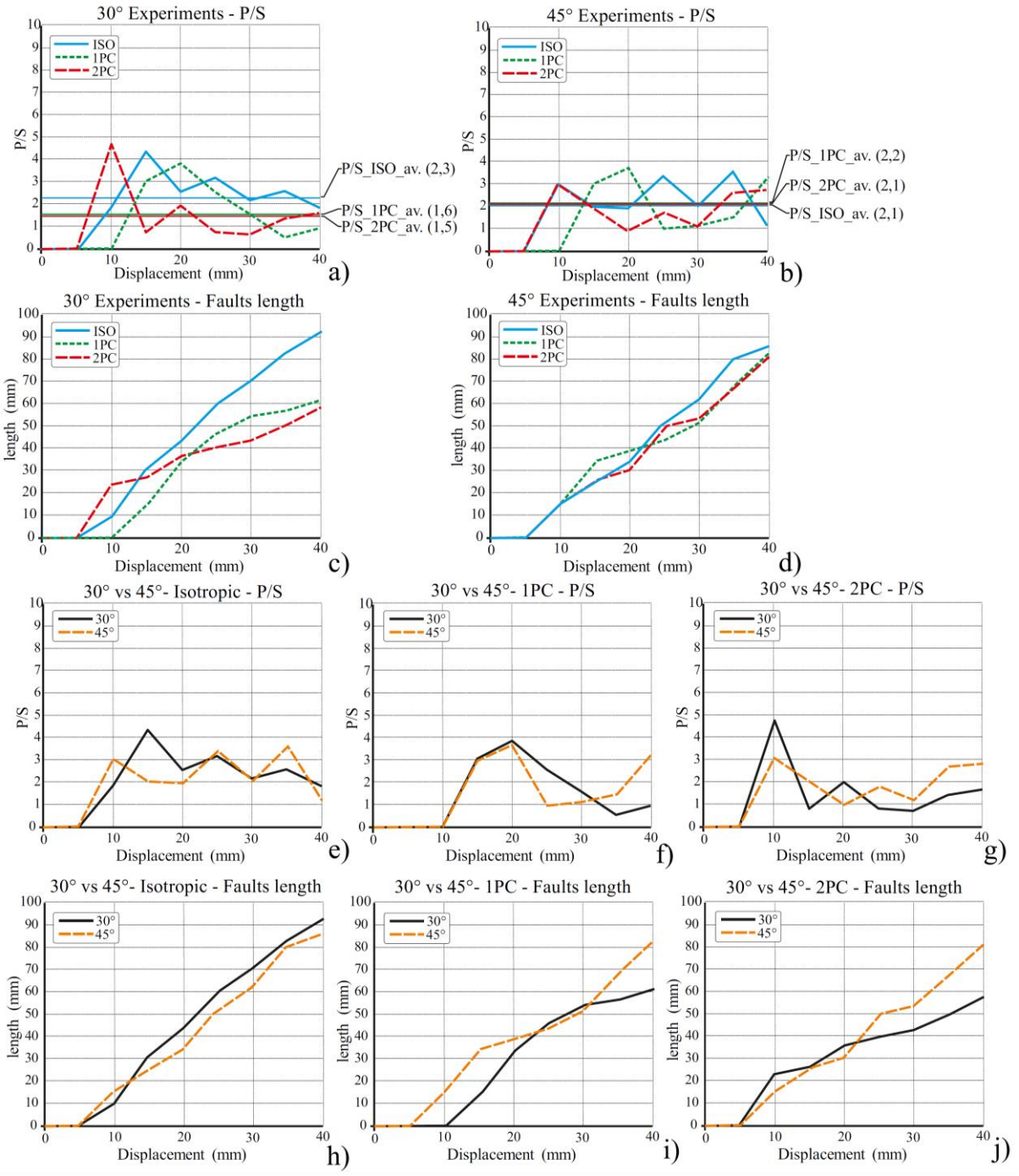

Figure 2.9. Propagation/slip ratio and fault length analysis: a) and b) P/S evolution for 30° and 45° dipping master fault, respectively; the average values of P/S of each configuration is also reported. c) and d) fault length evolution for 30° and 45° dipping master fault, respectively. e), f), and g) P/S comparison 30° vs 45°. h), i), and j) Fault length comparison 30° vs 45°. Each line derives from the average of three experiments per type.

2.3.4. Angle of incidence (AOI)

The previous section clearly illustrates that new faults in different experimental configurations cross the precuts at different values of total displacement. To understand the mechanisms leading to these different evolutionary trends we analyze the angle between the new faults and the precuts, i.e. the AOI (Figs. 2.2b and 2.10). To document the arrest of the new faults when their upper tip coincides with the precuts we measure the total length of the new faults starting from the hanging wall cutoff of the rigid block. By doing this we obtain the net length of the new faults.

In DIP30_1PC, the propagating faults are deflected along the discontinuity and new faults never cross it (Fig. 2.10a). The new faults reach the precut at 25 mm of total displacement and the AOI is 130°. At the end of the experiments the AOI drops to about 110° (Fig. 2.10a). In DIP30_2PC, the propagating faults reach the precut at 20 mm of total displacement and the AOI is 140°. Unlike the DIP30_1PC experiment, in DIP30_2PC the new faults cross the lower precut at the latest stages of deformation (after 35mm of total displacement) when the AOI is approaching 90° (Fig. 2.10b).

In DIP45_1PC the new faults reach the precut at 15 mm of total displacement and the AOI is about 120° (Fig. 2.10c). At 30 mm of total displacement and at an AOI of 90° the new faults cross the precut, implying that the stasis is very short relative to the 30° experiments. In DIP45_2PC the new faults reach the lower precut at 15 mm of total displacement and the AOI is about 115° (Fig. 2.10d). The stasis lasts until 20-25 mm of total displacement when the AOI is about 90°.

In summary, the new faults are able to cross the precuts when the AOI is about 90°. This seems independent from the dip of the master fault or from the amount of total displacement.

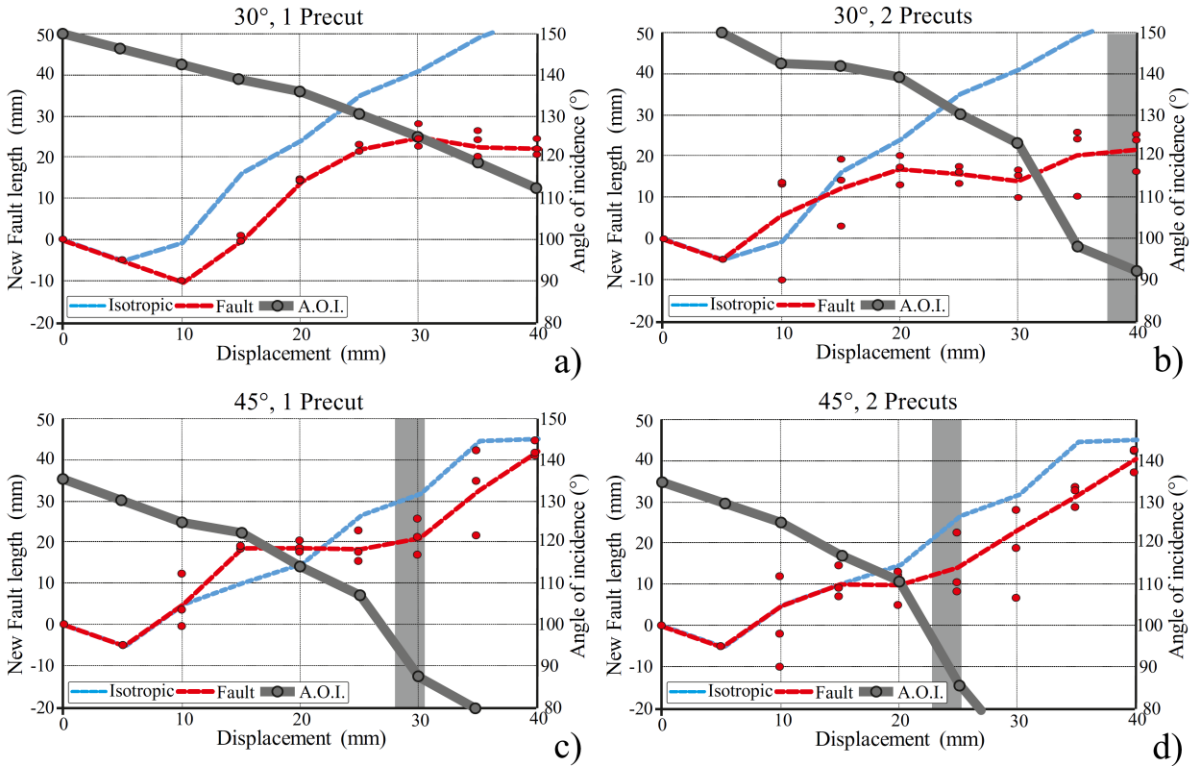

Figure 2.10. Evolution of the angle of incidence (AOI): a) and b) Experiments with master fault dipping 30°. c) and d) Experiments with master fault dipping 45°. The three red dots at every step of displacement indicate the length of new faults in the three experiments with the same setup. Red dashed lines represent the average at each step of the evolution of the length of new faults, and refer to the left vertical axis. Blue dashed lines indicate the evolution of the length of new faults of isotropic case (to be used as term of comparison). Grey lines indicate the variation of the AOI, and refers to the right vertical axis. Vertical, thick, grey bars mark the zone where the AOI is about 90°.

2.3.5. Fold evolution

This section presents data on the evolution of folds through a pairwise comparison of all the experiments (Fig. 2.11).In the experiments with the 30° dipping master fault the more open limbs are those seen in the isotropic case. In DIP30_1PC and DIP30_2PC experiments, we generally observe that the presence of discontinuities decreases the interlimb angle, i.e. the forelimb is slightly steeper, except for the initial stages (Fig. 2.11a). This is more evident comparing the single models configurations (Figs. 2.11c, 2.11d, 2.11e). In the first stages of the experiments with one discontinuity, the forelimb is slightly gentler than in the isotropic case because during the early phase of these experiments the flexural reactivation of the precut tends to enlarge the fold shape. In the middle stages of this experiment, however, the shape changes from wider to tighter; this occurs when the propagating faults are deflected along the portion of the precut that is reactivated with a dextral sense of shear (Fig. 2.11a; see also Fig. 2.5). This mechanism also gives way to a horizontal translation of the fold hinge

(Figs. 2.11a and 2.11c). The models with two precuts show a tendency similar to that of experiments with one precut (Figs. 2.11a and 2.11d). In detail, however, the horizontal translation of the fold hinge is less pronounced than in the experiments with one precut, and the forelimb is steeper (Fig. 2.11e). In general, neither in the experiments with one precut nor in those with two precuts the backlimb shows significant deviations with respect to the isotropic case (Figs. 2.11c and 2.11d).

In the DIP45 experiments the backlimb shows differences in the fold shapes between isotropic models and models with the precuts (Fig. 2.11b). In the latter, the backlimb difference with the isotropic case increases during deformation. (Figs. 2.11b, 2.11f, and 2.11g). As for the forelimb, it is steeper than in the isotropic cases, similarly to what is seen in the DIP30 experiments. Also in the DIP45 experiments the flexural reactivation of the discontinuities and the deflection of the propagating faults along them gives rise to a horizontal migration of the fold hinges (Figs. 2.11f, and 2.11g).

Comparing DIP_30 with DIP 45 models the isotropic experiments (Fig. 2.11i) differ significantly both in the backlimb (different vertical heights) and in the forelimb (different slope). In the experiments with one and two precuts (Fig. 2.11j, 2.11k), the differences in backlimb are substantially the same, whereas in the forelimb they tend to decrease in models with one precut (Fig. 2.11j) and become negligible when two precuts are present (Fig. 2.11k).

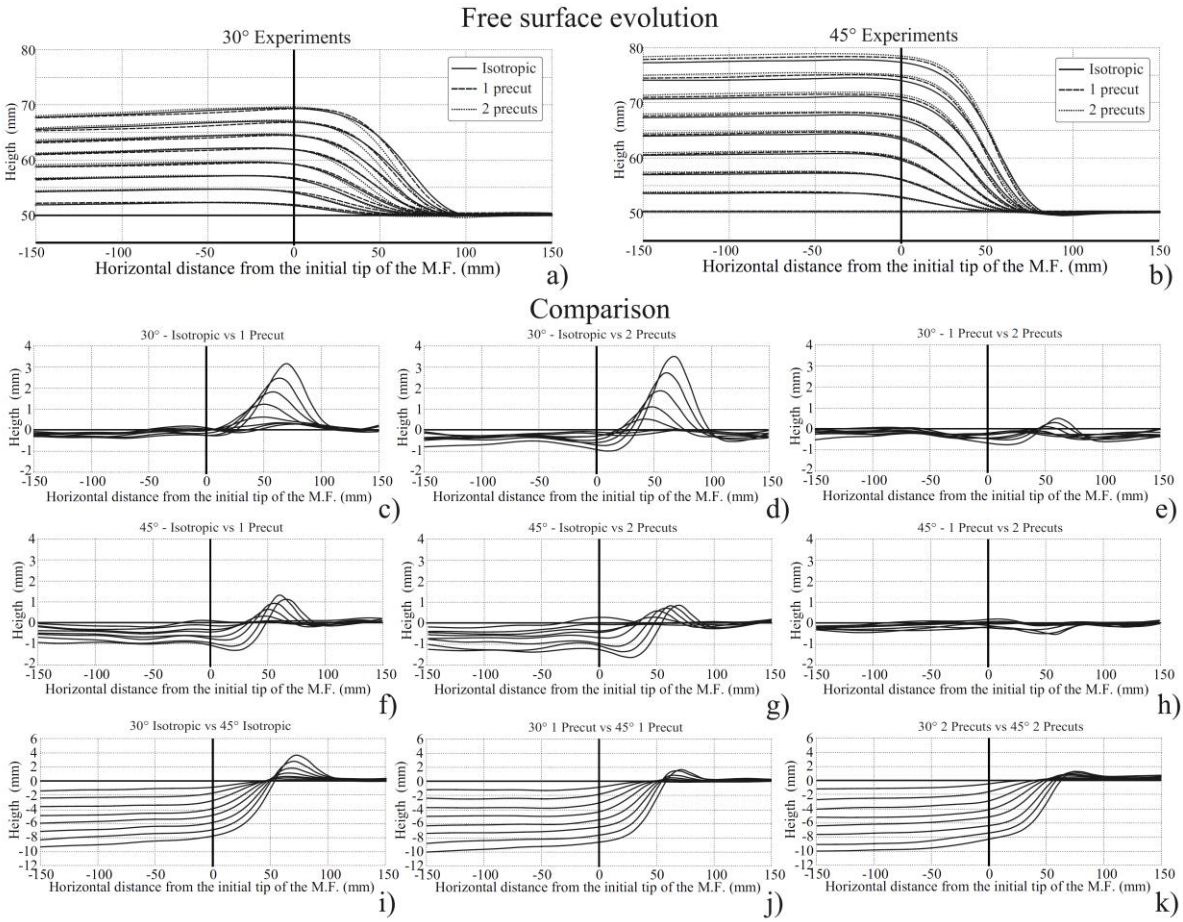

Figure 2.11. Fold evolution: Free surface evolution for a) DIP30 and b) DIP45 experiments, from zero to 40 mm of displacement. Each triplet of curves is relative to an interval of 5 mm of displacement. c), d) and e) Fold shape comparison of DIP30 experiments; f), g) and h) Fold shape comparison of DIP45 experiments. Each curve is the difference between the fold shapes of the two folds measured at that interval of displacement. i), j), and k) Comparison of experiments with the same configuration (isotropic, i; one precut, j; and two precuts, k) but with different master fault dip (30° vs 45°).

2.4. Discussion

The many differences between the isotropic models and the models with one or two precuts show how thin mechanical discontinuities - represented by precuts in our experiments - affect the evolution of fault-propagation folds as well as that of secondary brittle structures in a controlled environment. In particular, we observe that experiments with precuts differ from the reference isotropic experiment in terms of number, orientation, and propagation rate of new faults. Consequently, also the shape and evolution of the associated folds are different. To improve our understanding on how reverse faults evolve in the presence of such discontinuities in the real world, we compare the results from our experiments with common observations that are made in the investigation of natural cases. Then we analyze three different cases exploiting our findings.

2.4.1. Fault propagation

The experimental results on the development of new faults show how horizontal discontinuities (precuts) affect their evolution. In general, the propagation of new faults is faster when their upper tip is located below the precut, and accelerates as they approach the discontinuity (see section 2.3.3). When the new faults reach a discontinuity, they are deflected along it decreasing or even stopping their propagation. After crossing the discontinuity, the propagation rate tends to be more regular, i.e. similar to the propagation rate seen in an isotropic material. These observations are in agreement with those coming from analog models in extensional settings (Bonini et al., 2015) or inferred from mechanical models of reverse faults (e.g., Cooke and Pollard, 1997; Roering et al., 1997) and from field observation (Tavani et al., 2017). The acceleration of the propagation rate below a discontinuity is directly related both to the friction (e.g., Roering et al., 1997) and to the amount of slip along the fault (Bonini et al., 2015).

In all our experiments we observe that when new faults approach the discontinuities they are deflected along them. It is known that when a propagating fracture meets a thin, frictional discontinuity it may be stopped, it may be deflected, or it may be able to cross it. Such behavior depends on intrinsic properties of the discontinuity, i.e. its toughness and friction (Hutchinson, 1996; Roering et al., 1997; Xu et al. 2003; Wang and Xu, 2006). In our experiments only some portions of the discontinuities are reactivated, and these slipping portions change during the experiments. The shear strain rate analysis shows that new faults

are deflected along the slipping portions of the discontinuities with the same sense of shear, whereas they are stopped where the slipping portion of the discontinuities has the opposite sense of shear (Figs. 2.5 and 2.8). Hence, the sense of shear along a discontinuity plays a key role on the development of approaching faults. The fault deflection process may also explain why many active reverse faults in nature remain blind (Moss and Ross, 2011). For example, we may speculate that the presence of horizontal discontinuities above the tip of a propagating fault decreases the likelihood for that fault to breach and hence to produce earthquake ruptures at the ground surface.

In some of our experiments we observe that new faults cross the discontinuities, but this seems to happen only when and where new faults are almost perpendicular to the discontinuity, i.e. when the angle of incidence is about 90°.

2.4.2. Angle of incidence (AOI), the critical angle, and the crossing point

From the shear strain rate analyses (Figs. 2.5 and 2.8) we note that the point where new faults cross the discontinuities corresponds not only to the inflection point of the deformed discontinuities but also to the point where the sense of shear changes from dextral (on the right-hand side of the model) to sinistral (on the left-hand side of the model). This is the point where the slip along discontinuities is null. In general, the models show that when the new faults cross the discontinuities the AOI is about 90°, which can be considered as the critical angle for all our configurations. These results can be used when studying natural cases where fault location is controversial, debated, or unknown for lack of direct and unambiguous evidence of the fault geometry and extent. In seismic reflection data, for example, it is sometimes difficult to visualize or infer the fault traces and their tip points because seismic noise or disturbances (seismic disturbance zone) make any interpretation less objective in the vicinity of the faults (e.g. Kostenko et al., 2008; Hale, 2013; Iacopini et al., 2016). In these cases, along with the other factors controlling fault propagation (e.g. fault dip, slip rate, processes ahead of the fault tip), the critical angle may guide the interpretation, suggesting the point along a folded surface (discontinuity) where a propagating fault may be expected to cut through.

2.4.3. Folding evolution

The shape of the fault-related folds is one of the most widely used pieces of information to reconstruct the evolution of contractional structures, and their development is usually assumed as a linear process. Previous sections discussed the evolution of the new faults throughout the experiments with and without discontinuities (precuts) showing, among other observations, that the propagation rate of the new faults is variable depending on (i) their initial location, (ii) the number of discontinuities, and (iii) what portions of the precuts are reactivated during the experiments. Also, in the experiments with precuts we observe the formation of different kinds of secondary brittle structures (e.g., layer-parallel faults). The presence of discontinuities also affects the evolution of the folds associated with faulting.

Our results suggest that (i) backlimbs are rather insensitive to the activity of discontinuities, and that (ii) using the forelimb shape to derive fault parameters (dip, slip, etc.) can be misleading as mechanical discontinuities tend to conceal differences related to the dip of the ramping faults (Fig. 2.11). This occurrence has been observed also in studies based on mechanical models that have analyzed the role of weak layers or mechanically heterogeneous stratigraphy (e.g. Hardy and Finch, 2007; Albertz and Lingrey, 2012; Albertz and Sanz, 2012; Hughes and Shaw, 2015). This suggest that both thin frictional discontinuities and thin weak layers impact on the relationships between faults and folds. These findings are of paramount importance for example in calculating the slip rates of natural faults or deriving fault geometries from the shape of folded horizons.

2.4.4. Natural systems

As an application of the experimental results, we consider three natural cases where thin discontinuities potentially played a role during the evolution of the ramping faults. The first case is located in Southern California, San Fernando Valley, where active reverse faults are propagating and, in some cases, interacting with each other. In particular, we focus on the causative thrust fault of the 1994, Northridge earthquake (Fig. 2.12a). This thrust is blind and SW-dipping and its upper termination in its eastern portion is located close to another thrust system, dipping in the opposite direction, comprising the source of the Mw 7.1, 1971, San Fernando Earthquake (e.g. Hauksson et al., 1995; Mori et al. 1995; Huftile and Yeats, 1996). In its western portion, the upper tip of the Northridge thrust is located close to an imbricate

thrust system, the Santa Susana Fault (Fig. 2.12a). The steep attitude of the Santa Susana thrust ramps and the location of the upper tip of the Northridge thrust located in their synclinal area suggest that the Northridge thrust is a propagating fault (e.g. Davis and Namson, 1994). The upper part of San Fernando and Santa Susana thrust systems can be considered as thin mechanical discontinuities located above or near the upper termination of the Northridge thrust, as in our experimental setup. As shown by our experiments, the activity of the master fault (in this case the Northridge thrust) can be stopped by the discontinuities until it reaches the critical angle. According with our models, this critical angle should be 90°. The angle between the Northridge Thrust and the Santa Susana faults is higher than 90° and a stoppage of the Northridge upward propagation against these faults is feasible. We recall that our experiments show that flexural slip along the discontinuities occurs only when the propagating fault tip is below or coincident with the discontinuity (Figs. 2.5 and 2.8). During the 1994 earthquake sequence some shallow aftershocks were located in the area of the Santa Susana thrust systems and a flexural reactivation of these structures has been suggested (e.g. Davis and Namson, 1994). Following our experimental observations, this is coherent with a propagating fault stopped or deflected along discontinuities. In the eastern area (CS#2 in Fig. 2.12a), the angle between the Northridge and San Fernando thrusts is close to 90°, i.e. close to the critical angle, hence in this case we suggest that the San Fernando thrust does not currently represent an obstacle to the upward propagation of the Northridge thrust. The different interaction of the Northridge thrust with the structure dipping in the opposite direction can be confirmed also by looking at the different shape of the folds associated with the activity of the Northridge thrust and even by considering the distribution of coseismic slip observed during the 1994 earthquake sequence. The folds associated with the Northridge thrust exhibit a steeper forelimb in its western portion than in its eastern portion, similarly to the coseismic slip which was larger in the western area than in the eastern area (e.g. Carena and Suppe, 2002). In our experiments, when a propagating fault is below and close to a discontinuity it increases the propagation rate. In the Northridge case this implies that the fault could be more developed in the western area because of the presence and activity of pre-existing discontinuities (the Santa Susana fault system). In this view, these discontinuities favor the development of the propagating fault, that is not only larger but also more mature; in other words, the more slip accumulates on a fault, the more easily a coseismic rupture will propagate along that fault (e.g. Scholz, 2002).

The second case is located in the Po Plain, in Northern Italy (Fig. 2.12b). In this area some blind thrust faults are still active and generate significant earthquakes (e.g. Maesano et

al., 2015), as testified by the 2012 Emilia earthquake sequence during which the activation of two thrust ramps produced two mainshocks of Mw 6.1 and Mw 6.0 (e.g. Burrato et al., 2012; Bonini et al., 2014b; Bonini et al., 2016b). The thrust systems in this region involve two decollement levels, depicting classical ramp-flat trajectories (Fantoni and Franciosi, 2010; Ahmad et al., 2014; Toscani et al, 2014; Turrini et al., 2014, 2016). At a basin scale, the stratigraphic setting is rather uniform but the evolution of the various thrust system is rather different (see geological cross-sections in Fig. 2.12b). In the western zone the deeper thrust ramps appear to be deflected along an upper weak layer (cross-section #3 in Fig. 2.12b), whereas in the eastern zone the deeper thrust ramps cross the upper weak layer or form a short flat portion (cross-section #4 in Fig. 2.12b). This different behavior does not appear to be related to the different dip of the thrust ramps because both 45° dipping and the 20-25° dipping ramps are deflected along the upper weak layer in the western area, whereas in the eastern area steeper and less steep ramps cross the upper weak layer. Also the total displacement along the deeper ramp is not much different. The main difference between the two areas is related to the presence or absence of a fault along the upper weak layer, i.e. a flat portion of a thrust system developing above the upper decollement. The lower thrust ramps are deflected in the areas where a fault is present in the upper weak layer (see cross-section #3 in Fig. 2.12). As shown by our experiments, the tendency of the new faults to be deflected along the discontinuity is related, among others, to slip along the structures; in other words, slip along the discontinuity promotes the deflection. This observation is confirmed in the buried thrust systems of the Po Plain, where the deeper, propagating faults appear to be deflected along the upper thrust system.

The last case is located in the Western Kunlun Mountains front/Tarim Basin, at the very western end of China (Fig. 2.12c). Multiple décollement levels are seen in this region (see D1 and D2 in Cross-section #5 in Fig. 2.12c) where a duplex system has developed (Wang et al., 2013). The outermost thrust ramp is the causative fault of the 2015, Mw 6.5, Pishan earthquake, testifying that these structures are active (Lu et al., 2016; Li et al., 2016). The thrust system developed along both décollements levels D1 and D2. The upper level (D2) is folded by the deeper one (D1) and a series of linking thrusts developed between them, thus depicting the duplex system (Lu et al., 2016). Also in this case the structures that developed below a fault plane appear to have been deflected along it, confirming the observations made in the Po Plain in Italy and in our experiments, i.e. that propagating faults are easily deflected along fault-containing levels.

The buried duplex system of the Western Kunlun Mountains front and of the Tarim Basin illustrates how multiple reverse faults are sensitive to the presence of a mechanical discontinuity. In our experiments we find that new faults cross the discontinuities at a critical angle of about 90°. This occurred because we forced the master fault to be active throughout the experiment. In nature, especially in the most external sectors of contractional areas, a reverse or thrust fault is active until its activity maintains the critical shape of the entire system, for example if its activity is coherent with the Coulomb wedge dynamics (Chapple, 1978; Davis et al., 1983; Dahlen, 1984, 1990; Dahlen et al., 1984). The long-term activity of a thrust in a contractional wedge is mainly due to the friction along the basal detachment, the angle of internal friction of the material forming the wedge, the erosion, the syn-kinematic sedimentation, and the pore pressure. In a region with two decollements where a shallower and a deeper thrust system are acting, these factors may not allow a deeper thrust ramp to reach a critical angle with a shallower (roof) thrust because a younger thrust activates in the footwall of the older one before the critical angle is reached. As a consequence, a duplex system form. Our experimental results may suggest that a duplex system forms easily when the upper (roof) thrust develops before the deeper system (floor and link thrust) because the presence of a roof thrust facilitates the deflection of the link thrust.

In summary, comparing our experimental results with natural cases we notice that pre-existing fault planes act as thin, weak discontinuities, regardless of whether they are thrust ramps belonging to different thrust systems (e.g. San Fernando Valley in California) or shallower thrusts belonging to the same thrust system (e.g. Po Plain in Italy; Kunlun Mountains front and Tarim Basin in China). This is reasonable if we consider that a greater amount of stress is needed to induce slip along a weak layer rather than along a previously-formed fault which has already slipped. When we apply stress along a weak layer where no slipping surface already exists, part of the energy must be used to produce small cracks (nucleation phase; see the introduction), then to connect them and finally to create a fault plane (creation phase) and propagate it (propagation phase) inducing slip. In a region where fault planes already exist the applied stress can “immediately” induce slip, almost skipping the first phases. This reasoning has a direct impact in a hypothetical evolutionary scheme, where new, ramping faults evolve in regions where previously formed faults exists or do not exists in their propagation zones (Fig. 2.13), giving rise to different propagation rates and folding shapes.

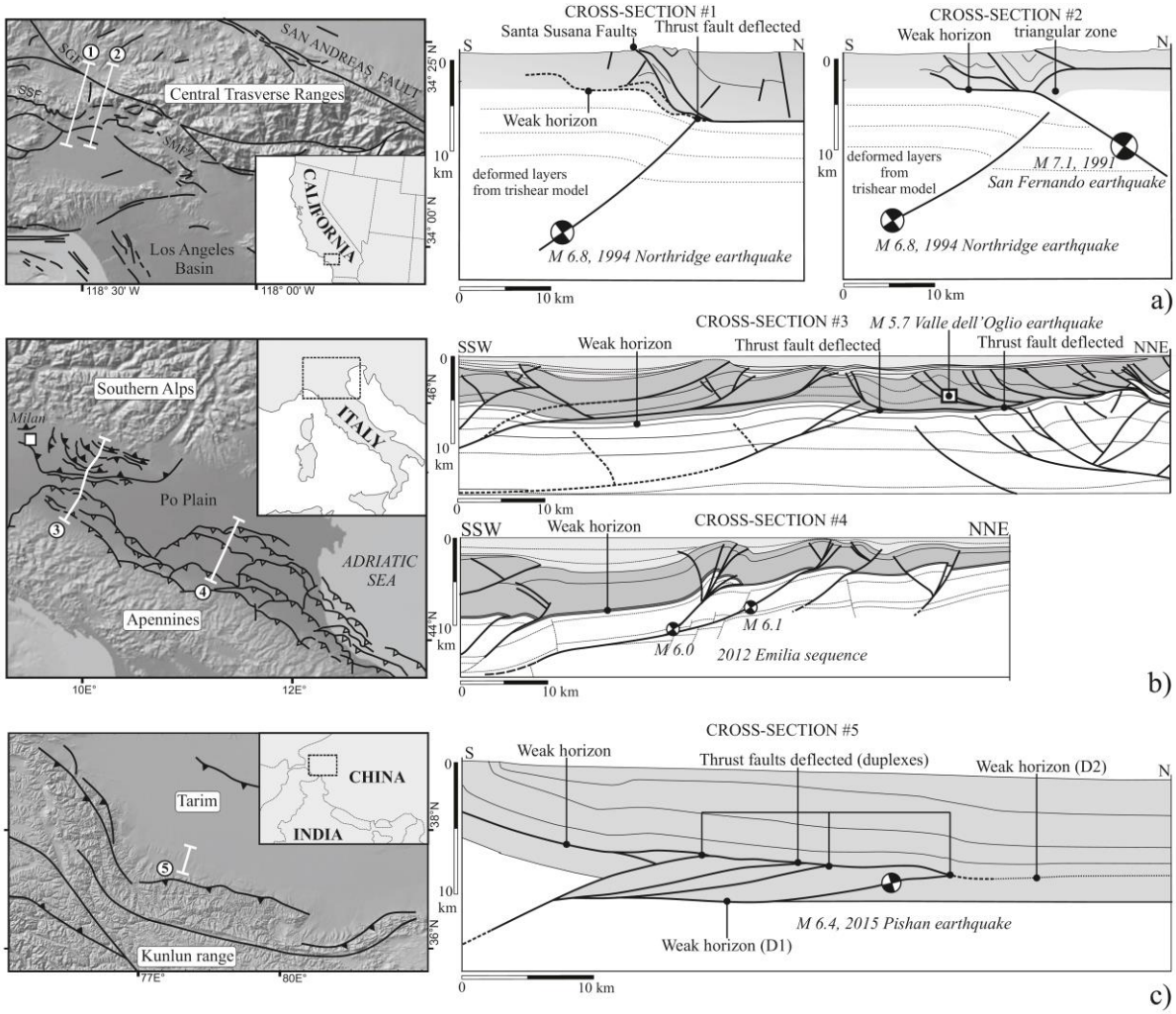

Figure 2.12. Naturel cases: a) Map view of the San Fernando Valley in southern California, and two cross section, located in the northern part, showing the structural setting of the Northridge thrust, the Santa Susana faults and the San Fernando thrust. Modified from Carena and Suppe (2002). b) Location map of the Po Plain in Italy; cross-section #3 and #4 shows the structural setting of the north-western and central areas respectively. Modified from Toscani et al. (2014) and Bonini et al. (2014b). c) Location map of the Western Kunlun Mountains front and Tarim Basin in China; cross-section #5 shows the deeper thrust system (to the left) and the shallower thrust system forming duplexes below the weak horizon D2 (modified from Li et al.;2016).

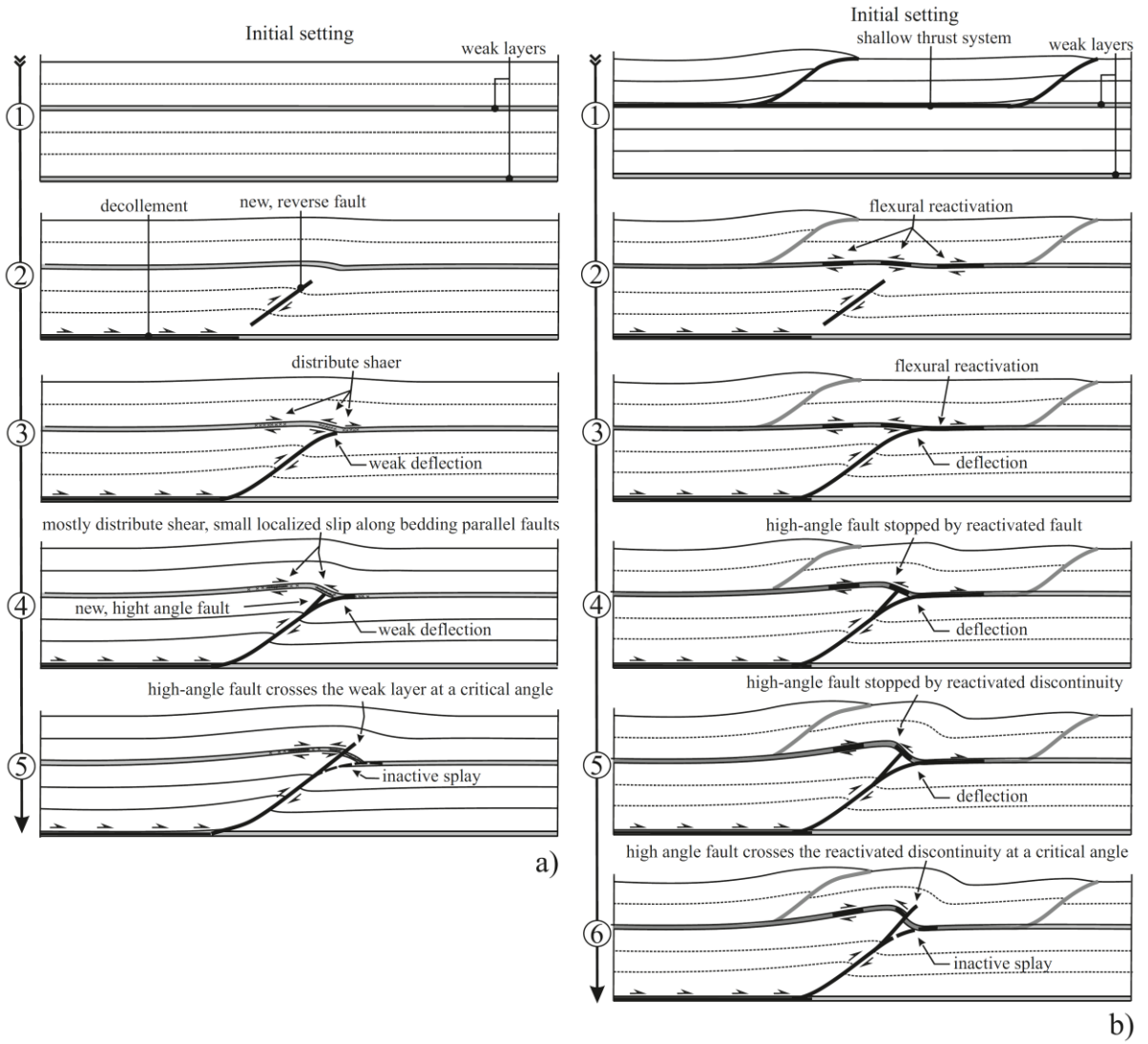

Figure 2.13. Hypothetical evolutionary scheme of two scenarios: a) the weak layer is not a pre-existing slipping surface. The propagation of a thrust creates distributed shear on it. The fault crosses the discontinuity at the stage 5. b) one of the two weak levels is a pre-existing slipping surface (shallow thrust system), the propagation of a new thrust causes the flexural slip reactivation and more slip is adsorbed by the discontinuity than in the previous case. The fault crosses the discontinuity at the stage 6.

2.4.5. Implications for kinematic models

Two seminal papers of the early 1990s proposed different solutions to address the relationships between folds and faults when slip along the fault plane decreases to zero. The first paper was published by Suppe and Medwedeff (1990), who transferred the kink-fold model developed for studying fault-bend folding to the case of fault-propagation folding. Such an approach, however, could not account for curved fold surfaces and for systematic variations in the thickness and dip of syn-tectonic strata. The second paper was published by Erslev (1991), who proposed a different approach based on the observation that in some

natural cases fold hinges tighten and converge downward to form a triangular zone. Erslev's study laid the basis for the trishear theory, that has since become extremely popular (e.g. Hardy and Ford, 1997; Allmendingeg, 1998; Zehnder and Allmendinger, 2000; Cardozo et al., 2003; Allmendinger et al., 2004, Cristallini et al, 2004; Jin and Groshong, 2006; Cardozo, 2008; Cardozo and Aanonsen, 2009; Welch et al., 2009; Cardozo et al., 2011; Liu et al., 2012; Pei et al., 2014; Zhao et al, 2017). The trishear theory predicts the presence of a triangular zone of distributed deformation whose apical angle is located on the tip of the propagating fault. In this triangular zone the displacement vectors vary linearly in magnitude and orientation - from a maximum in the hanging wall side, to zero in the footwall side (Allmendinger, 1998). The shape of the trishear zone is mainly controlled by two parameters: the propagation-to-slip ratio (P/S) and the size of the apical angle (Hardy and Ford, 1997; Allmendinger, 1998).

In all our experiments we observe gradual variations of the displacement vectors, both in orientation and module, from the hanging wall to the footwall (Figs. 2.4 and 2.7), a thickening of the footwall zone near the fault (Figs. 2.3, 2.6, and 2.11), and a smooth profile of the folds (e.g. Fig. 2.11). Such observations are all reminiscent of the trishear theory. In the isotropic models a quite regular triangular zone at the tip of the propagating faults is visible throughout the experiments (Figs. 2.4 and 2.7). Hence, the trishear method can be successfully applied to cases displaying a limited variability of the mechanical properties of the rocks hosting the propagating faults, as already suggested by previous studies (Cardozo et al., 2003; Hardy and Finch, 2007; Albertz and Sanz, 2012; Hughes and Shaw, 2015). In the non-isotropic experiments the reactivation of precuts has a deep impact on the displacement pattern (Figs. 2.4 and 2.7), showing a gradual variation of the displacement vectors from the hanging wall to the footwall and the thickening of the footwall zone (Figs. 2.3, 2.6, and 2.11), but it is not easy to identify a regular triangular zone at the tip of the propagating fault. This is especially evident in the experiments with two precuts (Figs. 2.3 and 2.6). In sections 2.3.1 and 2.3.2 we named this zone as segmented trishear zone. Segmentation is more evident when the tip of the propagating fault is still below the precuts. When the propagating fault reaches the precut and is deflected along it, our models are reminiscent of a fault-bend folding style, where the reactivated precuts mimic the generation of flat portions in the fault system". Hence, in layered rocks the kinematic models based on kink-fold models could be successfully applied (e.g. Hughes and Shaw, 2015). Notice that a variation of the displacement vectors is still visible, which is a typical characteristic of the trishear theory. An alternative solution to the utilization of kinematic models based on the trishear theory also for

layered rocks is to use the mechanical discontinuity as a lower boundary of the trishear zone, at least when the tip of the propagating fault coincides with the discontinuity. A similar solution has been recently proposed by Zhao et al. (2017). A fundamental question concerning practical applications of the kinematic models remains unanswered, however: for how long does the tip of the propagating fault coincide with the encountered discontinuity? While searching for an answer we may recall that in the kinematic analyses based on the trishear theory it is possible to impose a P/S variation while the system evolves; our experiments suggest during which phases of fault evolution the P/S should decrease, when it can be assumed to be zero, and when it should increase.

2.5. Conclusions

Our experiments allowed us to shed light on the role of thin, initially horizontal, frictional discontinuities on the evolution of reverse faults and associated folds. Our results suggest that such role is related to the intrinsic properties of the discontinuities (e.g. friction, toughness), and to their tendency to be reactivated. In general, the reactivation of discontinuities occurs when the upper tip of a propagating fault lies below them, or coincides with them. This reactivation tends to decrease the apical angle of the folds with respect to an isotropic case (i.e. without discontinuities), generating steeper forelimbs. The reactivation of the discontinuities, their characteristic slip distribution and their sense of shear control the ability of a discontinuity to deflect or stop a propagating fault. We may conclude that a slipping discontinuity with the same sense of shear of an approaching fault tends to deflect it until a critical angle of incidence is reached. The angle between the plane of the propagating fault and the slope of the folded discontinuity at its inflection point (i.e. the inflection point between the hanging wall anticline and the footwall syncline) is the critical angle, which in our models always approaches 90°. The inflection point of the folded discontinuity is also the preferred point where the propagating fault crosses the discontinuities.

Although our results provide new clues for an improved understanding of the evolution of faults and fault-related folds, we recall that they are necessarily based on a limited number of cases with intrinsic limitations (e.g. footwall and hanging wall simulated with two rigid blocks, number of the simulated discontinuities, and frictional properties of the discontinuity). To achieve a better understanding of the relationships between fault activity and pre-existing discontinuities, the approach and the analysis presented here must be applied to a larger number of models, encompassing a range of tectonic regimes and of natural cases.

Chapter 3. How do frictional surfaces affect the evolution of reverse faults? Insights from analogue-based numerical models

ABSTRACT

Reverse faulting frequently develops in mechanically anisotropic environments. Thus, the mechanical stratigraphy must plays a role on the development of faults, their geometry, and their tendency to propagate, reflecting also on the shape of the related folds. A specific kind of mechanical stratigraphy is represented by thin discontinuities, such us thin weak layers, detachments, or pre-existing faults. Analogue models of reverse faulting in mechanically anisotropic conditions have demonstrated that the fault propagation and the sequence of faulting are influenced by the localized shear strain occurring along thin discontinuities during folding. The amount of localized deformation that can be accommodated along such discontinuities may depend by their frictional properties. In this work, we study the impact of different frictional properties of thin, mechanical discontinuities (*layer-parallel interfaces* in this study) on the fault configurations and sequence of faulting revealed by analogue models, using numerical mechanical models based on the boundary element method. For different values of friction along the discontinuity and for a range of stages of the growing fold we perform a slip partitioning analysis to examine how the slip distributes along the faults and the interface with the progress of deformation. Furthermore, we apply work minimization approach, using the external work as term of comparison, to assess the conditions in which the faults efficiently accommodate the deformation together with the discontinuity disfavouring its crossing, and the conditions in which the faults are expected to cross it. Our results show that different frictional properties of the discontinuities impact on the slip distribution along the faults, thus on the propagation rate of the master fault, and on the tendency of the faults to cross the discontinuity.

3.1. Introduction

It is widely recognized that the mechanical stratigraphy plays a considerable control on faults and folds development in fault-related folding processes. Many studies investigated the impact of mechanical stratigraphy on faults development and folds shape in contractional regimes. Roering et al. (1997) found that the slip along bedding-plane impacts on reverse fault propagation. Albertz and Lingrey (2012) and Albertz and Sanz (2012) performed a structural and mechanical analysis to demonstrate how variable mechanical stratigraphy, fault dip, and layer detachments affect fault propagation and fold shape. Hardy and Finch (2006), and Hughes and Shaw (2015) identified the mechanical stratigraphy as the main factor defining the style of deformation (trishear to kink-band) in fault-propagation folding.

In a previous study (Chapter 2) Bonanno et al., 2017 performed a set of analogue experiments to analyze the evolution of reverse faults and related folds in presence of thin, initially horizontal, mechanical discontinuities. In their models have been observed a diacronous formation of two fault systems. In the early stages of the experiments, the new faults are generally curved and they connect the initial tip of the master fault with the horizontal discontinuities, i.e. the first set of new faults are deflected along the discontinuities (Fig. 2.3 and 2.6). During the formation of these curved faults the discontinuities were activated both with left lateral and right lateral slip. In later stages, a second set of new faults with a sub-rectilinear geometry branched off from the first curved faults up to the discontinuities (Fig. 2.3 and 2.6) accommodating even more deformation. At the same time, the activity along the curved faults and the right lateral movement of the discontinuities gradually decreased. Bonanno et al. (2017) observed that the second sub-straight faults crossed the discontinuities when their angle of incidence was sub-perpendicular (~ 90°), identifying a sort of critical angle in which the faults cross the discontinuities that repeats in all the different setups. This critical angle seems to be independent by the displacement on and the dip of the master fault. In a general view, analogue experiments have also demonstrated that the interaction curved fault/discontinuity decelerate the fault's propagation rate decreasing the propagation to slip ratio (P/S), and that the related fold changes its geometry in presence of reactivated discontinuities. Such a result can be potentially helpful for example to better locate the fault tips when in seismic reflection data is difficult to visualize the fault traces and their tips, or provide insights on the behaviour of the propagation rate in zones interested by thin mechanical discontinuities that can be implemented in kinematic modelling.

Although these findings provide new clues for an improved understanding of the evolution of faults and fault-related folds, they are necessarily based on a limited number of conditions with intrinsic limitations. For example, experimental constraints inhibit testing different frictional properties of the discontinuity. In nature, mechanical discontinuities may have different characteristics, for instance: a weak layer is more difficult to be activated than a pre-existing fault that has already slipped, or than a weak layer affected by overpressure fluids. Therefore, the frictional properties of the discontinuity can impact the evolution of the fault. The coefficient of friction determines the amount of slip accommodated along the discontinuities, and consequently, the friction may affect the geometry and the activity of the underlying faults and their tendency to propagate.

In order to investigate this aspect, we numerically reproduce the fault configurations and sequence of faulting revealed by clay analogue models of fault-propagation fold published in Bonanno et al. (2017). We use a Boundary Element Method (BEM) code in order to analyze the impact of different frictional properties of thin, mechanical, layer-parallel discontinuities on the propagation and evolution of new, reverse faults. We test different friction values along the discontinuity for a range of stages of the growing fold, which corresponds to different curvature of the layer-parallel discontinuity. For all the configurations, we perform a slip partitioning analysis to evaluate how the slip budget accommodates on faults in the different conditions. Furthermore, we apply the work minimization approach, using the external work as term of comparison, to establish the contribution, in terms of efficiency, given by the high-angle straight fault, i.e. the fault that crosses the discontinuity in clay analogue models. Interweaving the results of these two analyses, we determine the conditions at which a growing reverse fault interacts with a layer-parallel discontinuity transferring part of the slip budget along it, and the conditions at which the fault is expected to crosses it. Results suggest that the frictional properties on thin mechanical discontinuities affect the slip distribution along the underlying faults, which reflects on their tendency to propagate and to cross the discontinuities.

3.2. Method

3.2.1. BEM and Fric2D

Among different numerical modelling techniques used in rock mechanics, the Boundary Element Method (BEM) is considered well suited to investigate fault interactions and the associated deformation. Differently from other numerical modelling techniques, such us the Finite Element Method (FEM), in which the entire model requires discretization, BEM models have the great advantage of requiring only the discretization of the boundaries and discontinuities, e.g. faults (Crouch and Starfield, 1990). This is particularly advantageous for our modeling purpose to investigate faults interaction in homogeneous material, because errors due to discretization and approximation arise only along fault surfaces (Crouch and Starfield, 1990).

The BEM models applied in this study uses the numerical code Fric2D (Cooke and Pollard, 1997) to determine the stress and displacement on faults within the deforming system. Fric2D has been used to study fault behaviour (Cooke and Pollard, 1997; Roering et al., 1997; Cooke and Kameda, 2002), including bedding plane slip within folds (Cooke et al., 2000), damage development along frictional faults (Savage and Cooke, 2010), the energy of fault systems (Cooke and Murphy, 2004; Del Castello and Cooke, 2007; Cooke and Madden, 2014), and fault interactions (Cooke et al., 2011; McBeck et al., 2016). Fric2D uses continuum mechanics to solve the quasi-static equations of deformation for assigned boundary conditions, material properties, fault geometry, and fault friction. The material surrounding the fault system is isotropic and linearly elastic. Model boundaries and fault surfaces are discretized into linear elements of equal length. Fric2D uses the displacement discontinuity method where each element has uniform slip and opening along its length (Crouch and Starfield, 1990). Each fault within the model requires the prescription of two main constitutive properties, such us cohesion (c) and the static coefficient of friction (μ_s). Once the constitutive properties are set, the Fric2D code calculates the tractions and the displacement on faults within the deforming fracture system as well as boundaries. From the boundary tractions and displacements, we calculate the external work (W_{ext}), which reflects the total work required to move the boundaries to the imposed displacement. The fault conditions and external work are used to compare models with different friction along a layer-parallel interface and at different evolutionary stages of fault growth.

3.2.2. Work minimization

The principle of the work minimization assumes that fault systems evolve toward more efficient configurations that requires least total work. It provides an approach to predicting failure by assuming that the crust deforms in order to minimize the external tectonic work acting on it. Work minimization approach has been used extensively to study crustal deformation (see Cooke and Madden 2014 for a recent review), including the development of faults (Jones and Wesnousky, 1992; Cooke and Kameda, 2002; Oslon and Cooke, 2005; Maillot and Leroy, 2006), or to investigate the dynamics of accretionary systems (Gutsher et al., 1998; Hardy et al., 1998; Del Castello and Cooke, 2007; Cubas et al., 2008; Souloumiac et al., 2009, 2010; Yagupsky et al., 2014). Cooke and Murphy (2004) applied work minimization approach to predict fault evolution by assuming that systems deform to optimize the external work (W_{ext}) acting on the system. McBeck et al. (2016) developed a numerical tool (GROW) to predict faults and fractures growth by findings the fault propagation path and geometry that minimize the global external work. The external work is then a suitable parameter to predict the orientation and timing of fault propagation when using work minimization approach.

The external work, or total work, is the sum of five work terms that constitute the work budget required to deform a faulted area. They are internal work of deformation around faults, W_{int}, work against friction along faults, W_{fric}, work of seismic radiated energy, W_{seis}, work to initiate new faults or propagate existing faults, W_{prop}, and work against gravity, W_{grav} (Cooke and Murphy, 2004).

$$W_{ext} = W_{int} + W_{fric} + W_{seis} + W_{prop} + W_{grav}$$

Within Fric2D, the W_{ext} is determined from the product of the shear and normal tractions, τ and σ_n, and shear and normal displacements, u_s and u_n, integrated along the model boundaries, B:

$$W_{ext} = \oiint (\tau u_s + \sigma_n u_n) \mathrm{d}B$$

W_{ext} reflects the overall mechanical efficiency of the fault system, such that the most efficient fault propagation path will produce the maximum change in external work, ΔW_{ext}, which is calculated as the difference in W_{ext} before and after fault propagation (e.g. Cooke and Madden, 2014; McBeck et al., 2016).

In this study, the external work is not used to predict the fault propagation paths, which are instead taken from analogue models, but to predict the timing in which the high angle faults form and cross the layer-parallel interface for the different coefficient of friction simulated along it. Specifically, we calculate the external work before and after the propagation of the sub-straight, high-angle fault, which is observed crossing the discontinuity in clay analogue models. Than we calculate the difference ΔW_{ext}, in all the stages of folding and for each coefficient of friction along the layer-parallel interface. Analyzing the ΔW_{ext} derived from different models, we can assess how the development of the straight fault impact on the efficiency of the system at different stages of folding, and with different friction values along the layer-parallel interface. Comparison of the results of the external work with the experimental observations of analogue models of when second straight fault forms and crosses the discontinuity, reveals in which stages the straight fault develops and crosses the layer-parallel interface, for the different conditions of friction simulated along the layer-parallel interface.

3.2.3. Model setup

The boundary conditions, the shape, the mechanical properties and the geometries of the frictional surfaces in the numerical models were designed to mimic those observed in clay analogue experiments by Bonanno et al. (2017). The reference analogue models simulate two master faults dipping 30° and 45° with one initially horizontal discontinuity inserted in the clay pack (exp. 30°_1PC and 45°_1PC). The shape of and the displacement along the boundaries of the models reproduce the kinematic of the 30° and 45° deformation boxes: the left side and left base boundaries (Fig. 3.1) move up of 1 mm at 30° and 45° to the right, simulating the reverse movement of master faults dipping 30° and 45°. The frictional surfaces consist essentially in three main components: i) a layer-parallel interface that represents a thin mechanical discontinuity on which we test different friction values. ii) a curved fault with shallower dip at shallower depths that merges along the layer-parallel interface, which is the first fault formed in clay models; iii) a straight fault having the same dip as the master fault, (30° or 45°) that branches off from the curved fault and terminates against the layer-parallel interface (Fig. 3.1). The models are built to simulate three different stages of folding of the layer-parallel interface (Early, Middle and Late stage), representing three subsequent evolutionary stages of the host fold. The different shapes of the layer-parallel interface form three different angles of incidence (AOI) with the straight fault (130°, 110°, 90°). Each of the

numerical models simulates a small increment of deformation one of the folding stages thereby providing three snapshots of deformation for the evolution of the system. The material properties are established using the parameters of the wet clay with a 60% of water content by mass, and are: density of 1600 kg/m^3, Young's modulus of 0.025 MPa, Poisson's ratio of 0.2.

Before to analyse the impact of different frictional properties along the layer-parallel interface on the faults evolution, the numerical models are calibrated with the analogue models to assign, in addition to the material properties, also the starting value of the static friction coefficient μ_s at the layer-parallel interface (μ_{si}) and a value to maintain constant at the faults (μ_{sf}). The calibration is executed comparing the displacement field of numerical models with the reference analogue models (see section 3.3.1). The starting value attributed at the layer-parallel interface is μ_{si} = 0.1, and the constant value attributed at the faults is μ_{sf} = 0.2. Along the layer-parallel interface are then simulated different friction conditions, i.e.: 0.05, 0.1, 0.15, and 0.2 (Table 3.1) for the different configurations showed in Figure 3.1.

For all the stages of folding and for each friction value tested on the layer-parallel interface we analyzed the slip partitioning along the three frictional surfaces (curved fault, straight fault and layer-parallel interface) and the variation of the external work. Slip partitioning allows to analyze the variation in the slip budget distribution between curved fault, straight fault and layer-parallel interface in the different configurations of friction and stage of folding. The analysis of the external work is performed considering two fault configurations: a first, which incorporates the curved fault deflected along the layer-parallel interface (as observed in early stages of analogue models), and a second configuration in which a straight fault branches off from the curved fault and meets the layer-parallel interface (corresponding to the second main fault that forms in analogue models) (Fig. 3.8a; Table 3.2).

Each analysis provides the slip distribution and the external work produced by 1 mm of displacement imposed at the left side and left base boundaries.

Table 3.1. Summary of the numerical models used for the analysis of the slip partitioning.

Master fault dip	Stages of deformation	Prescribed interfaces	μ_{si}	μ_{sf}
30°	Early stage	Curved fault Straight fault L-P interface	0.05 0.1 0.15 0.2	0.2
	Middle stage			
	Late stage			
45°	Early stage	Curved fault Straight fault L-P interface	0.05 0.1 0.15 0.2	0.2
	Middle stage			
	Late stage			

Table 3.2. Summary of the numerical models used for the analysis of the external work.

Master fault dip	Stages of deformation	Prescribed faults	μ_{si}	μ_{sf}
30°	Early stage	Curved	0.05 0.1 0.15 0.2	0.2
		Curved, Straight		
	Middle Stage	Curved		
		Curved, Straight		
	Late stage	Curved		
		Curved, Straight		
45°	Early stage	Curved	0.05 0.1 0.15 0.2	0.2
		Curved, Straight		
	Middle Stage	Curved		
		Curved, Straight		
	Late stage	Curved		
		Curved, Straight		

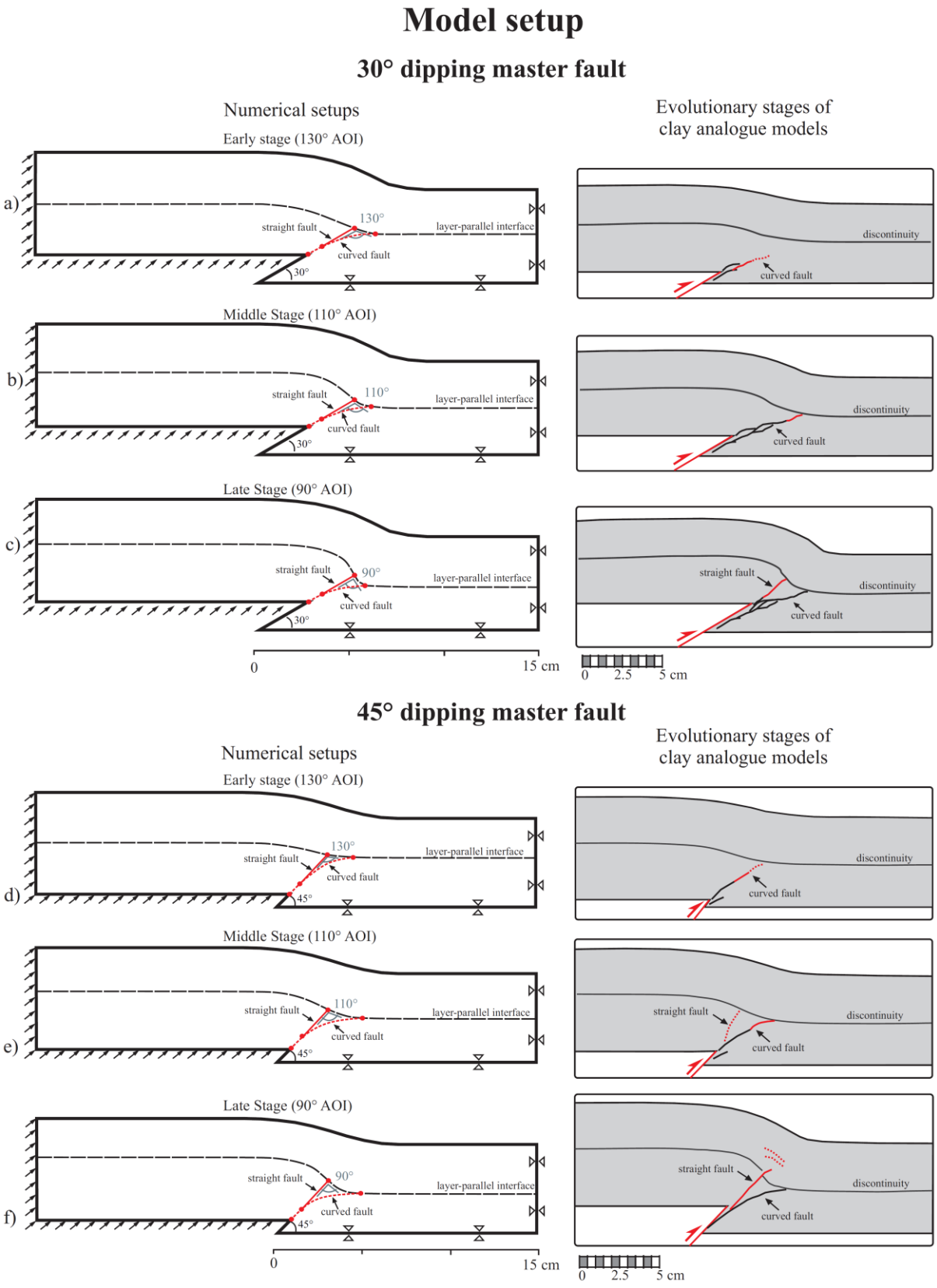

Figure 3.1. a), b), and c) Numerical setups of three evolutionary stages of a 30° dipping master fault and their corresponding stages in analogue models. d), e), and f) Numerical setups of three evolutionary stages of a 45° dipping master fault and their corresponding stages in analogue models. The left base and left side boundaries rise to the right simulating the reverse movement of the 30° and 45° dipping master faults.

3.3. Model results

3.3.1. Calibration

The calibration operations are executed analysing different coefficient of friction along the faults and the layer-parallel interface in order to get the best correspondence whit the displacement field of the reference analogue models. Along the faults, the values of friction of 0.1 and 0.2 show similar displacement field, although the displacement field with friction 0.2 shows a slightly wider trishear zone which best matches the displacement distribution of the reference analogue model (DIP45_iso) (Fig. 3.2a). Instead, the displacement field with friction 0.3 shows a too wider trishear zone because of the lower slip occurring along the faults, and a consequent prevalence of the off-fault deformation. Thus, the friction value of 0.2 along the faults is the value we maintain constant in all the analysis performed. The displacement field of the reference analogue model DIP45_1PC shows a net change in correspondence of the discontinuity (Fig. 3.2b). This net change, due to the localized shear strain occurring along it, find the best matching with the displacement field of numerical models with a friction value of 0.1 along the layer-parallel interface (Fig. 3.2b), indicating that the extension of the slipping portion along both the interfaces is similar. A lower value of friction (0.05) involve a too extended top to the hinterland reactivation of the interface, whereas with a higher value of friction (0.15) the reactivation of the interface is too localized compared to the analogue model.

The only noticeable difference among the analogue and numerical displacement fields resides in the top to the foreland movement of the upper block in the numerical model that is not as extended as in the analogue model (Fig. 3.2b).

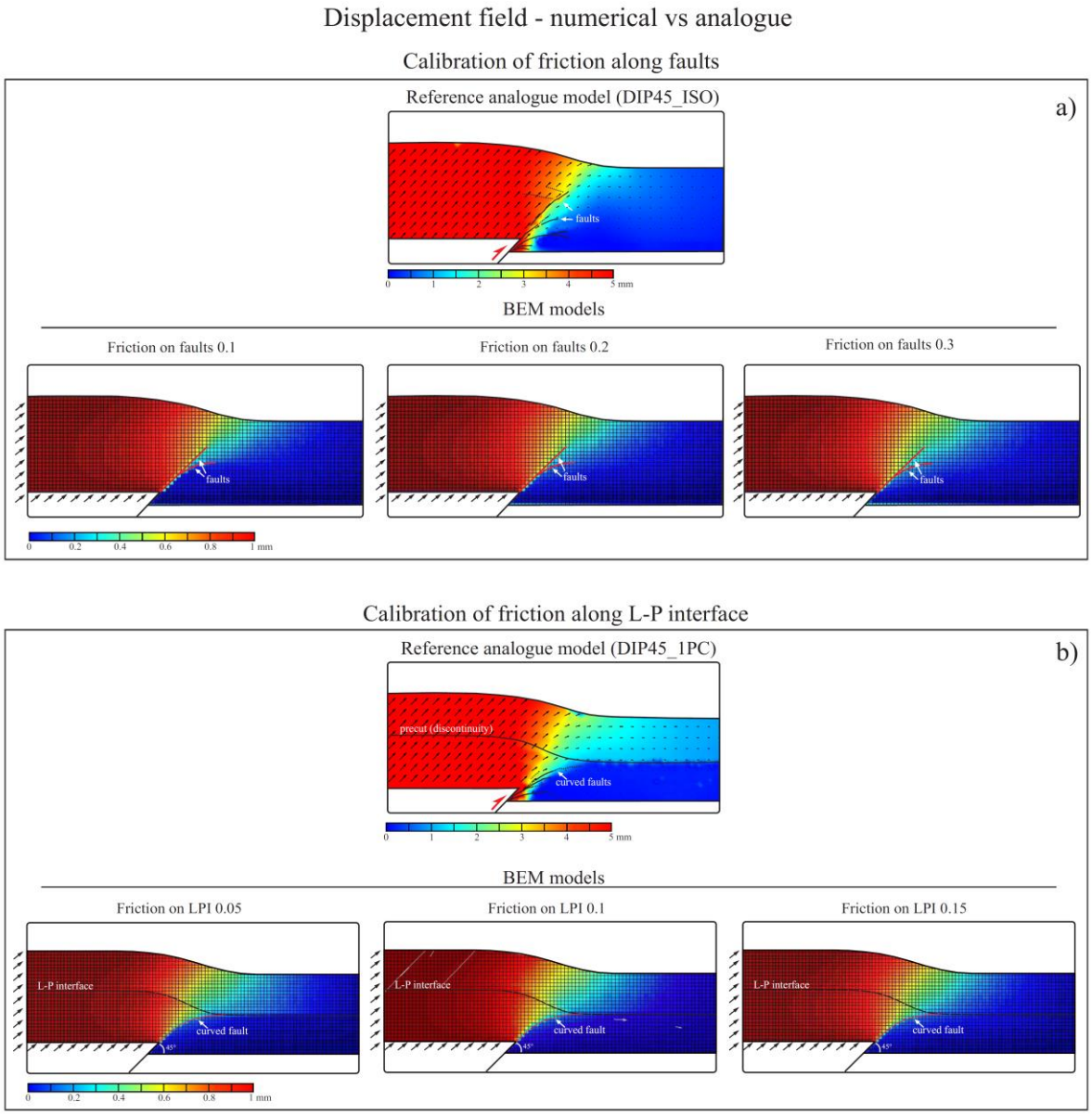

Figure 3.2. Comparison analogue vs numerical displacement field. a) Calibration of friction along faults testing three different values of friction (0.1, 0.2, and 0.3) b) Calibration of friction along the layer-parallel interface (L-P interface) testing three different values of friction (0.05, 0.1, and 0.15).

3.3.2. Slip partitioning

In this section we present the results related to the slip partitioning among the three frictional surfaces implemented in the models: the first curved fault, the second straight fault, and the layer-parallel interface. We also analyze the slip partitioning in terms of change in slip budget distribution in different setups, i.e. varying the coefficient of friction on the layer–parallel interface, and during different evolutionary stages, i.e. Early, Middle and Late stage.

3.3.2.1. 30° dipping master fault models

In the Early stage of the 30° models the slip along the curved faults decreases increasing the coefficient of friction along the layer-parallel interface, conversely, the slip increases on the straight fault (Fig. 3.3, and Fig. 3.4a for details). The same trend is preserved throughout the models, i.e. in the Middle and Late stage, although with different values (Fig. 3.3, and 3.4a). When the coefficient of friction along the layer-parallel interface is low (friction 0.05 in Fig. 3.3 and 3.4b), the slip along the curved fault slightly decreases only in the Late stage, whereas the straight fault does not show significant variations due to the stage of folding. Increasing the coefficient of friction along the interface, from Early to Late stage the slip along the curved fault decreases with a more noticeable variations (Fig. 3.3 and 3.4b), whereas the straight fault shows only a small increase of slip with the highest friction condition (friction 0.2 in Fig. 3.4b).

The slip along the layer-parallel interface shows both left lateral and right lateral sense of slip (Fig. 3.7). The left lateral slip is due to the flexural slip occurring along the top to hinterland sector of the interface, and it does not show particular variations due to the stage of folding. Conversely, the right lateral slip is least due to the flexural slip and mostly associated with the movement along the curved fault, which being merged with the layer-parallel interface, activates its top to foreland sector. The right lateral slip decreases from the Early to the Late stage for all frictional values (Fig. 3.7a) together with the decrease of slip along the curved faults, suggesting a direct correlation among them.

The general trend of the slip distribution in 30° models indicates that the slip along the curved fault mostly decreases with increasing the coefficient of friction and marginally later in folding, the slip along the straight fault mainly increases with higher friction on the interface, and the right lateral slip along the layer-parallel interface decreases in later stages of folding.

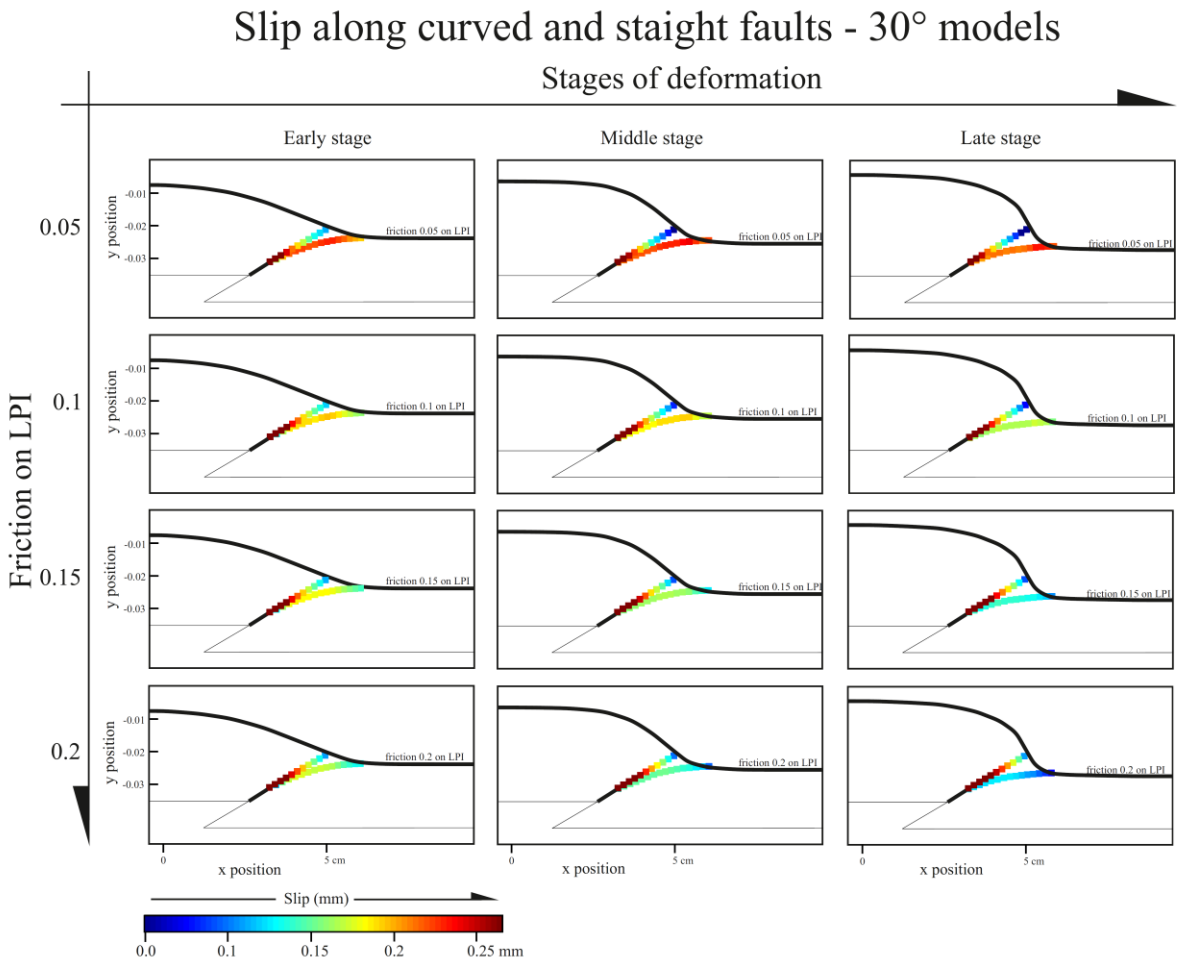

Figure 3.3. Slip along curved and straight faults in 30° dipping master fault models, for the three stages simulated (Early, Middle and Late stage) and with four different coefficient of friction along the layer-parallel interface (LPI) (0.05, 0.1, 0.15, 0.2). Red colors represent high slip, blue colors low slip.

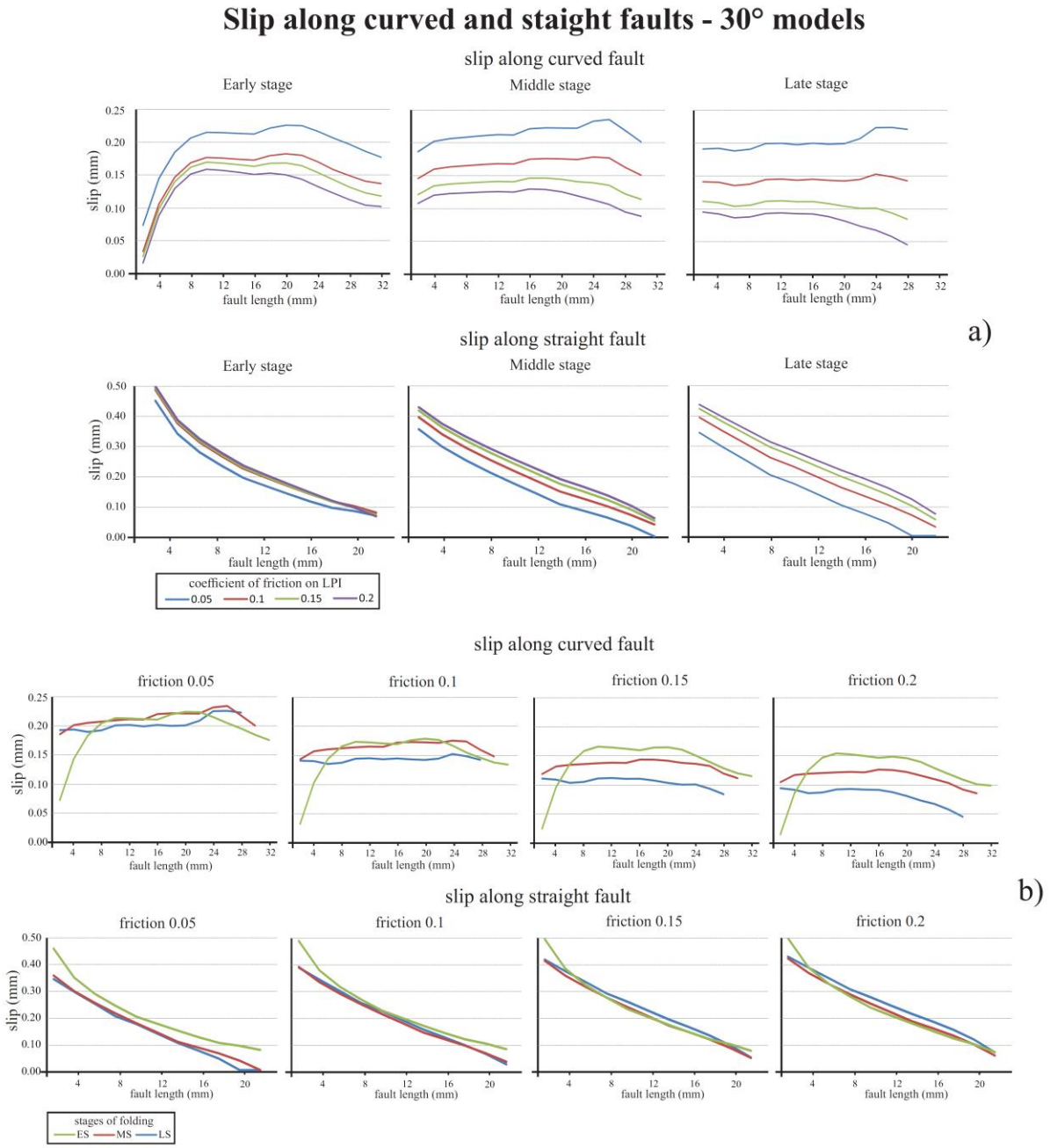

Figure 3.4. Detailed illustration of the slip along the curved and straight faults in 30° models. Figure a) illustrates the effect of different friction of the layer-parallel interface (LPI) on the slip along the curved (above) and straight (below) faults, for the three stages of folding. Figure b) illustrates the variation of slip due to the stage of folding for the curved (above) and the straight (below) faults, in the different conditions of friction along the LPI.

3.3.2.2. 45° dipping master fault models

In the Early stage, increasing the coefficient of friction along the layer-parallel interface the slip along the curved fault slightly decreases, conversely, the slip slightly increases on the straight fault (Fig. 3.5 and Fig. 3.6a for details). The Middle and Late stage shows the same trend but with more noticeable variations. To notice, in Middle and Late stages, with higher

friction along the interface increases the portion of the curved fault with zero slip (Fig. 3.5, and 3.6a). In all the conditions of friction along the layer-parallel interface, from Early to Late stage the slip decreases along the curved fault and increases along the straight fault.

The layer-parallel interface in 45° models, (Fig. 3.7b) shows a decrease of the right lateral slip from the Early to the Late stage of folding in all the friction conditions. With high friction condition (0.15 and 0.2), the right lateral slip in the Middle and Late stage is zero, coherently with the slip along the curved fault which shows zero slip on its upper portion (Fig. 3.5 and 3.6a).

The general trend of the slip distribution in 45° models indicates that the slip along the curved fault decreases with increasing the coefficient of friction and later in folding, conversely, the slip along the straight fault increases with higher friction and later in folding, and the right lateral slip along the interface decreases later in folding.

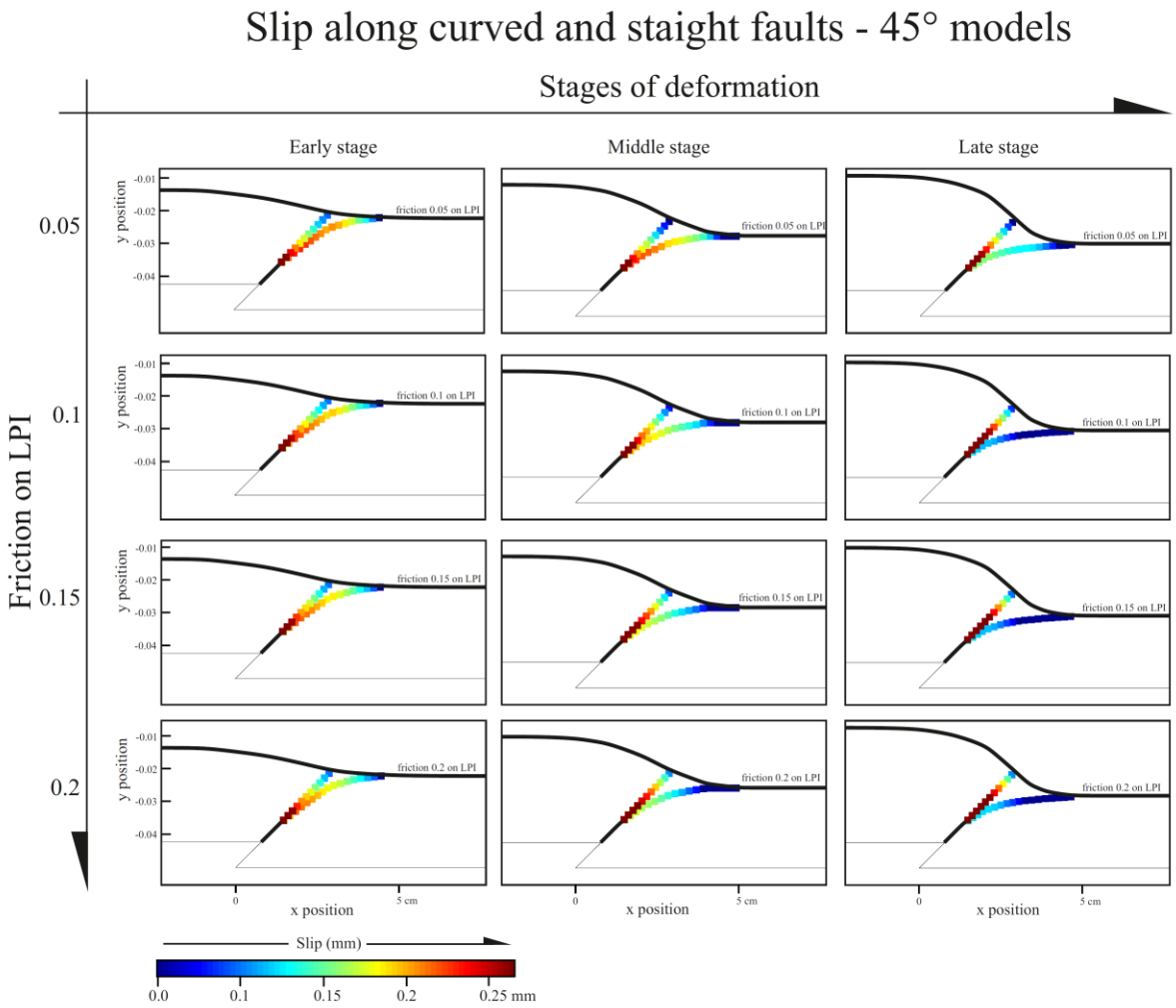

Figure 3.5. Slip along curved and straight faults in 45° dipping master fault models, for the three stages simulated (Early, Middle and Late stage) and in four different coefficient of friction along the layer-parallel interface (LPI) (0.05, 0.1, 0.15, 0.2). Red colors represent high slip, blue colors low slip.

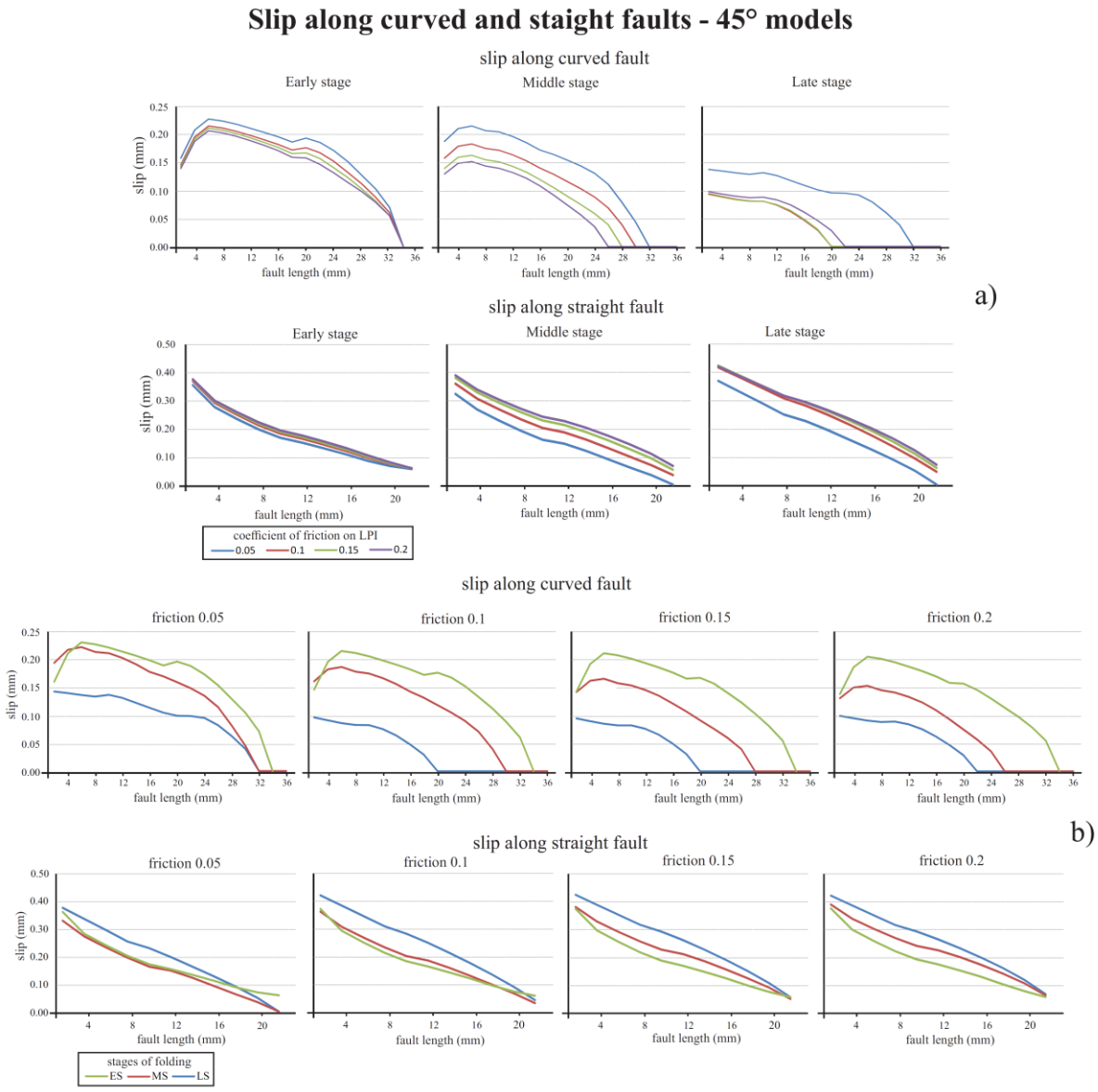

Figure 3.6. Detailed illustration of the slip along the curved and straight faults in 45° models. Figure a) illustrates the effect of different friction of the layer parallel interface (LPI) on the slip along the curved (above) and straight (below) faults, for the three stages of folding. Figure b) illustrates the variation of slip due to the stage of folding for the curved (above) and the straight (below) faults, in the different conditions of friction along the LPI.

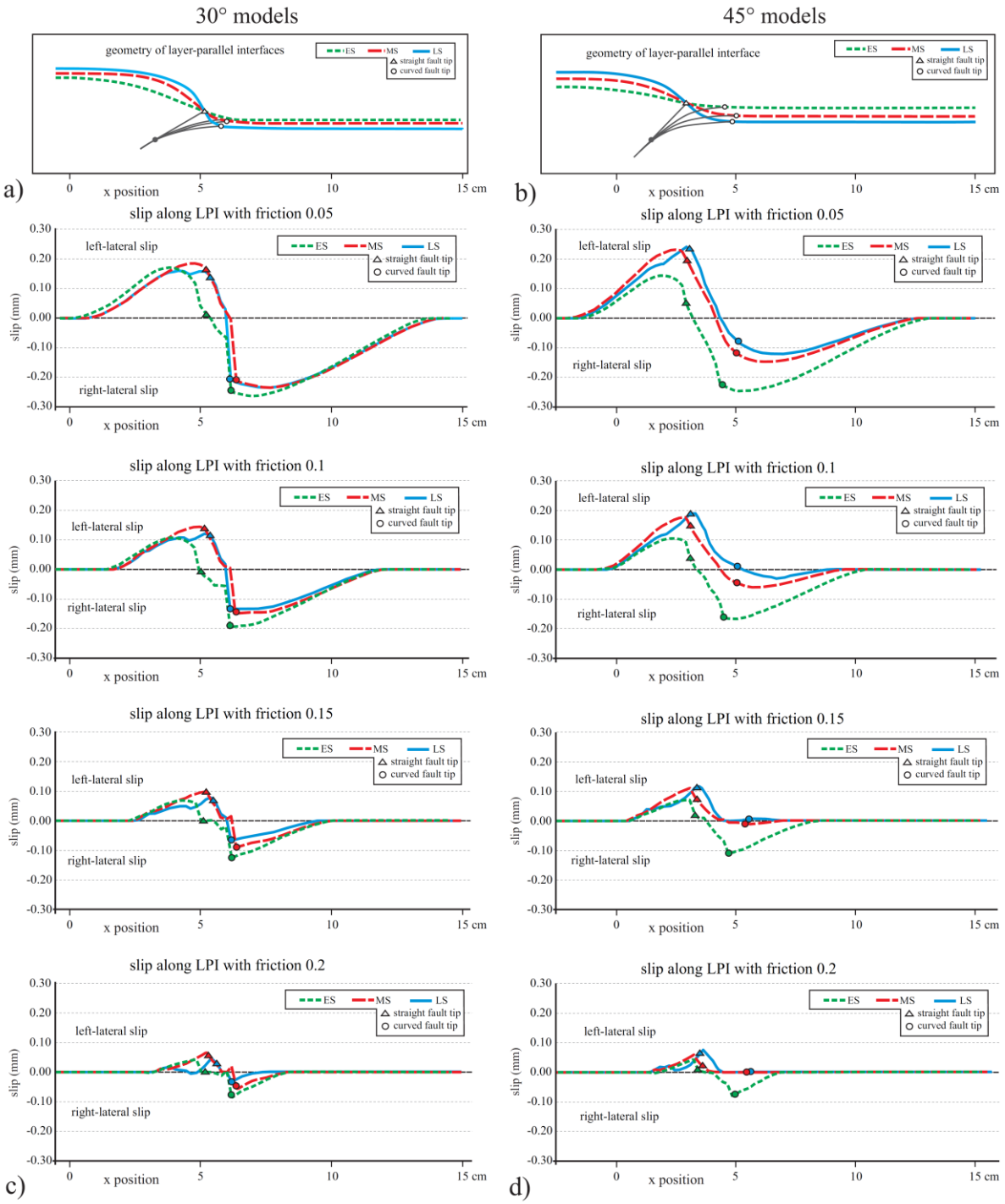

Figure 3.7. Slip along the layer-parallel interface (LPI). a) and b) report the geometry of the LPI for the three stages of folding in 30° and 45° dipping master fault models respectively. Fault tips positions are also reported. c) and d) Illustrate the variation of slip along the LPI due to the stage of folding in the four different conditions of friction (0.05, 0.1, 0.15, and 0.2) for 30° and 45° dipping master fault models respectively. Positive and negative values indicate left lateral and right lateral slip (in section view), respectively.

3.3.2.3. 30° vs 45°

The analysis of the slip partitioning shows differences in the slip distribution along faults and layer-parallel interface due to the master fault dip. In particular, with a lower dip of the master fault in 30° models, the interaction curved fault/layer-parallel interface is more efficient in accommodating deformation compared to the 45° models. As a result, at equal stage and friction, in 30° models the slip along the curved fault is always greater (Figs. 3.3, and 3.5), and consequently, the right lateral slip along the layer-parallel interface is always higher in both magnitude and extension, compared to the 45° models (Fig. 3.7c and d). The difference in dip between 30° and 45° models also reflects indirectly on the straight fault. In 45° models, the curved fault is more sensitive to the stage of folding because it changes more its orientation with folding compared to the curved fault in 30° models. This impacts on the straight fault which, at its time, shows noticeable variation due to folding. Conversely, in 30° models the less change in the orientation of the curved fault with folding involve less variation in slip on both curved and straight fault.

3.3.3. External Work

Figure 3.8 shows the ΔW_{ext} related to the development of the straight fault for different stages of folding and friction values along the layer-parallel interface. In all but the Early stage of folding with 30˚ master fault and low friction, the presence of the straight fault increases the efficiency of the system by accommodating deformation, namely reducing the external work applied at boundaries. This is consistent with the slip partitioning as efficient systems have greater fault slip and less off-fault deformation. In both 30° and 45° models, the ΔW_{ext} increases when the folding progresses, indicating that the development of the straight fault has the greatest impact on the overall efficiency of the systems later in folding. The external work is also sensitive to the friction along the layer-parallel interface. In both 30° and 45° models (Fig. 3.8b and c), and within each stage of folding, the ΔW_{ext} increases with increasing friction on the layer-parallel interface. This indicates that the development of the straight fault has a greater impact on the efficiency of the system when the friction on the layer-parallel interfaces is higher. This is due to the less slip that is accommodated along the layer-parallel interface with a high friction (see Fig. 3.7). The differences in ΔW_{ext} due to different friction values are larger in the Late stages than in the Early stages, indicating that the external work is more influenced by the friction in Late stages of folding. The Early stage

of 30° models with low friction (0.05 and 0.1; Fig. 3.8b) is the only case in which the inclusion of the straight fault decreases the efficiency of the system. At these conditions, most of the deformation is accommodated along the curved fault and the layer-parallel interface (see Fig. 3.3 and 3.7c) and their mutual interaction is still fairly efficient to not promote the formation of the straight fault.

The comparison of the 30° and 45° models shows that the formation of the straight fault causes a greater increase in efficiency in 45° setup for all the frictional values and in all the stages of folding.

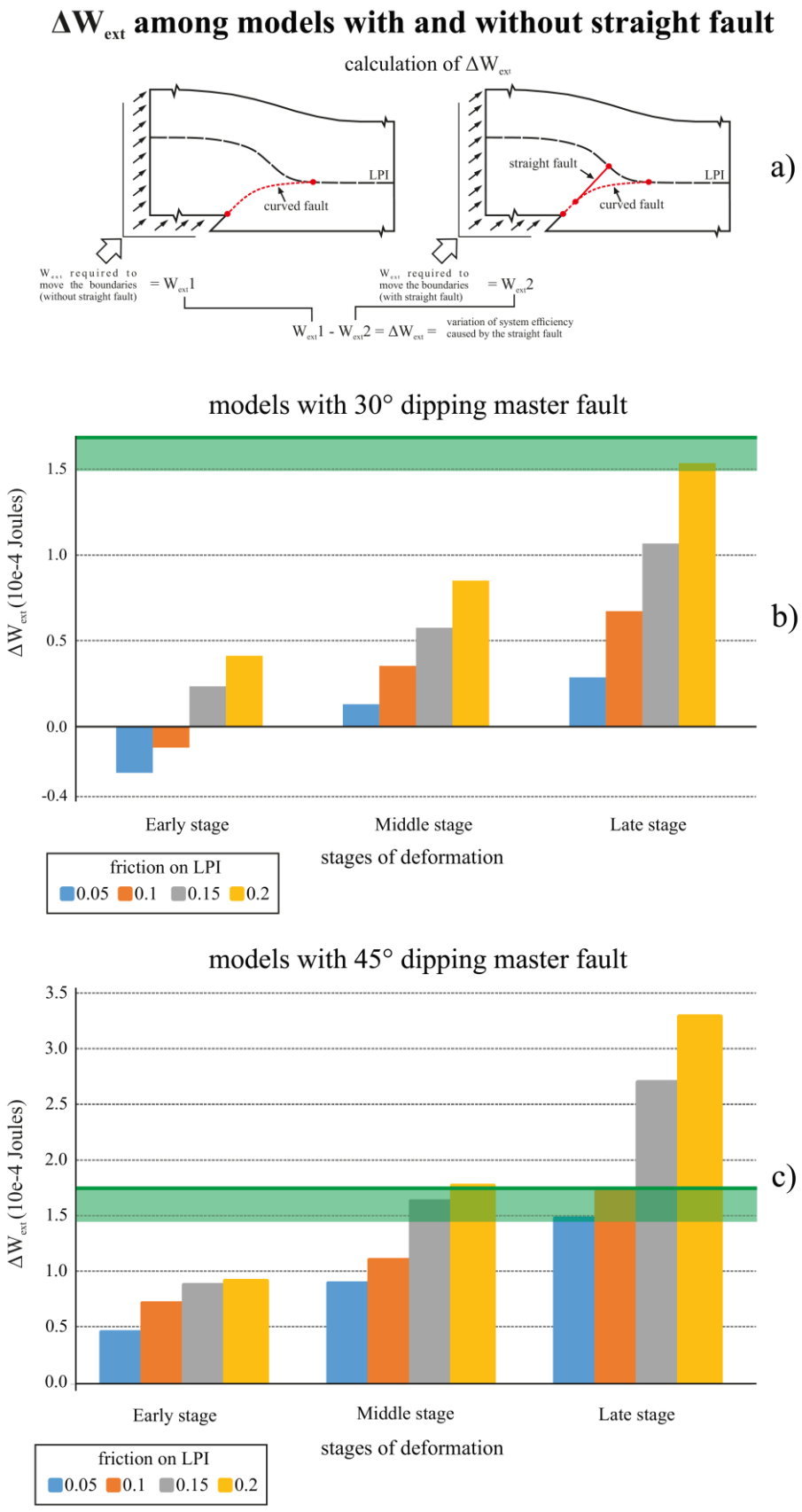

Figure 3.8. External work analysis. a) example of calculation of the ΔW_{ext}. b) ΔW_{ext} caused by the straight fault in 30° dipping master fault models. c) ΔW_{ext} caused by the straight fault in 45° dipping master fault models. Green line and bar represent the threshold value over which or near which the straight fault is expected to cross the layer-parallel interface.

3.4. Discussion

3.4.1. Slip evolution in numerical and analogue models

Clay analogue experiments illustrated in Bonanno et al. (2017) evolve with the formation of a first main fault having shallower dip at shallower depth that merges along the discontinuity. During the formation of the first main fault (curved fault), the discontinuity is activated with left lateral and right lateral slip. With the proceeding of the deformation, a second main fault with high-angle and a sub-straight geometry branches off from the first curved fault. This second fault become even more important in accommodating the deformation and, at the same time, the activity along the first deflected fault and the right lateral movement of the discontinuity gradually decrease. The second sub-straight fault crosses the discontinuity when the angle of incidence between them is about 90°, than it continues its propagation toward the surface forming splays.

The results obtained from numerical models are consistent with those observed in analogue models. During the Early stage, we observed that the curved faults accommodate more slip both in 30° and in 45° setups. The high slip of the curved fault reflects on the right lateral slipping of the layer-parallel interface which shows higher value in the Early stages (Fig. 3.7). Conversely, the straight fault shows relatively low slip because the curved fault more easily accommodates the displacement. The relatively secondary role of the straight fault in early stages of folding is also evident from the analysis of the external work (Fig. 3.8). Both in 30° and 45° setups the ΔW_{ext} is lowest, suggesting that the presence of the straight fault causes a small, or even negative in 30° dipping master fault setup, impact on the external work compared with later stages. The negative values of ΔW_{ext} in the Early stage of folding with 30˚ master fault and low friction (Fig. 3.8a), indicates that the straight fault should not forms because its presence increases the work required to move the boundaries. This is consistent with the results of analogue models where the sub-straight faults form in later stages (see Early stage in Fig 3.1a). Hence, in the Early stage, the interaction curved fault/layer-parallel interface is still fairly efficient that does not involve the development of the second straight fault.

During later stages, the slip increases along the straight fault and decreases along the curved fault due to the progressive reduced efficiency of the curved fault in accommodating the displacement imposed by the master fault. This reduced efficiency is caused by the different orientation at later stages of the fault with respect to the local stress field imposed by the activity of the master fault. The reduced efficiency of the curved fault impacts also on the

right lateral slip along the layer-parallel interface which progressively decreases. As a result of the reduced activity along both the curved fault and the layer-parallel interface, the straight fault having the same dip of the master fault becomes more efficient in accommodating the displacement. Also in this case, the analysis of the external work confirms this tendency: the external work is strongly optimized (high ΔW_{ext}) by the formation of the straight fault in Late stages of folding compared to Middle and Early stages (Fig. 3.8). The increased slip along the straight fault implies that the fault will have greater tendency to propagate across the layer-parallel interface because increases the stress intensity factor at a fault tip that drives fault propagation. These results suggest that in late stages of folding the fault is expected to propagate across the layer-parallel interface.

3.4.2. The effect of different friction values along the layer-parallel interface

The model results indicate the variation of the coefficient of friction along the layer-parallel interface as a first order factor affecting the slip distribution along the curved and straight fault. Both the 30° and 45° setups indicate that from low to high friction along the layer-parallel interface the slip decreases along the curved fault and increases on the straight fault. In the previous section (3.4.1) we maintained that the slip along the curved fault progressively decreases from Early to Late stage because it changes its orientation with respect to the local stress field, thus the decrease in right lateral slip along the interface later in folding is the effect of minor slip along the curved fault. However, the slip along the curved fault is, at its time, affected by the tendency of the interface to be moved, thus by the friction along it. Therefore, when the friction is low, the interface can easily be activated thus the curved fault shows higher slip. Conversely, when the friction is high, the layer-parallel interface accommodate minor slip and consequently, the slip along the curved fault decreases too. The mutual interaction between the curved fault and the layer-parallel interface influences the slip distribution along the straight fault. When the friction is low, the curved fault and the interface accommodate much of the deformation, and less displacement goes along the straight fault. This is also evident from the external work analysis: the formation of the straight fault causes a small increase in efficiency (small ΔW_{ext}) when the friction along the interface is low (Fig. 3.8). Contrariwise, with a higher friction along the interface, the deformation accommodated along it, and consequently along the curved fault, is lower, thus the straight fault become more efficient in accommodating the deformation. Also in this case, the external work reflects this behaviour: when the friction along the interface is high, the

development of the straight fault causes a higher increase in the efficiency of the system (high ΔW_{ext}). These results are consistent with those coming from mechanical models that investigated the effect of mechanical stratigraphy of reverse faulting (Hardy and Finch, 2007; Albertz and Lingrey 2012; Albertz and Sanz, 2012; Hughes and Shaw, 2015) or from field observations (Erslev and Mayborn, 1997; Tavani et al., 2017), when flexural slip occurs along bedding surfaces.

Summarizing, this findings suggest that with low friction values on the layer-parallel interface, the activity along the curved fault will last for a longer period accommodating a greater amount of slip together with the layer-parallel interface and consequently delaying the formation of the straight fault able to cross the layer-parallel interface (Fig. 3.9b). These results agree with previous studies which investigated the effect of bedding-parallel slip on thrust propagation (Roering et al., 1997; Cooke and Pollard 1997; Erickson et al., 2001). Natural analogues of mechanical discontinuities that recall low friction condition are: well-developed pre-existing slipping faults (e.g. shallow thrust systems), detachments, layers affected by overpressure fluids, or in general, all those structures that can accommodate inelastic deformation by localized shear. With higher friction on the layer-parallel interface, the activity along the curved fault decreases because the layer-parallel interface is more difficult to be activated (see slip along layer-parallel interface, Fig. 3.7). Consequently, the curved fault will be active for a shorter period accommodating minor slip and successive high-angle fault segments, branching off from the curved fault, will easily cross the layer-parallel interface reducing their period of interaction (Fig. 3.9a). Examples of natural analogues of discontinuities more difficult to activate by localized shear are intercalated weak layers in more competent rocks or faults with non-mature slipping surfaces. These findings are resumed in a hypothetical evolutionary scheme of two scenarios illustrated in Figure 3.9.

In terms of kinematic evolution, with low friction conditions, the efficient interaction between curved fault and interface implies a remarkable decrease in the propagation rate of the reverse master fault. Whereas, with high friction cases, the less efficient interaction among curved fault and interface implies a less decrease in the propagation rate of the reverse master fault. Considering these results, we can assert that the propagation rate of a reverse master fault will be affected by an overlying discontinuity as long as its intrinsic properties allow to accommodate slip, and that the decrease in the propagation rate is proportional to the capability of the mechanical discontinuity to accommodate localized deformation. These findings implement those of Bonanno et al. (2017) related to the change in the propagation to

slip ratio during deformation, and have a direct implication in kinematic models that use the activity of the faults to justify the deformation of folds in fault-propagation fold kinematic.

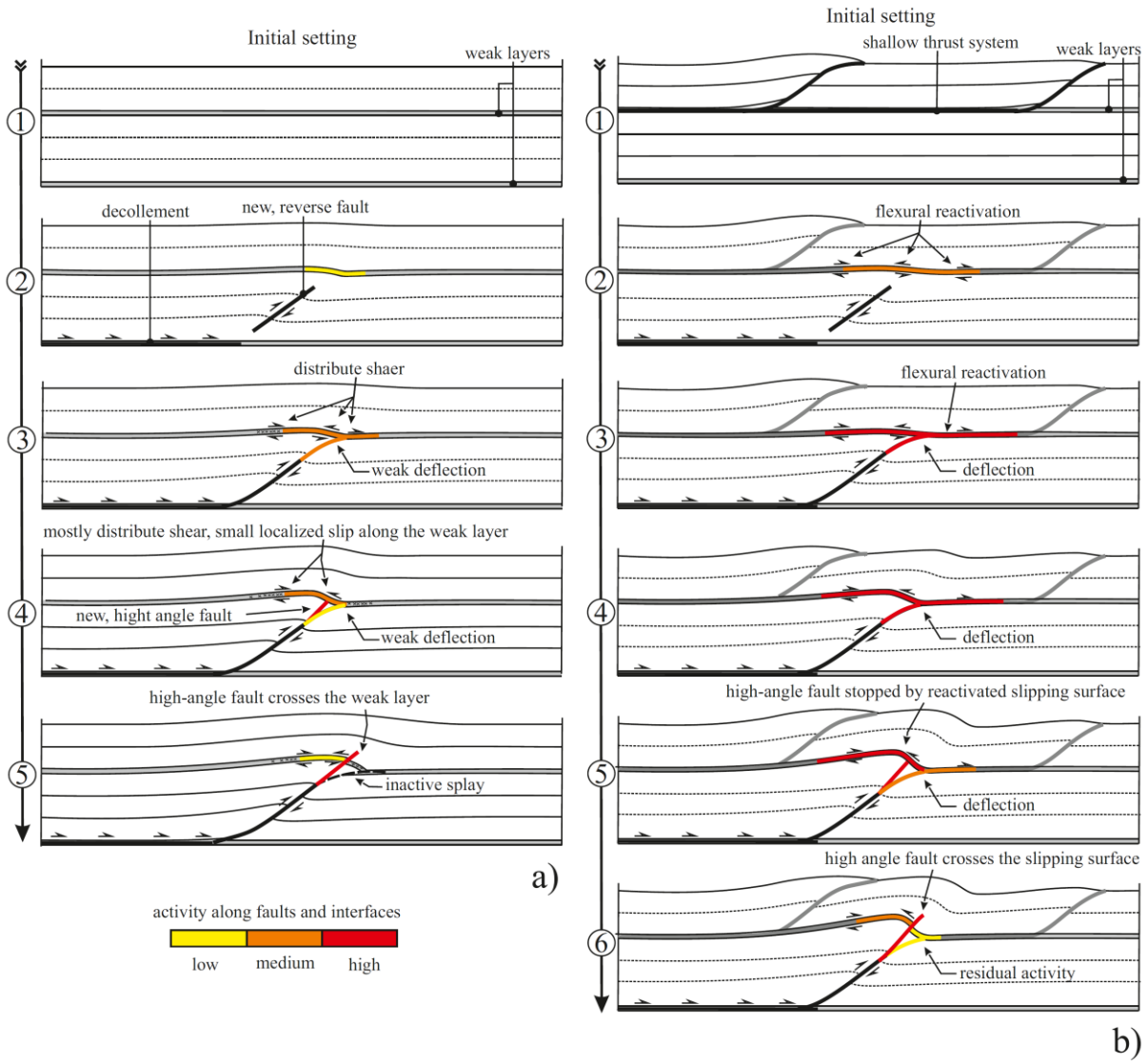

Figure 3.9. Hypothetical evolutionary scheme of two scenarios: a) the weak layer is not a pre-existing slipping surface. The propagation of a reverse fault causes a low reactivation of the interface and the curved deflection has, at its time, minor activity and for a shorter period. High angle fault crosses the interface at stage 5; b) one of the two weak levels is a pre-existing slipping surface (shallow thrust system). The propagation of a new reverse fault causes a stronger reactivation of the interface both in magnitude and extension. The curved deflection has higher activity and for a longer period. High angle fault crosses the interface at the stage 6. Modified from Bonanno et al. (2017).

3.4.3. The effect of the master fault dip

Different dips of the master faults involve second order variations in the slip distribution. The right lateral slip on the layer-parallel interface, mostly due to the activity of the curved fault, in 30° models shows higher values and for a longer portion of the interface

compared to the 45° setup (Fig. 3.7c and d) because of the greater component of horizontal movement. These results indicate that with a lower dip of the master fault, the curved fault will interacts for a longer period with the interface, accommodating together a largest amount of localized deformation and delaying the crossing of the interface compared to higher master fault dips. These observation agree with the results of the eternal work analysis: the development of the straight fault in 30° models causes a lower increase in efficiency (less ΔW_{ext}) compared to 45° setup in all the stages of folding and for each friction value along the layer-parallel interface (Fig. 3.8). These results highlight that the curved fault and the interface are more efficient in accommodating deformation when the dip of the master fault is lower.

What discussed in this section comply with the results of the propagation rate of the faults in analogue models (Chapter 2), in which the crossing of the discontinuities in DIP_30° experiments occurs later in folding compared to DIP_45° experiments.

3.4.4. The crossing of the layer-parallel interface

As described in the introduction, clay analogue models by Bonanno et al. (2017) reported that high angle, sub-straight faults cross the discontinuities when the angle among them (angle of incidence) is approximately 90°. In the numerical models, the straight fault and the interface form an angle of incidence of 90° in the Late stage (Fig. 3.1c and f). The Late stage of 45° models with coefficient of friction of 0.1 on the interface is the corresponding condition in which the rectilinear fault crosses the interface in the analogue experiments (45_1PC experiments in Bonanno et al., 2017). The slip partitioning in this stage shows a very low slip along the curved fault, with a long portion with zero slip (Fig. 3.5 and 3.6), and a related very low right lateral slip along the interface (Fig. 3.7d). Consequently, the straight fault has high activity. These conditions can supposedly identified as the slip budget distribution in which the straight fault should crosses the layer-parallel interface. The external work analysis indicates that in this condition the straight fault produces a ΔW_{ext} of about 1.7^{-4} Joules. This value can be considered as the threshold value of required increased efficiency, near which or over which the straight fault is expected to cross the layer-parallel interface. Figure 3.8 shows that in 45° models, different cases have a value of ΔW_{ext} close or above the threshold value, i.e. all the friction conditions in the Late stage and the two higher friction conditions (0.15 and 0.2) in the Middle stage (angle f incidence 110°). In 30° models, only the highest friction condition in the Late stage shows a ΔW_{ext} slightly lower to the threshold

value, thus the crossing of the interface in this stage is uncertain (Fig. 3.8b). In all the cases with values of ΔW_{ext} close or higher to the threshold value, the slip distribution indicates very low or zero slip along the curved fault and very low or mostly zero right lateral slip along the layer-parallel interface.

These results suggest that the critical angle of ~ 90° found in Bonanno et al. (2017) is characteristic of the frictional properties of the discontinuities implemented in the experiments. Higher friction values involve the crossing of the discontinuities in earlier stages, as observed in the Middle stage with high friction in 45° models, which correspond to an angle of incidence of 110°, and as discussed in the previous section (3.4.2).

3.5. Conclusions

This study investigated through BEM numerical models the effect of different frictional properties of thin mechanical discontinuities on the propagation of blind reverse faults, in fault-propagation fold style. The models numerically reproduce the fault configurations and sequence of faulting revealed by clay analogue models from Bonanno et al. (2017). Our results suggest that the frictional properties of thin mechanical discontinuities have a first order impact on the slip budget distribution along the faults. The friction affects the period of interaction among the faults and the simulated layer-parallel interfaces and it has a direct impact on the propagation rate of the reverse master fault. Specifically, the propagation rate decreases with increasing the capability of the mechanical discontinuity to accommodate slip. The dip of the master fault appears as a second order factor controlling the distribution of the slip budget, suggesting that mechanical, frictional discontinuities have, in general, a stronger impact with lower dips of the master fault. The crossing of the discontinuities is controlled by the interaction between the curved fault and the interface: when the activity along them is strongly reduced, the crossing of the discontinuity by high angle faults is promoted.

These findings provide insights on the behaviour of reverse faults in presence of different types of thin, mechanical discontinuities. The results can be used for new implementations of kinematic models of fault-related folding. New implementations should consider that part of the slip budget might be accommodated in the form of localized shear along such thin, slipping interfaces, causing the slowdown in the growth of the master fault. The measure of the slowdown will be proportional to the attitude of the thin interfaces to accommodate slip.

Chapter 4. Conclusions

The aim of this study has been to investigate the effect of thin, mechanical discontinuities on the development and propagation of reverse faults and their related folds, by means of analogue and numerical modeling.

Analogue models have reproduced the deformation mechanisms of two reverse master faults dipping at 30° in one case and 45° in another, in presence of one or two discontinuities implemented in a clay pack. The results suggest that both the faults development and the fold shapes are affected by the tendency of the discontinuities to be reactivated. i) The reactivation of discontinuities occurs when the upper tip of a propagating fault lies below them, or coincides with them. ii) This reactivation tends to decrease the apical angle of the folds with respect to an isotropic case (i.e. without discontinuities), generating steeper forelimbs, especially in experiments with two discontinuities. iii) The reactivation of the discontinuities, their characteristic slip distribution and their sense of shear control the ability of a discontinuity to deflect or stop a propagating fault modifying its propagation rate; iv) when the activity along the discontinuities decreases, high angle faults cross the discontinuities when the angle of incidence among them is ~ 90° (critical angle).

BEM numerical models, are based on the fault configurations and sequence of faulting observed in the analogue models, and they aimed to study what emerged from the analogue models simulating different frictional properties of discontinuities. The slip partitioning and external work analyses suggest that the frictional properties of thin mechanical discontinuities have a first order impact on the slip budget distribution along the faults and on the sequence of faulting. The friction affects the period of interaction among the faults and the simulated layer-parallel interfaces and has a direct impact on the propagation rate of the reverse master fault. Specifically, the propagation rate will decreases with increasing the capability of the mechanical discontinuity to accommodate slip. The dip of the master fault appears as a second order factor controlling the distribution of the slip budget, suggesting that mechanical, frictional discontinuities have, in general, a stronger impact with lower dips. As in the numerical experiments we introduce two secondary faults connected to the initial tip of the master fault, one straight fault and one curved fault, we observed that the crossing of the discontinuities is controlled by the interaction between the curved fault and the interface. Namely, when the activity along the curved faults is strongly reduced, the crossing of the discontinuity by straight, high angle faults is promoted. This implies that the crossing of the discontinuity can occur in different stages of deformation depending on the tendency of the discontinuity to be activated.

What reported in this thesis provides insights on the behaviour of reverse faults and in particular on the reverse fault-propagation folds kinematic in regions affected by thin, mechanical discontinuities. The results can be used for new implementations of kinematic models of fault-related folding that can better describe the deformation in region where reverse faults develop in mechanically layered rocks. As mentioned in the introduction and in section 2.4.5, the kinematic approach aims to reconstruct the deformation history of systems interested by folding and faulting. They correlate the observed fold shape whit the fault dip and slip at depth assuming a constant growth rate of fault (constant propagation to slip ratio). As demonstrated by mechanical and analogue models, and by field observation the growth rate of faults cannot be considered constant in mechanically layered systems. The results of the P/S analysis of analogue models indicate when the propagation of the fault should accelerate, decelerate or eventually, stop. The numerical analysis of variable friction along discontinuities integrates the results of analogue models suggesting the magnitude of the deceleration in fault propagation when it is interacting with the discontinuity. The magnitude of the deceleration will depends by the intrinsic characteristics of the discontinuity itself (i.e. its tendency to accommodate slip), and will determines the time span in which the fault remains confined below the discontinuity. Furthermore, the slip analysis on frictional interfaces (faults and discontinuities) indicates how the slip budget distributes in various stage of folding, with effects on the resultant fold shape. Therefore, the combination of analogue and numerical results can be converted to new numerical algorithms for kinematic modeling, which should consider modification in the fault propagation and fold shape due to localized shear on overlying frictional interfaces.

Other possible applications of the here presented findings can be in seismic lines interpretation operations, when the fault trace and its tip position is not clear because of the so-called “fault-shadow”; and in active tectonic studies, in explaining the interaction between main faults and secondary frictional surfaces.

References

Ahmad, M.I., Dubey, A.K., Toscani, G., Bonini, L., Seno S., 2014. Kinematic evolution of thrust wedge and erratic line length balancing: insights from deformed sandbox models. International Journal of Earth Sciences, 103, 1, 329-347, doi:10.1007/s00531-013-0947-8.

Albertz, M., Lingrey, S., 2012. Critical state finite element models of contractional fault-related folding: part 1. Mechanical analysis. Tectonophysics 576–577, 133–149.

Albertz, M., Sanz, P.F., 2012. Critical state finite element models of contractional fault-related folding: part 2. Mechanical analysis. Tectonophysics 576–577, 150–170.

Allmendinger, R.W., 1998. Inverse and forward numerical modeling of trishear fault-propagation folds. Tectonics 17, 640–656.

Allmendinger, R.W., Shaw, J.H., 2000. Estimation of fault propagation distance from fold shape: implications for earthquake hazard assessment. Geology 28, 1099–1102.

Allmendinger, R.W., Zapata, T., Manceda, R., Dzelalija, F., 2004. Trishear kinematic modelling of structures, with examples from the Neuquén Basin, Argentina. In: McClay, K.R. (Ed.). Thrust Tectonics and Hydrocarbon Systems. AAPG Mem. 82, 356–371.

Anderson, E.M., 1942. The Dynamics of Faulting (lst edn). Oliver & Boyd, Edinburgh.

Benesh, N., Plesch, A., Shaw, J., Frost, E., 2007. Investigation of growth fault bend folding using discrete element modeling: implications for signatures of active folding above blind thrust faults. Journal of Geophysical Research 112, 1–10.

Bergen, K.J., Shaw, J.H., Leon, L.A., Dolan, J.F., Pratt, T.L., Ponti, D.J., Morrow, E., Barrera, W., Rhodes, E.J., Murari, M.K., Owen, L.A., 2017. Accelerating slip rates on the Puente Hills blind thrust fault system beneath metropolitan Los Angeles, California, USA. Geology, v. 45, p. 227–230, doi:10.1130/G38520.1.

Bonanno, E., Bonini, L., Basili, R., Toscani, G., and Seno, S., 2017. How do horizontal, frictional discontinuities affect reverse fault-propagation folding? Journal of Structural Geology 102, 147-167.

Bonini, L., Di Bucci, D., Toscani, G., Seno, S., Valensise, G., 2014a. On the complexity of surface ruptures during normal faulting earthquakes: excerpts from the 6 April 2009 L'Aquila (central Italy) earthquake (Mw 6.3). Solid Earth 5, 389–408.

Bonini, L., Toscani, G., Seno, S., 2014b. Three-dimensional segmentation and different rupture behaviour during the 2012 Emilia seismic sequence (Northern Italy). Tectonophysics, doi: 10.1016/j.tecto.2014.05.006.

Bonini, L., Basili, R., Toscani, G., Burrato, P., Seno, S., Valensise, G., 2015. The role of pre-existing discontinuities in the development of extensional faults: An analog modeling perspective. Journal of Structural Geology 74. 145–158.

Bonini, L., Basili, R., Toscani, G., Burrato, P., Seno, S., Valensise, G., 2016a. The effects of pre-existing discontinuities on the surface expression of normal faults: Insights from wet clay analog modeling. Tectonophysics, doi:10.1016/j.tecto.2015.12.015.

Bonini, L., Toscani, G., Seno, S., 2016b. Comment on "The May 20 (MW 6.1) and 29 (MW 6.0), 2012, Emilia (Po Plain, Northern Italy) earthquakes: New seismotectonic implications from

subsurface geology and high-quality hypocenter location" by Carannante et al., 2015. Tectonophysics 688, 182-188.

Brace, W.F., Paulding, B.W., Scholz C., 1966. Dilatancy in fracture of crystalline rocks. Journal of Geophysical Research 71 (16), 3939–3953.

Brandes, C., Tanner, D.C., 2014. Fault-related folding: A review of kinematic models and their application. Earth-Science Reviews 138, pp. 352–370.

Burrato P., Vannoli P., Fracassi U., Basili R., Valensise G., 2012. Is blind faulting truly invisible? Tectonic-controlled drainage evolution in the epicentral area of the May 2012, Emilia-Romagna earthquake sequence (northern Italy). Annals of Geophysics, 55(4), 525-531, doi: 10.4401/ag-6182.

Cardozo, N., Bhalla, K., Zehnder, A.T., Allmendinger, R.W., 2003. Mechanical models of fault propagation folds and comparison to the trishear kinematic model. Journal of Structural Geology 25, 1–18.

Cardozo, N., 2008. Trishear in 3D. Algorithms, implementation, and limitations. Journal of Structural Geology 30, 327–340.

Cardozo, N., Aanonsen, S., 2009. Optimized trishear inverse modeling. Journal of Structural Geology 31, 546–560.

Cardozo, N., Jackson, C.A.L., Whipp, P.S., 2011. Determining the uniqueness of best-fit trishear models, Journal of Structural Geology 33, 1063–1078.

Carena, S., Suppe, J., 2002. Three-dimensional imaging of active structures using earthquake aftershocks: The Northridge thrust, California. Journal of Structural Geology 24, 887–904, doi:10.1016/S0191-8141(01)00110-9.

Cartwright, J.A., Trudgill, B.D., Mansfield, C.S., 1995. Fault growth by segment linkage - an explanation for scatter in maximum displacement and trace length data from the canyonlands grabens of SE Utah. Journal of Structural Geology 17 (9), 1319–1326.

Chapple, W.M., 1978. Mechanics of thin-skinned fold and thrust belts. Geological Society of America Bulletin, v. 89, no. 8, p. 1189–1198, doi:10.1130/0016-7606(1978)89<1189 :MOTFB>2.0.CO;2.

Chester, J.S., Chester, F.M., 1990. Fault-propagation folds above thrusts with constant dip. Journal of Structural Geology 12, 903–910.

Cooke, M.L., Pollard, D.D., 1997. Bedding-plane slip in initial stages of fault-related folding. Journal of Structural Geology 19 (3), 567–581.

Cooke, M. L., Kameda, A., 2002. Mechanical fault interaction within the Los Angeles Basin: A two-dimensional analysis using mechanical efficiency. J. Geophys. Res., 107(B7), 2146.

Cooke, M.L., Murphy, S., 2004. Assessing the work budget and efficiency of fault systems using mechanical models. J. Geophys. Res. 109.

Cooke, M.L., van der Elst, N.J., 2012. Rheologic testing of wet kaolin reveals frictional and bi-viscous behavior typical of crustal materials. Geophysical Research Letters 39, doi:10.1029/2011GL050186.

Cooke, M.L., Madden, E.H., 2014. Is the Earth lazy? A review of work minimization in fault evolution. J. Struct. Geol. 66, 334–346.

Cooke, M. L., Mollema, D., Pollard, D.D., Aydin, A., 2000. Interlayer slip and joint localization in East Kaibab Monocline, Utah: Field evidence and results from numerical modeling, in Forced Folds and Fractures, edited by J. W. Cosgrove and M. S. Ameen. Geol. Soc. Spec. Publ. 169, 23– 49.

Cooke, M.L., Islam, F., McGill, G., 2011. Basement controls on the scale of giant polygons in Utopia Planitia, Mars. J. Geophys. Res., 116, E09003.

Cooke, M.L., Schottenfeld, M.T., Buchanan, S.W., 2013. Evolution of fault efficiency at restraining bends within wet kaolin analog experiments. Journal of Structural Geology 51, 180–192.

Corti, G., Bonini, M., Conticelli, S., Innocenti, F., Manetti, P., Sokoutis, D., 2003. Analogue modelling of continental extension: a review focused on the relations between the patterns of deformation and the presence of magma. Earth-Science Reviews 63, 169–247.

Cristallini, E.O., Giambiagi, L., Allmendinger, R.W., 2004. True three-dimensional trishear: a kinematic model for strike-slip and oblique-slip deformation. Geol. Soc. Am. Bull. 116, 938–952.

Crouch, S.L., Starfield, A.M., 1990. Boundary Element Methods in Solid Mechanics, Unwin Hyman, Boston, Mass.

Cubas, N., Leroy, Y.M., Maillot, B., 2008. Prediction of thrusting sequences in accretionary wedges. J. Geophys. Res. 113.

Dahlen, F.A., 1984. Non-cohesive critical Coulomb wedges: An exact solution. Journal of Geophysical Research, v. 89, no. B12, p. 10,125–10,133.

Dahlen, F.A., 1990. Critical taper model of fold-and-thrust belts and accretionary wedges. Annual Review of Earth and Planetary Sciences, v. 18, no. 1, p. 55–99.

Dahlen, F.A., Suppe, J., Davis, D., 1984. Mechanics of fold-and-thrust belts and accretionary wedges: Cohesive Coulomb theory. Journal of Geophysical Research, v. 89, no. B12, p. 10,087–10,101.

Dahlstrom, C.D.A., 1969. Balanced cross-section. Can. J. Sci. 6, 743–757.

Davis, D., Suppe, J., Dahlen, F.A., 1983. Mechanics of fold and thrust belts and accretionary wedges. Journal of Geophysical Research, v. 88, no. B2, p. 1153–1172, doi:10.1029/JB088iB02p01153.

Davis, T.L., Namson, J. S., 1994. A balanced cross-section of the 1994 Northridge earthquake, southern California. Nature 372, 167-169.

De Sitter, L.U., 1956. Structural Geology. McGraw-Hill, New York, 551 pp.

Del Castello, M., Cooke, M.L., 2007. Underthrusting-accretion cycle: work budget as revealed by the boundary element method. J. Geophys. Res. 112.

Eisenstadt, G., Sims, D., 2005. Evaluating sand and clay models; do rheological differences matter? Journal of Structural Geology 27, 1399–1412.

Epard, J.L., Groshong, R.H., 1995. Kinematic model of detachment folding including limb rotation, fixed hinges and layer-parallel strain. Tectonophysics 247, 85–103.

Erickson, S., Jamison, W., 1995. Viscous-plastic finite-element models of fault-bend folds. Journal of Structural Geology 17, 561–573.

Erickson, S., Strayer, L., Suppe, J., 2001. Initiation and reactivation of faults during movement over a thrust-fault ramp: numerical mechanical models. Journal of Structural Geology 23, 11–23.

Erslev, E.A., 1991. Trishear fault-propagation folding. Geology 19, 617–620.

Erslev, E.A. Mayborn, K.R., 1997. Multiple geometries and modes of fault-propagation folding in the Canadian thrust belt. J. Struct. Geol. 19, 321–335.

Fantoni, R., Franciosi, R., 2010. Tectono-sedimentary setting of the Po plain and Adriatic foreland. Rend. Lincei 21 (1), S197-S209. doi:10.1007/s12210-010-0102-4.

Faulkner, D.R., Mitchell, T.M., Healy, D., Heap, M.J., 2006. Slip on 'weak' faults by the rotation of regional stress in the fracture damage zone. Nature 444, 922–925.

Finch, E., Hardy, S., Gawthorpe, R., 2003. Discrete element modelling of contractional fault-propagation folding above rigid basement fault blocks. Journal of Structural Geology 25, 515–528.

Finch, E., Hardy, S., Gawthorpe, R., 2004. Discrete-element modelling of extensional fault-propagation folding above rigid basement blocks. Basin Research 16, 489–506.

Fisher, M.P., Woodward, N.B., Mitchell, M.M., 1992. The kinematics of break-thrust folds. Journal of Structural Geology 14, 451–460.

Graveleau, F., Malavieille, J., Dominguez, S., 2012. Experimental modelling of orogenic wedges: a review. Tectonophysics, 538–540, 1–66.

Grothe, P.R., Cardozo, N., Mueller, K., Ishiyama, T., 2014. Propagation history of the Osaka-wan blind thrust, Japan, from trishear modeling. Journal of Structural Geology 58, 79–94.

Gutscher, M.A., Kukowski, N., Malavieille, J., Lallemand, S., 1998. Episodic imbricate thrusting and underthrusting: analog experiments and mechanical analysis applied to the Alaskan Accretionary Wedge. J. Geophys. Res. 103, 10,161–10,176.

Hale, D., 2013. Methods to compute fault images, extract fault surfaces, and estimate fault throws from 3D seismic images. Geophisics 78, NO. 2, O33–O43.

Hardy, S., Finch, E., 2007. Mechanical stratigraphy and the transition from trishear to kink-band fault-propagation fold forms above blind basement thrust faults: a discrete-element study. Marine and Petroleum Geology 24, 75–90.

Hardy, S., Ford, M., 1997. Numerical modelling of trishear fault propagation folding. Tectonics 16, 841–854.

Hardy, S., Duncan, C., Masek, J., Brown, D., 1998. Minimum work, fault activity and the growth of critical wedges in fold and thrust belts. Basin Res. 10, 365–373.

Hauksson, E., Jones, L.M., Hutton, K., 1995. The 1994 Northridge earthquake sequence in California: Seismological and tectonic aspects. Journal of Geophysical Research 100, 12335–12355.

Hedlund, C.A., 1997. Fault-propagation, ductile strain, and displacement-distance relationships. Journal of Structural Geology 19, 243–248.

Henza, A.A., Withjack, M.O., Schlische, R.W., 2010. Normal-fault development during two phases of non-coaxial extension: An experimental study. Journal of Structural Geology 32 (11), 1656–1667.

Hesse, S., Back, S., Franke, D., 2010. The structural evolution of folds in a deepwater fold and thrust belt — a case study from the Sabah continental margin offshore NW Borneo, SE Asia. Marine and Petroleum Geology 27, 442–454.

Hubbert, M.K., 1937. Theory of scale models as applied to the study of geologic structures. Geol. Soc. Am. Bull. 48, 1459–1520.

Hubbert, M.K., 1951. Mechanical basis for certain familiar geologic structures. Geol. Soc. Am. Bull. 62, 355–372.

Huftile, G.J., Yeats, R.S., 1996. Deformation rates across the Placerita (Northridge Mw = 6.7 aftershock zone) and Hopper Canyon segments of the western Transverse Ranges deformation belt. Bulletin of the Seismological Society of America, v. 86, no. 1, part B, p. 3–18.

Hughes, A.N., Shaw, J.H., 2014. Fault displacement distance relationships as indicators of contraction fault-related folding style. AAPG Bulletin 98, 227–251.

Hughes, A.N., Shaw, J.H., 2015. Insights into the mechanics of fault-propagation folding styles. Geol. Soc. Am. Bull. 127, 1752–1765.

Hutchinson, J.W., 1996. Stresses and Failure Modes in Thin Films and Multilayers, Notes for a DCAMM Course. Technical University of Denmark, Lyngby, 1–45.

Iacopini, D., Butler, R.W.H., Purves, S., McArdle, N., De Freslon, N., 2016. Exploring the seismic expression of fault zones in 3D seismic volumes. Journal of Structural Geology 89, 54–73. doi:10.1016/j.jsg.2016.05.005

Jamison, W., 1987. Geometric analysis of fold development in overthrust terranes. Journal of Structural Geology 9, 207–219.

Jin, G., Groshong, R.H., 2006. Trishear kinematic modeling of extensional fault-propagation folding. Journal of Structural Geology 28, 170–183.

Jones, C.H., Wesnousky, S.G., 1992. Variations in strength and slip rate along the San Andreas Fault system. Science 256, 83e86.

Kostenko, O.V., Naruk, S.J., Hack, W., Poupon, M., Meyer, H.-J., Mora-Glukstad, M., Anowai, C., Mordi, M., 2008. Structural evaluation of column-height controls at a toe-thrust discovery, deep-water Niger Delta. AAPG Bull. 92, 1615–1638.

Li, T., Chen, J., Fang, L., Chen, Z., Thompson, J.A., Jia, C., 2016. The 2015 Mw 6.4 Pishan earthquake: seismic hazards of an active blind Wedge thrust system at the western Kunlun range front, northwest Tibetan Plateau. Seismol. Res. Lett. 87(3): 1-8.

Lingrey, S., 2000. Structural interpretation and modeling of seismic data from the Moran and Paua Area, PNG Foldbelt. In: Buchanan, P., Grainge, A., Thornton, R. (Eds.), Papua New Guinea's Petroleum Industry in the 21st Century: Proceedings of the Fourth PNG Petroleum Convention. PNG Chamber of Mines and Petroleum, Port Moresby, pp. 385–396.

Liu, C., Yin, H., Zhu, L., 2012. TrishearCreator: a tool for the kinematic simulation and strain analysis of trishear fault-propagation folding with growth strata. Comput. Geosci. 49, 200–206.

Lu, R., Xu, X., He, D., Liu, B., Tan, X., Wang, X., 2016. Coseismic and blind fault of the 2015 Pishan M_w 6.5 earthquake: Implications for the sedimentary-tectonic framework of the western Kunlun Mountains, northern Tibetan Plateau. Tectonics 35, 956–964, doi:10.1002/2015TC004053.

Maesano, F.E., Toscani, G., Burrato, P., Mirabella, F., D'Ambrogi, C., Basili, R., 2013. Deriving thrust fault slip rates from geological modeling: Examples from the Marche coastal and offshore contraction belt, Northern Apennines, Italy. Marine and Petroleum Geology 42, 122-134, doi:10.1016/j.marpetgeo.2012.10.008.

Maesano, F.E., D'Ambrogi, C., Burrato, P., Toscani, G., 2015. Slip-rates of blind thrusts in slow deforming areas: examples from the Po Plain (Italy). Tectonophysics 643, 8-25. doi:10.1016/j.tecto.2014.12.007.

Maillot, B., Leroy, Y.M., 2006. Kink-fold onset and development based on the maximum strength theorem. J. Mech. Phys. Solids 54, 2030–2059.

Mansfield, C., Cartwright, J.A., 2001. Fault growth by linkage: observations and implications from analogue models. Journal of Structural Geology 23, 745–763.

McBeck, J., Madden, E.H., Cooke, M.L., 2016. Growth by Optimization of Work (GROW): A new modeling tool that predicts fault growth through work minimization. Comput. Geosci. 88, 142–151.

McClay, K., 2011. Introduction to thrust fault-related folding, In: McClay, K., Shaw, J. H., Suppe, J. (Eds.), Thrust fault-related folding, AAPG Mem., 94, 1–19.

Miller, J.F., Mitra, S., 2011. Deformation and secondary faulting associated with basement-involved compressional and extensional structures. AAPG Bull 95 (4), 675–689.

Mitra, S., 1990. Fault-propagation folds: geometry, kinematic evolution, and hydrocarbon traps. AAPG Bull 74, 921–945.

Mitra, S., 1992. Balanced structural interpretations in fold and thrust belts, In: Structural Geology of Fold and Thrust Belts (S. Mitra and G. W. Fisher, eds), pp. 53–77. John Hopkins University Press, Baltimore.

Mitra, S., 2002b. Structural models of faulted detachment folds. AAPG Bull 86, 1673–1694.

Mitra, S., 2003. A unified kinematic model for the evolution of detachment folds. Journal of Structural Geology 25, 1659–1673.

Mitra, S., Mount, V.S., 1998. Foreland basement-involved structures. Bulletin of the American Association of Petroleum Geologists 82, 70–109.

Mitra, S., Miller, J.F., 2013. Strain variation with progressive deformation in basement-involved trishear structures. Journal of Structural Geology 53, 70–79.

Mori, J., Wald, D.J., Wesson, R.L., 1995. Overlapping fault planes of the 1971 San Fernando and 1994 Northridge, California earthquakes. Geophys. Res. Lett 22, 1033-1036.

Moss, R.E.S., Ross, Z., 2011. Probabilistic fault displacement hazard analysis for reverse faults. Bull. Seismol. Soc. Am. 101, no. 4, 1542–1553.

Olson, E., Cooke, M.L., 2005. Application of three fault growth criteria to the Puente Hills thrust system, Los Angeles, California, USA. J. Struct. Geol. 27, 1765–1777.

Pei, Y., Paton, D.A., Knipe, R.J., 2014. Defining a 3-dimensional trishear parameter space to understand the temporal evolution of fault propagation folds. J. Struct. Geol. 66, 284e297. http://dx.doi.org/10.1016/j.jsg.2014.05.018.

Poblet, J., McClay, K., 1996. Geometry and kinematics of single layer detachment folds. Am. Assoc. Petrol. Geol. Bull 80, 1085–1109.

Ramberg, H., 1981. Gravity, deformation and the Earth's crust. Academic Press, London.

Roering, J.J., Cooke, M.L., Pollard, D.D., 1997. Why blind thrust faults do not propagate to the earth's surface: Numerical modeling of coseismic deformation associated with thrust-related anticlines. J. Geophys. Res. 102, 11,901-11,912.

Savage, H.M., Cooke, M.L., 2010. Unlocking the effects of friction on fault damage zones. J. Struct. Geol. 32 (11), 1732–1741.

Scholz, C.H., 2002. The Mechanics of Earthquakes and Faulting, second ed. Cambridge University Press, New York, p. 471.

Segall, P., Pollard, D.D., 1983. Joint formation in granitic rock of the Sierra Nevada. Geol. Soc. Am. Bull. 94, pp. 563–571.

Shaw, J., Shearer, P., 1999. An elusive blind-thrust beneath metropolitan Los Angeles. Science 283, 1516–1518.

Sibson, R.H., Xie, G., 1998. Dip range for intracontinental reverse fault ruptures: truth not stranger than friction? Bulletin of the Seismological Society of America 88, 1014-1022.

Souloumiac, P., Leroy, Y.M., Maillot, B., Krabbenhøft, K., 2009. Predicting stress distributions in fold-and-thrust belts and accretionary wedges by optimization. J. Geophys. Res. 114.

Souloumiac, P., Krabbenhøft, K., Leroy, Y.M., Maillot, B., 2010. Failure in accretionary wedges with the maximum strength theorem: numerical algorithm and 2D validation. Comput. Geosci 14, 793–811.

Storti, F., Salvini, F., 1996. Progressive rollover fault-propagation folding: a possible kinematic mechanism to generate regional-scale recumbent folds in shallow foreland belts. Am. Assoc. Petrol. Geol. Bull 80, 174–193.

Storti, F., Salvini, F., McClay, K., 1997. Fault-related folding in sandbox analogue models of thrust wedges. Journal of Structural Geology 19, 583–602.

Suppe, J., 1983. Geometry and kinematics of fault-bend folding. Am. J. Sci. 283, 684–721.

Suppe, J., Medwedeff, D.A., 1984. Fault-propagation folding. Geol. Soc. Am. Bull. (Abstracts with Programs), 16, 670.

Suppe, J., Medwedeff, D.A., 1990. Geometry and kinematics of fault-propagation folding. Eclogae Geol. Helv. 83, 409–454.

Suppe, J., Connors, C.D., Zhang, Y., 2004. Shear fault-bend folding. In: Thrust Tectonics and Hydrocarbon Systems (K.R. McClay, ed.). Am. Assoc. Petrol. Geol. Mem. 82, 303–323.

Tavani, S., Storti, F., 2006. Fault-bend folding as an end-member solution of (double-edge) fault-propagation folding. Terra Nova 18, 270–275.

Tavani, S., Storti, F., Salvini, F., 2006. Double-edge fault-propagation folding: geometry and kinematics. Journal of Structural Geology 28, 19–35.

Tavani, S., Granado, P., Arbués, P., Corradetti, A., Muñoz, J.A., 2017. Syn-thrusting, near-surface flexural-slipping and stress deflection along folded sedimentary layers of the Sant Corneli-Bóixols anticline (Pyrenees, Spain). Solid Earth, 8, 405–419. doi:10.5194/se-8-405-2017.

Thielicke, W., 2014. The Flapping Flight of Birds – Analysis and Application, Phd thesis, Rijksuniversiteit, Groningen.

Thielicke, W., Stamhuis, E.J., 2014. PIVlab – Towards User-friendly, Affordable and Accurate Digital Particle Image Velocimetry in MATLAB. Journal of Open Research Software, 2(1):e30, doi: http://dx.doi.org/10.5334/jors.bl.

Toscani, G., Bonini, L., Ahmad, M. I., Di Bucci, D., Di Giulio, A., Seno, S., Galuppo, C., 2014. Opposite verging chains sharing the same foreland: kinematics and interaction through analogue models (Central Po Plain, Italy). Tectonophysics 633, 268-282. doi:10.1016/j.tecto.2014.07.019.

Turrini, C., Lacombe, O., Roure, F., 2014. Present-day 3D structural model of the Po Valley basin, Northern Italy. Mar. Pet. Geol. 56, 266–289. http://dx.doi.org/10.1016/j. marpetgeo.2014.02.006.

Turrini, C., Toscani, G., Lacombe, O., Roure, F., 2016. Influence of structural inheritance on foreland-foredeep system evolution: An example from the Po valley region (northern Italy). Mar. Pet. Geol. 77, 376–398. http://dx.doi.org/10.1016/j.marpetgeo.2016.06.022.

Vannoli, P., Basili, R., Valensise, G., 2004. New geomorphologic evidence for anticlinal growth driven by blind-thrust faulting along the northern Marche coastal belt (central Italy). Journal of Seismology 8, 297-312, doi:10.1023/B:JOSE.0000038456.00574.e3.

Wang, C.Y., Chen, H.L., Cheng, X.G., Li, K., 2013. Evaluating the role of syn-thrusting sedimentation and interaction with frictional detachment in the structural evolution of the SW Tarim basin, NW China: insights from analogue modeling. Tectonophysics 608, pp. 642–652.

Wang, P., Xu, L.R., 2006. Dynamic interfacial debonding initiation induced by incident crack. Int. J. Solids Struct. 43, 6535–6550.

Welch, M.J., Knipe, R.J., Souque, C., Davies, R.K., 2009b. A Quadshear kinematic model for folding and clay smear development in in fault zones. Tectonophysics 471, 186–202.

Williams, G., Chapman, T., 1983. Strains developed in the hanging walls of thrusts due to their slip/propagation rate: a dislocation model. Journal of Structural Geology 5, 563–571.

Withjack, M.O., Oloson, J., Peterson, E., 1990. Experimental models of extensional forced folds. AAPG Bull. 74, 1038e1054.

Xu, L.R., Huang, Y.Y., Rosakis, A.J., 2003. Dynamic crack detection and penetration at interfaces in homogeneous materials: experimental studies and model predictions. J. Mech. Phys. Solids 51, 461–486.Zehnder, A.T., Allmendinger, R.W., 2000. Velocity field for the trishear model. Journal of Structural Geology 22, 1009–1014.

Yagupsky, D.L., Brooks, B.A., Whipple, K.X., Duncan, C.C., Bevis, M., 2014. Distribution of active faulting along orogenic wedges: minimum-work models and natural analogue. J. Struct. Geol. 66, 237–2 47.

Yan, P., Liu, H., 2004. Tectonic-stratigraphic division and blind fold structures in Nansha waters, South Shina sea. Journal of Asian Earth Sciences 24, 337–348.

Zhao, H., Guo, Z., Yu, X., 2017. Strain modelling of extensional fault-propagation folds based on an improved non-linear trishear model: A numerical simulation analysis. Journal of Structural Geology 95, 60–76.

Appendix A. Fault and fractures analysis in the second and third series of clay analogue models

Here are illustrated the fault and fractures analysis of the second and third set of analogue experiments. These second and third set are used together with the first series illustrated in Chapter 2 (Figs. 2.3 and 2.6) for the analysis of fault propagation, angle of incidence and folding evolution.

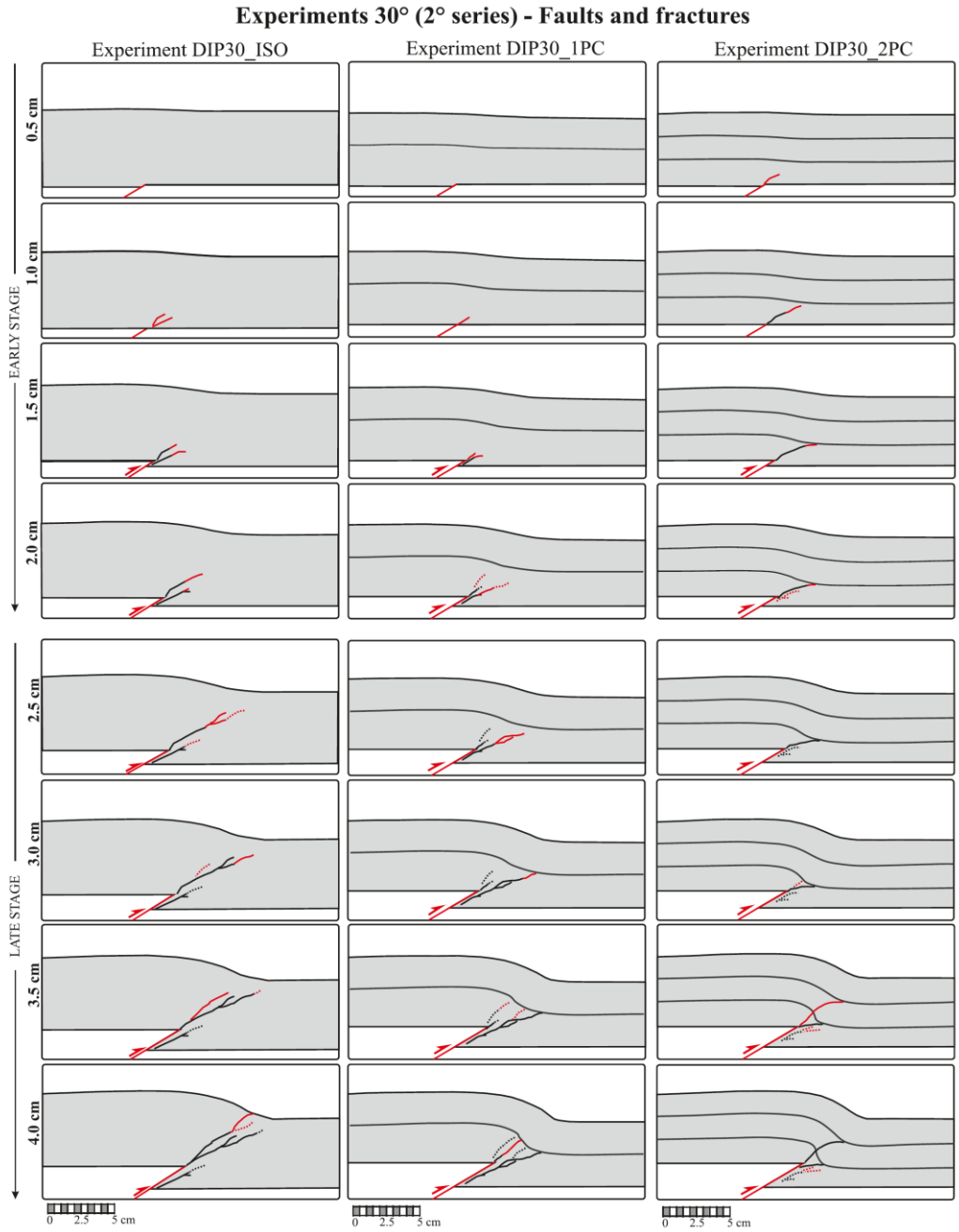

Figure A.1. 2° series of experiments. Analysis of faults and fractures in experiments with master fault dipping 30° for three different configurations: isotropic (_ISO), one precut (_1PC), and two precuts (_2PC). Each row represents the development of faults and fractures at every increment of 5 mm displacement on the master fault. Red and black lines represent the newly- and previously-formed faults, respectively, at each successive increment of displacement (5 mm). Dotted lines indicate faults or fractures where the offset determination is uncertain. Black thin lines indicates the position of precuts.

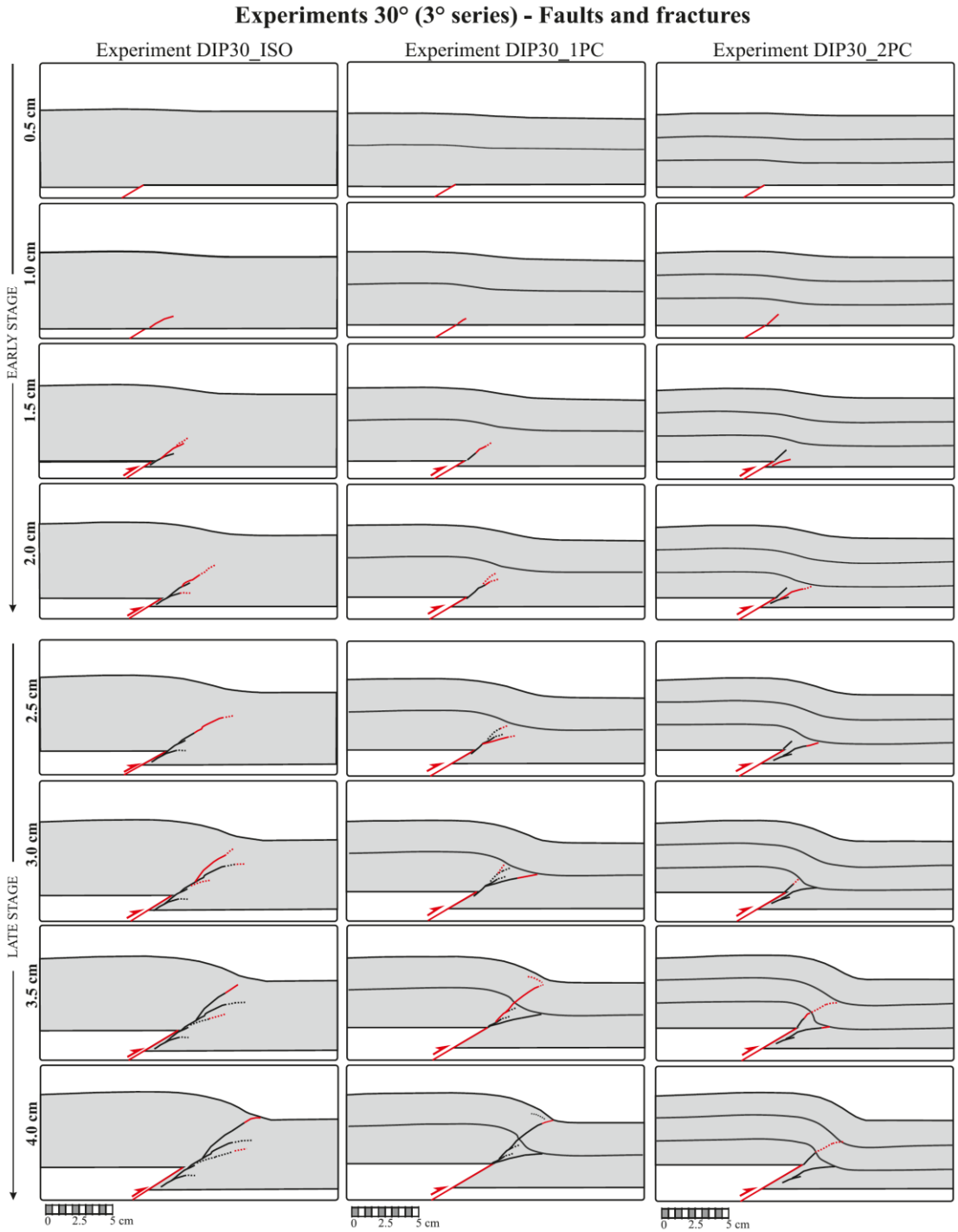

Figure A.2. 3° series of experiments. Analysis of faults and fractures in experiments with master fault dipping 30° for three different configurations: isotropic (_ISO), one precut (_1PC), and two precuts (_2PC). Each row represents the development of faults and fractures at every increment of 5 mm displacement on the master fault. Red and black lines represent the newly- and previously-formed faults, respectively, at each successive increment of displacement (5 mm). Dotted lines indicate faults or fractures where the offset determination is uncertain. Black thin lines indicates the position of precuts.

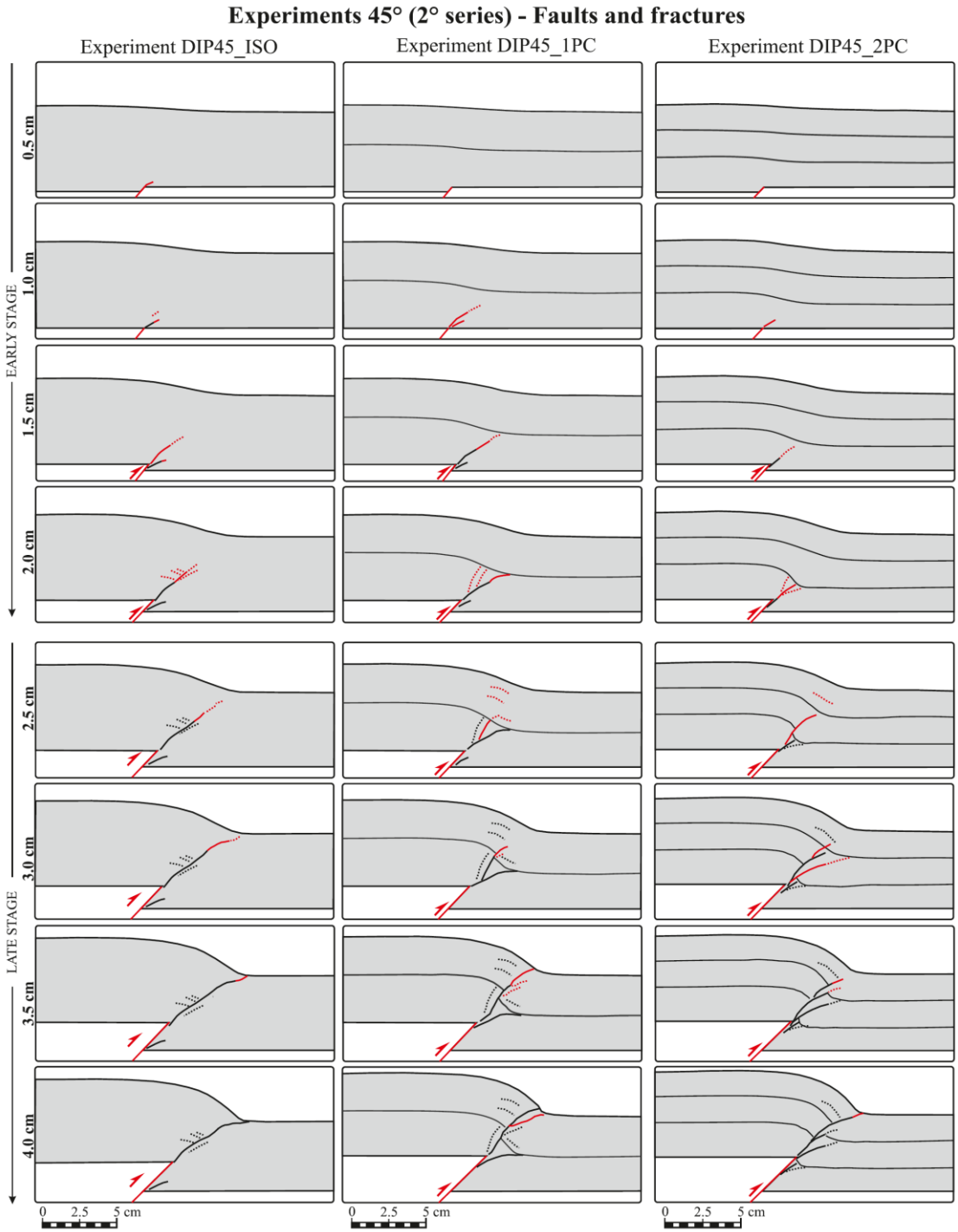

Figure A.3. 2° series of experiments. Analysis of faults and fractures in experiments with master fault dipping 45° for three different configurations: isotropic (_ISO), one precut (_1PC), and two precuts (_2PC). Each row represents the development of faults and fractures at every increment of 5 mm displacement on the master fault. Red and black lines represent the newly- and previously-formed faults, respectively, at each successive increment of displacement (5 mm). Dotted lines indicate faults or fractures where the offset determination is uncertain. Black thin lines indicates the position of precuts.

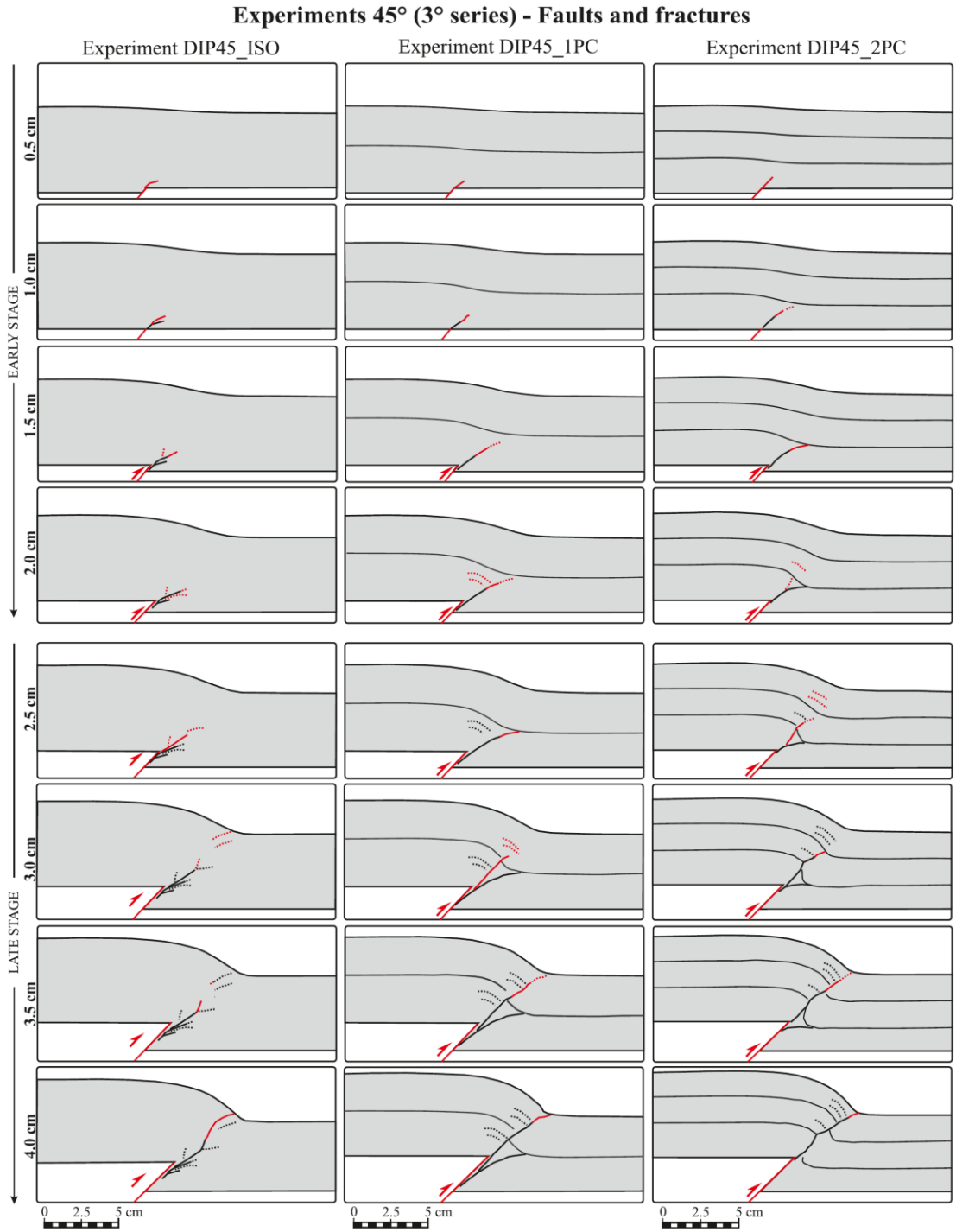

Figure A.4. 3° series of experiments. Analysis of faults and fractures in experiments with master fault dipping 45° for three different configurations: isotropic (_ISO), one precut (_1PC), and two precuts (_2PC). Each row represents the development of faults and fractures at every increment of 5 mm displacement on the master fault. Red and black lines represent the newly- and previously-formed faults, respectively, at each successive increment of displacement (5 mm). Dotted lines indicate faults or fractures where the offset determination is uncertain. Black thin lines indicates the position of precuts.

Appendix B. GROW models

The numerical analysis described in Chapter 3 involved also the use of the recently developed tool GROW (Growth by Optimization of Work; McBeck et al., 2016). GROW uses Fric2D to determine slip on pre-existing surfaces and to evaluate failure in all potential propagation directions. GROW calculates the external work for all the propagation direction of one or many growing faults and, following the principal of work optimization, add a fault element in the direction that minimize the external Work (McBeck, et al., 2016, Madden et al., 2017).

In GROW models we set a fault element as a starter element which is free to propagate (Fig A.5). From the starter element, GROW calculates the propagation path of the fault using the work optimization approach. The fault propagation will continue until the fault intersects another fault or boundary or if the last element added in the last propagation step does not fail in shear or in tension.

The GROW models are executed on the 45° dipping master fault setup and are built to analyze two stages i.e. Early and Late stages (Fig. A.5). The *Early Stage* models investigate if the propagation path (PP) reproduces the curved fault observed in analogue models, and how the PP changes by varying the friction on the layer parallel interface (coefficient of friction simulated: 0.0, 0.1, 0.2). A starter element is added at the tip of the master fault (Fig A.5a). The *Late Stage* models investigate the development of second fault observed in analogue models, which is also the fault that crosses the layer parallel interface. In the Late stage, the layer parallel interface has a higher degree of curvature (equal to that used for the Late stage of numerical analysis in Chapter 3) compared to the Early stage, and a starter element branches off from the tip of the previous one, and for each friction value along the layer parallel interface (0.0, 0.1, 0.2), the corresponding PP of the Early stage is prescribed (Fig A.5b).

In the Early Stage, all the formed faults change their direction decreasing their dip compared to the starter element, to produce a curved fault that grows toward the interface. Increasing the friction on the layer-parallel interface (from 0.0 to 0.2) increases the dip of the formed faults (Fig A.5a). With 0.0 friction on the layer parallel interface, the formed fault terminates its propagation without to reach the layer parallel interface. With friction 0.1 and 0.2 on the layer parallel interface the faults terminate against the layer-parallel interface forming a short, convex downward segment.

Also in the Late stage, the formed faults increase their dip increasing the friction on the layer parallel interface (Fig A.5b). In all the three cases they terminate against the layer parallel interface forming a convex upward geometry.

These results indicate that the newly formed faults increase their dip with higher friction along the layer-parallel interface; however, the tendency of the fault to form splays is always preserved. These findings strengthen those coming from the slip partitioning and external work analysis illustrated in Chapter 3, indicating that lower values of friction facilitate the development of the curved faults and thus will have a greater impact on the propagation rate of the master fault. Neverless, GROW still has a not negligible intrinsic limitation, i.e. it does not reproduce the folding of the layer-parallel interface during the slipping and propagation of the faults, hence I retained to insert GROW models as appendix of this thesis.

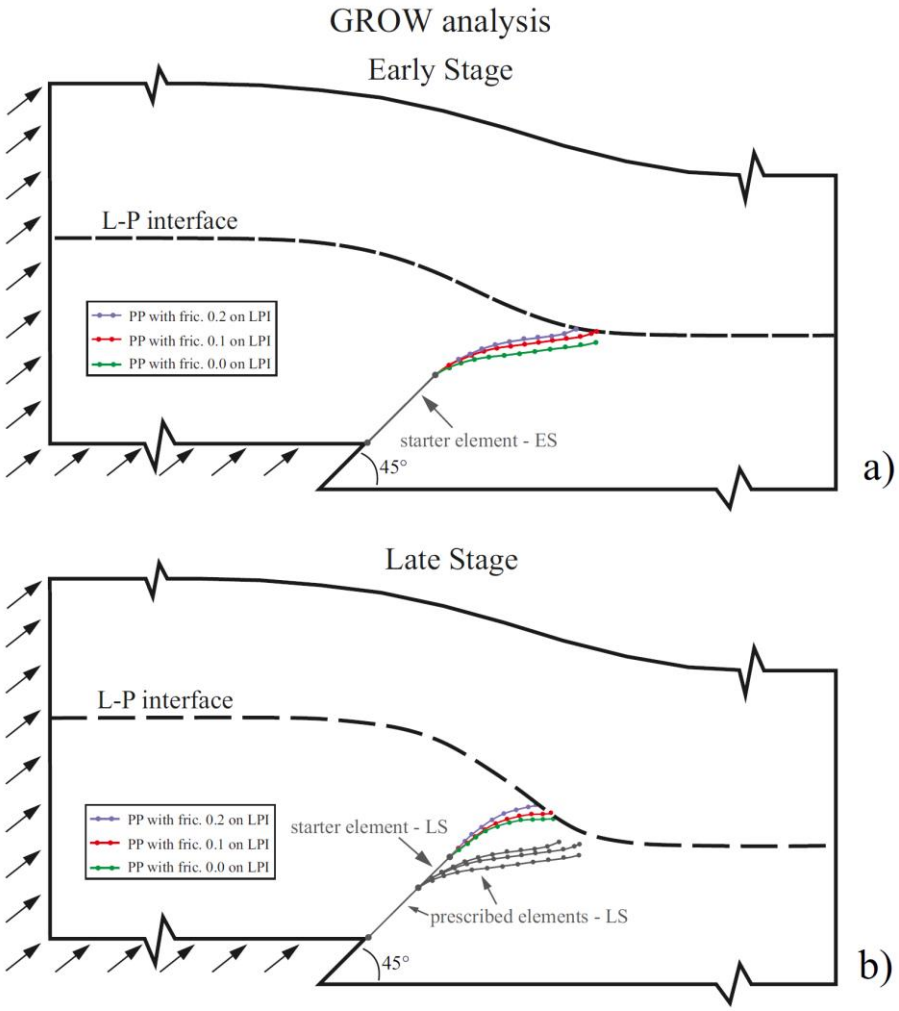

Figure A.5. Propagation paths (PP) of faults applying different friction along the layer-parallel interface (LPI). a) Early stage: a starter element with the same dip of the master fault is prescribed. b) Late Stage: for each friction value along FI, the corresponding PP of the early stage is prescribed. A starter element branches off from the tip of the previous starter element of the Early Stage.